

---

Electronic Thesis and Dissertation Repository

---

4-17-2024 10:15 AM

# Breast Cancer Risk in Women with Breast Bilateral Asymmetry: Machine Learning Based Risk Analysis and Mitigation through Developing a Framework for Customized Bra Design

Xi Feng, *Electrical and Computer Engineering*

Supervisor: Abbas Samani, *The University of Western Ontario*

A thesis submitted in partial fulfillment of the requirements for the Doctor of Philosophy degree  
in Electrical and Computer Engineering

© Xi Feng 2024

Follow this and additional works at: <https://ir.lib.uwo.ca/etd>



Part of the [Biomedical Commons](#)

---

## Recommended Citation

Feng, Xi, "Breast Cancer Risk in Women with Breast Bilateral Asymmetry: Machine Learning Based Risk Analysis and Mitigation through Developing a Framework for Customized Bra Design" (2024). *Electronic Thesis and Dissertation Repository*. 10034.

<https://ir.lib.uwo.ca/etd/10034>

This Dissertation/Thesis is brought to you for free and open access by Scholarship@Western. It has been accepted for inclusion in Electronic Thesis and Dissertation Repository by an authorized administrator of Scholarship@Western. For more information, please contact [wlsadmin@uwo.ca](mailto:wlsadmin@uwo.ca).

## Abstract

Breast cancer is the most prevalent form of cancer globally, accounting for 12.5% of all new cases annually. Research has found a significant correlation between breast bilateral asymmetry and an increased risk of cancer, with women diagnosed with breast cancer having higher levels of bilateral asymmetrical breast volume. Unfortunately, 87% of women with breast asymmetry lack adequate tools for assessing their cancer risk. Early screening using bilateral asymmetry to predict a woman's long-term risk of breast cancer can help physicians make informed decisions about whether to recommend sequential imaging and the frequency of screening. Another important factor in understanding the cause of breast cancer is the association between long-term abnormal mechanical stress distribution in breast tissue and the increased risk of developing breast lesions. Chronic stress promotes cancer development through various molecular mechanisms. However, existing off-the-shelf symmetric bras do not adequately address breast asymmetry, as they may not provide sufficient support for smaller breasts while inducing high stress levels to larger breasts. Therefore, it is essential to explore the relationship between concentrated stress from ill-fitted bras and its potential contribution to breast cancer development. A more personalized and tailored bra fitting technique could significantly reduce the risk of breast cancer associated with mechanical stress. In this study, we developed an unsupervised machine learning algorithm to classify breast bilateral asymmetry using bilateral magnetic resonance imaging. A clear link between breast asymmetry and breast cancer risk has been established, providing a predictive tool for proactive breast health assessment. We then developed two complementary computational inversion techniques to determine the individual-specific hyperelastic parameters of breast tissue, along with the breast's undeformed shape, using MRI images. This synergistic algorithm addresses issues with preloading-induced errors, thereby providing a more precise foundation for designing customized bras. The development of customized bras for cancer-prone women with significant breast asymmetry is facilitated by the optimization of breast tissue stress distribution. This is achieved through the accurate capture of breast shape and tissue properties. By integrating these details with various textile options for bra modeling, our study supports the natural state of the breast and reduces potentially harmful stress concentrations. Our research contributes significantly to the understanding of breast cancer

risk factors and offers potential for innovative approaches in preventive breast healthcare. This study is a crucial step forward in the field and demonstrates the potential for improved outcomes in breast health.

## Keywords

Asymmetry, Bilateral, Biomechanics, Bra Design, Breast Cancer, Computer Assisted Medical Procedures, Finite Element Analysis, Hyperelastic Parameter, Inversion Solution, MRI, Reference Geometry, Machine Learning, Neural Networks, Optimization, Reconstruction, Stress-free Geometry

## Summary for Lay Audience

Breast cancer affects millions of women worldwide, making it a major health threat. Scientists are uncovering surprising factors that impact risk of breast cancer development, including those that many women are unaware of. In recent years, scientists have investigated various factors that may contribute to this disease. One significant factor is breast tissue density, a condition in which there is more fibrous tissue than fatty tissue in the breasts. This increased density is associated with a higher risk of breast cancer, especially in premenopausal women, making them up to six times more likely to develop the disease.

Another interesting aspect of this research focuses on the concept of breast bilateral asymmetry, where one breast has a different size, shape or tissue distribution than the other. Surprisingly, this condition is quite common, affecting approximately 87% of the women. However, most bras available in stores are designed for symmetrical breasts, which means that they do not fit well for women with this asymmetry. This poor fit can lead to uneven pressure and stress on the breast. Studies have suggested that this uneven stress might contribute to an increased risk of developing breast cancer.

To explore this further, this research delves into the relationship between breast asymmetry and breast cancer risk. It looks at detailed breast MRI scans from a long-term study to understand whether and how different breast sizes, shape and composition can affect the likelihood of developing cancer, leading to a classification tool for determining the risk of breast cancer using the woman's breast MRI. This research also proposes an innovative approach – designing custom-made bras that cater to the unique needs of women with breast asymmetry. The goal is to provide better support and reduce the uneven stress caused by standard bras. By doing so, it is hoped that this could be a step towards reducing the breast cancer risk in these women.

In essence, this study aimed at understanding the nuances of breast health and how factors such as tissue density and breast asymmetry can influence cancer risk. It also seeks to provide practical solutions, such as custom-made bras, which could not only improve comfort, but also potentially play a role in preventing breast cancer. By combining medical

research with everyday products, this study aimed at making a meaningful impact on women's health and well-being.

## Co-Authorship Statement

The major contributors are Xi Feng and Dr. Abbas Samani where Xi Feng was the first author who wrote the initial draft of the manuscript and developed all the code. Dr. Samani was responsible for conceiving ideas and consultation for algorithms development, supervision, and editing the manuscripts.

## Acknowledgments

To my esteemed supervisor Dr. Abbas Samani. I'm reminded of the ancient adage, "A mentor for a day is a godfather for a lifetime." Beyond imparting academic wisdom, he has been a paragon of diligence and precision in scientific inquiry, embodying virtues that extend far beyond the realm of academia into the very essence of being.

To my parents, I extend my deepest gratitude for the freedom and support they have bestowed upon me, allowing me to pursue the life I envision for myself. Their love has been my guiding light, empowering me to carve my own path with conviction and courage.

To my lab mates: Halimah Alsurayhi, Matthew Adrian Caius and Tristan Curry, for their unwavering support and camaraderie throughout my PhD journey. Their encouragement has been invaluable, and I truly appreciate their contribution to my academic and personal growth.

And to myself, I offer a note of appreciation for never yielding in the face of adversity. With each setback, my resolve has only strengthened, akin to the mythical phoenix rising anew from its ashes—reborn, resilient, and radiant.

# Table of Contents

Abstract.....	ii
Summary for Lay Audience.....	iv
Co-Authorship Statement.....	vi
Acknowledgments.....	vii
Table of Contents.....	viii
List of Tables.....	xii
List of Figures.....	xii
List of Abbreviations.....	xvi
Chapter 1.....	1
1 « Introduction».....	1
1.1 « Background and Motivation ».....	1
1.1.1 Statistics.....	1
1.1.2 Breast Anatomy and Physiology.....	4
1.1.3 Breast Cancer and Asymmetry.....	7
1.1.4 Biomechanical Modeling for Breast.....	9
1.1.5 Breast Gravitational Deformation.....	13
1.1.6 Bra Design.....	14
1.2 « Theory ».....	15
1.2.1 Magnetic Resonance Imaging.....	15
1.2.2 Tissue Biomechanics.....	17
1.3 « Literature Review ».....	19
1.3.1 Breast Cancer Assessment based on Bilateral Asymmetry.....	19
1.3.2 Biomechanical Properties of Breast Tissue.....	21
1.3.3 Stress Concentration and Cancer Risk.....	24

1.3.4 Bra Shape Optimization .....	25
1.4 « Objectives » .....	26
1.5 « Thesis Outline » .....	27
1.5.1 Thesis Overview .....	27
1.5.2 Chapter 2 .....	28
1.5.3 Chapter 3 .....	29
1.5.4 Chapter 4 .....	29
1.5.5 Chapter 5 .....	30
1.5.6 Chapter 6 .....	30
References .....	30
Chapter 2 .....	43
2 « Prediction Risk of Breast Cancer Development Using Breast Bilateral Asymmetry Analysis within a Machine Learning Framework » .....	43
2.1 « Introduction » .....	43
2.2 « Materials and Methods » .....	45
2.2.1 Overview of Proposed Model .....	45
2.2.2 Data acquisition .....	46
2.2.3 Data Augmentation Using Finite Element (FE) Based Image Warping .....	48
2.2.4 Feature Engineering .....	51
2.2.5 Clustering .....	56
2.2.6 Validation .....	60
2.3 « Results » .....	61
2.3.1 Data Augmentation Validation .....	61
2.3.2 Feature Engineering .....	62
2.3.3 Clustering .....	63
2.4 « Discussion and Conclusions » .....	69

References .....	72
Chapter 3 .....	78
3 « Machine-Learning Based Inverse Problem Technique to Determine Hyperelastic Parameters of Breast Tissue Under Zero-gravity Conditions » .....	78
3.1 « Introduction » .....	78
3.2 « Theory » .....	81
3.3 « Methods » .....	84
3.3.1 Dataset Construction .....	86
3.3.2 Uniaxial Testing .....	91
3.3.3 Neural Network for Mapping Loaded to Unloaded Parameters .....	93
3.3.4 Data Fitting .....	96
3.4 « Results » .....	97
3.4.1 Sensitivity Analysis .....	97
3.4.2 Parameters Fitting .....	98
3.4.3 Evaluation of Neural Network Performance .....	99
3.4.4 Ablation study results on Neural Network configuration .....	101
3.4.5 Examples of Stress-Free Hyperelastic Parameters .....	102
3.5 « Discussion and Conclusion » .....	104
References .....	106
Chapter 4 .....	110
4 « A Machine Learning Based Algorithm to Determine Unloaded Geometry of the Breast Using MRI Image Data » .....	110
4.1 « Introduction » .....	110
4.2 « Material and Methods » .....	113
4.2.1 Stress-Free Geometry Space .....	115
4.2.2 Loaded Geometry Space .....	117
4.2.3 Neural Network Design .....	118

4.2.4 Validation .....	120
4.3 « Results » .....	121
4.4 « Discussion and Conclusion » .....	127
References .....	130
Chapter 5 .....	134
5 « Biomechanics-driven Optimization of Bra Shape Design for Women with Bilateral Asymmetry: Leveraging Individual MRI Data and Hyperelastic Parameters for Breast-Bra Contact Mechanics– Preliminary Study » .....	134
5.1 «Introduction » .....	134
5.2 « Material and Methods » .....	137
5.2.1 Geometry Alignment .....	138
5.2.2 Finite Element Analysis .....	142
5.3 « Preliminary Results » .....	145
5.3.1 Geometry Alignment and Displacement Mapping .....	145
5.3.2 Resultant Forces from Repeated Experiments .....	146
5.3.3 Stress Analysis at Optimal Position .....	147
5.4 « Discussion and Conclusions » .....	148
Reference .....	149
Chapter 6 .....	153
6 « Conclusions and Future Work » .....	153
6.1 « Conclusions » .....	153
6.1.1 Chapter 2 .....	153
6.1.2 Chapter 3 .....	154
6.1.3 Chapter 4 .....	155
6.1.4 Chapter 5 .....	155
6.2 « Future Directions » .....	156
6.3 « Closing Remarks » .....	157

## List of Tables

Table 1-1: Overview of mechanical testing methods for breast tissue. ....	11
Table 2-1: Features related to breast tissue density and texture with their description. ....	52
Table 2-2: Comparative performance metrics of breast cancer detection models. ....	69
Table 3-1: Sensitivity matrix (S) for 0.99 reduction factor. ....	97
Table 3-2: Comparative Performance Metrics of Neural Network Predictions for Hyperelastic Models. ....	100
Table 3-3: Ablation study results for optimizing Neural Network configurations. ....	101
Table 3-4: Stress-Free Parameters for Different stiffness tissue. ....	103
Table 4-1: Evaluation metrics. ....	123
Table 4-2: Comparative ablation study results for Neural Network performance with 10 principal components. ....	125
Table 5-1: Optimal bra displacement and resultant forces analysis. ....	147

## List of Figures

Figure 1-1 : Comparative trends in diagnosis and mortality rates for breast cancer vs. other cancers (2019-2023).....	1
Figure 1-2 : Distribution and survival rates of breast cancer subtypes.....	3
Figure 1-3 : A fishbone diagram to visualize logical structure of this thesis “Introduction” Chapter.....	3
Figure 1-4 : Anatomy of the breast. (Copyright Illustration 27676555   Breast Anatomy © Ermolaevamariya   Dreamstime.com).....	4
Figure 1-5 : Comparative anatomy of firming and sagging breasts highlighting Cooper's Ligaments. (Copyright Illustration 153331644   Breast © Yomogi1   Dreamstime.com.).....	6
Figure 1-6 : Pathways from breast asymmetry to increased breast cancer risk.....	9
Figure 1-7 : Stress-strain curve (Figure taken from [6]).....	11
Figure 1-8 : Breast MRI scan of a cancerous lesion.....	16
Figure 2-1 : Block diagram of the clustering method proposed for breast cancer risk assessment.....	46
Figure 2-2 : Breast bilateral MRI images of two patients included in the study. (a) depicts the first scan of a patient's breast, where the arrow highlights a region of dense tissue initially not diagnosed as cancerous by the radiologist. (b) shows a subsequent scan of the same patient, where the previously dense tissue area has since developed into a cancerous tumor, as confirmed by biopsy. This is a good example of a patient’s breasts with substantial bilateral asymmetry that is clearly visible in the image. (c) presents the first scan of a breast that was correctly identified as non-cancerous. Due to the rich blood supply in the nipple-areolar complex, this tissue was misinterpreted as a cancerous mass. In (d), the second scan of the patient shows that the tissue at this location is non-cancerous, similar to the tissue on the	

right side. This type of misdiagnosis often occurs in large-sized breasts. Compared to the former patient, the breasts of the latter patient has less obvious bilateral asymmetry. ....	47
Figure 2-3 : Block diagram of the proposed warping framework. ....	49
Figure 2-4 : (a)(c) Original breast slice MRI images (b)(d) Slice images from the volumes generated by assigning different hyperelastic parameters and applying rotations at various angles. ....	62
Figure 2-5 : Comparative analysis of initially extracted and ultimately selected features in volume-by-volume clustering. ....	63
Figure 2-6 : ROC curve comparison. The orange curve represents our completed dataset of 210 cases examined on all positive and negative cases with AUC = 0.85 (reference AUC = 0.5). ....	64
Figure 2-7 : Comparison between two sets of features (used for model and additional validation). Their centroids and distributions are very close, and the feature distributions almost have the same tendency. ....	65
Figure 2-8 : Example of classification for five cases using the slice-by-slice clustering method, with the stacked bars representing the count of MRI slices in each risk category and a green line indicating the final risk category determined by majority vote. ....	66
Figure 2-9 : Detailed comparison of clustering results between volumetric and sliced clustering methods, where the two classification methods have a high degree of consistency, with 95% of the points falling within the same classification region. ....	67
Figure 3-1 : Neural Network model for computing breast tissue stress-free (unloaded) hyperelastic parameters from loaded parameter counterpart. ....	86
Figure 3-2 : Axial stress distribution of the cylindrical breast tissue sample with Yeoh hyperelastic parameters of $C_1$ , $C_2$ and $C_3$ obtained using Finite Element Analysis. ....	92
Figure 3-3 : Proposed NN architecture, illustrating the data flow and neuronal interconnections. ....	94

Figure 3-4 : Yeoh and Ogden model fittings to uniaxial stress-strain data. ....	99
Figure 4-1 : Block diagram outlining the proposed inversion algorithm for reconstructing the breast stress-free geometry. ....	114
Figure 4-2 : Cylindrical coordinate system applied to breast model geometry. ....	116
Figure 4-3 : Schematic of the proposed Neural Network architecture. ....	119
Figure 4-4 : Comparison of performance metrics across principal component numbers. ....	124
Figure 4-5 : Comparison of two breast surface point clouds of (a) the groundtruth model extracted from MRI (under gravity loading state) and (b) reconstructed breast surface model under gravity-loading derived from corresponding stress-free state geometry generated using the proposed algorithm. ....	126
Figure 5-1 : Flowchart of proposed breast-bra contact mechanics technique. ....	138
Figure 5-2 : A sketch of two forces $F_1$ and $F_2$ which bra applies. ....	144
Figure 5-3 : Displacement mapping of breast surface points assigned with the displacements of corresponding bra surface points. ....	145
Figure 5-4 : Stress Distribution Analysis on Breast Surface. ....	148

## List of Abbreviations

<b>AUC</b>	Area Under the Curve
<b>ANN</b>	Artificial Neural Network
<b>BI-RADS</b>	Breast Imaging Reporting and Data System
<b>CAD</b>	Computer-Aided Detection
<b>DCIS</b>	Ductal Carcinoma In Situ
<b>ECM</b>	Extracellular Matrix
<b>FN</b>	False Negatives
<b>FP</b>	False Positives
<b>FGTs</b>	Fibroglandular Tissues
<b>FEM</b>	Finite Element Method
<b>GLCM</b>	Gray-Level Co-Occurrence Matrix
<b>GLDM</b>	Gray-Level Dependence Matrix
<b>GLRLM</b>	Gray-Level Run-Length Matrix
<b>GLSZM</b>	Gray-Level Size Zone Matrix
<b>HD</b>	Hausdorff Distance
<b>IDC</b>	Invasive Ductal Carcinoma
<b>ILC</b>	Invasive Lobular Carcinoma
<b>ICP</b>	Iterative Closest Point
<b>LASSO</b>	Least Absolute Shrinkage and Selection Operator
<b>LV</b>	Left Ventricle

<b>LPP</b>	Locally Preserving Projection
<b>MRI</b>	Magnetic Resonance Imaging
<b>MSE</b>	Mean Squared Error
<b>mRMR</b>	Minimum Redundancy Maximum Relevance
<b>mpMRI</b>	Multiparametric MRI
<b>NGTDM</b>	Neighborhood Gray-Tone Difference Matrix
<b>NN</b>	Neural Network
<b>NMI</b>	Normalized Mutual Information
<b>OBSP</b>	Ontario Breast Screening Program
<b>PCA</b>	Principal Component Analysis
<b>RF</b>	Radiofrequency
<b>ROC</b>	Receiver Operating Characteristic
<b>ReLU</b>	Rectified Linear Unit
<b>STD</b>	Standard Deviation
<b>SSE</b>	Sum of Squared Errors
<b>TN</b>	True Negatives
<b>TP</b>	True Positives
<b>VR</b>	Virtual Reality

## Chapter 1

### 1 « Introduction »

#### 1.1 « Background and Motivation »

##### 1.1.1 Statistics

Cancer remains the leading cause of death in Canada. Breast cancer presents a particularly significant burden, representing the most commonly diagnosed cancer in Canadian women and the second leading cause of cancer-related death [1]. In 2023, it was estimated that 27,700 women were diagnosed with breast cancer, and 5,300 Canadian women died from the disease [2]. This ranks breast cancer as a major contributor to the overall impact of cancer on Canadians, alongside lung and other cancers. While mortality rates are declining, the annual number of new breast cancer cases remains substantial [2]. Figure 1-1 illustrates the comparative analysis of diagnosis numbers and mortality rates between breast cancer and other cancers over the last five years.

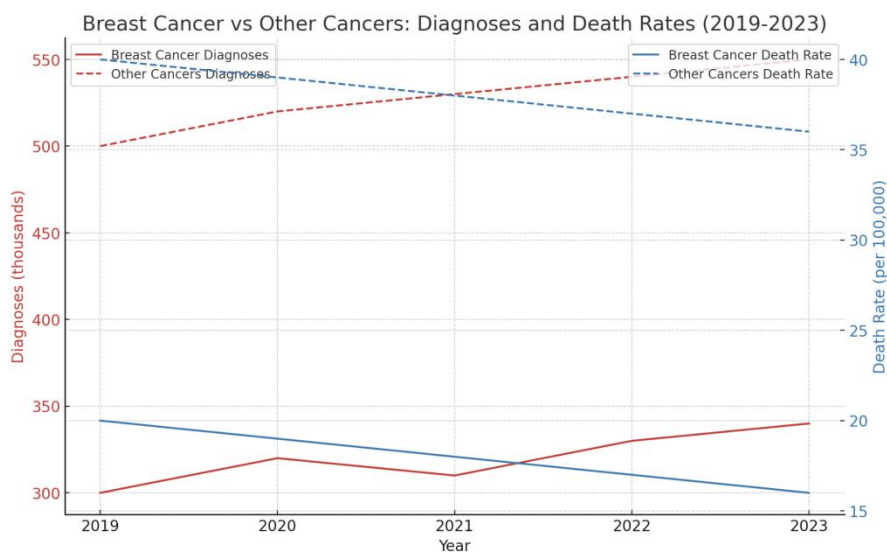


**Figure 1-1: Comparative trends in diagnosis and mortality rates for breast cancer vs. other cancers (2019-2023).**

Early detection is crucial for improving outcomes, with the World Health Organization's Global Breast Cancer Initiative working to reduce mortality [3]. While screening has proven effective for postmenopausal women and those in their forties, many younger women at risk lack access to programs such as the Screen Project, available specifically for those with a family history of BRCA1 and BRCA2 mutations [1]. Equitable healthcare demands the development of more convenient and accessible cancer prediction methods for the vulnerable young population.

Unlike lung cancer, breast cancer is not strongly associated with a single cause. Risk factors include age, family history, genetics, and lifestyle. The breast cancer 5-year net survival rate of 89% demonstrates the importance of early detection [4]. Survival rates vary based on the stage at diagnosis, with localized breast cancer having significantly higher survival rates than cancers that have spread to other parts of the body. Breast cancer has various subtypes with differing implications for treatment: 1) ductal carcinoma in situ (DCIS), a non-invasive form; 2) invasive ductal carcinoma (IDC), the most common at 80% of diagnoses; and 3) invasive lobular carcinoma (ILC) [4]. Figure 1-2 provides a visual comparison of the proportion of diagnoses and survival rates among the primary breast cancer subtypes.

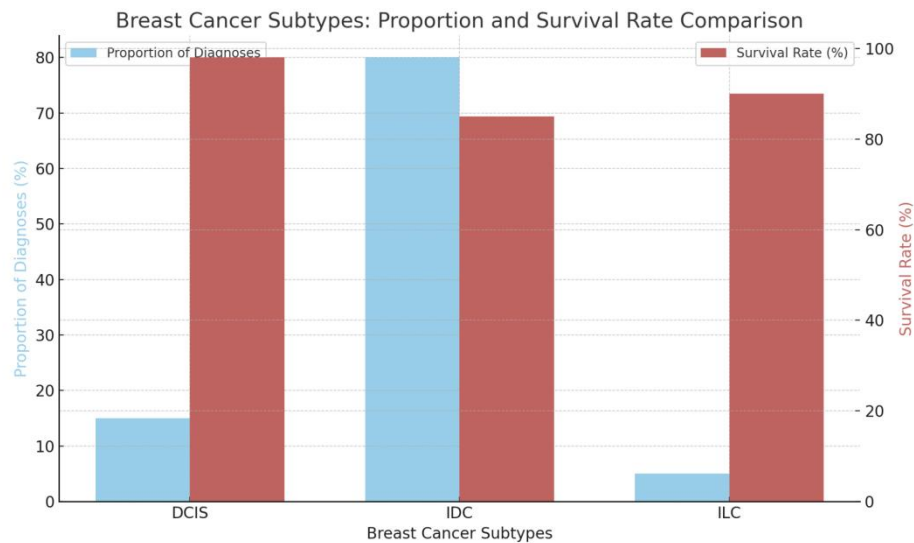


**Figure 1-2: Distribution and survival rates of breast cancer subtypes.**

Figure 1-3 is designed to show the structure and logical relationships within the 'Introduction' chapter of this thesis, visually summarizing key components and their interconnections.

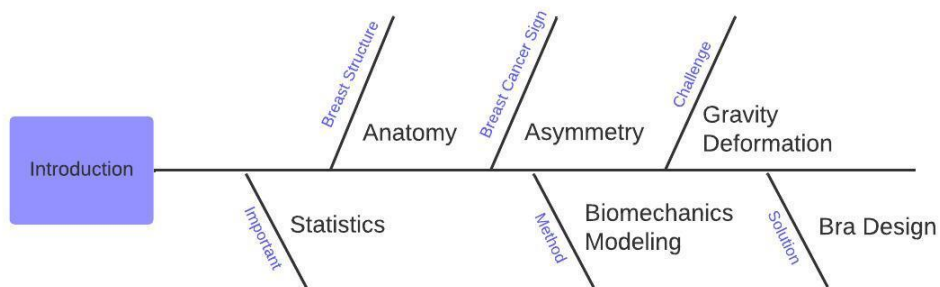


**Figure 1-3: A fishbone diagram to visualize logical structure of this thesis “Introduction” Chapter.**

### 1.1.2 Breast Anatomy and Physiology

A deep understanding of breast anatomy and physiology is crucial for analyzing how mechanical forces interact with the breast tissues. The breast is a complex organ, primarily composed of soft tissues, including glandular, fibrous, and adipose tissues, each of which plays a crucial role in the organ's overall function and response to external and internal forces. Figure 1-4 provides a detailed sagittal view of the breast anatomy, highlighting the chest wall, pectoralis muscles, lobules, nipple, fatty tissue, and skin.

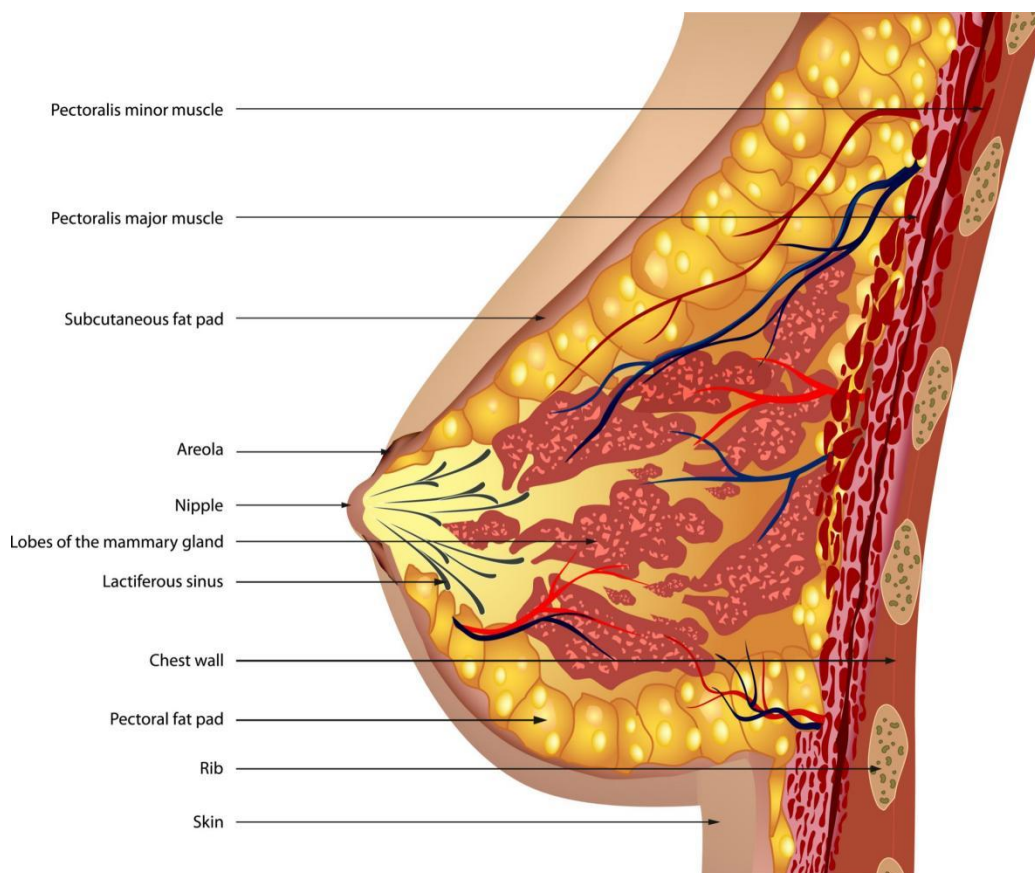


**Figure 1-4: Anatomy of the breast. (Copyright Illustration 27676555 | Breast Anatomy © Ermolaevamariya | Dreamstime.com)**

The glandular tissue is responsible for milk production at the core of the breast anatomy. This tissue is organized into lobes and lobules, with each lobe containing multiple lobules.

The lobules are milk-producing glands that connect to ducts that lead to the nipple, allowing the passage of milk [5]. The dense nature of glandular tissue contributes significantly to the overall density of the breast, a factor that influences the distribution and absorption of mechanical forces. Surrounding and supporting glandular structures are bands of fibrous tissue, also known as connective tissue. This component provides structural support and maintains the shape and integrity of the breasts. Fibrous tissue is also intertwined with glandular components, creating a scaffold that influences the biomechanical properties of the breast [6]. Its elasticity and stiffness are key factors in the response of the breast to mechanical stress, affecting the distribution of forces within the breast tissue. Adipose tissue or fatty tissue fills the spaces between glandular and fibrous tissues, contributing to the size and shape of the breast. The proportion of adipose tissue relative to fibrous and glandular tissues varies greatly among individuals and can change over time owing to factors such as age, hormonal changes, and overall body fat percentage. Adipose tissue is somewhat softer than glandular and fibrous tissues [7]. Its distribution and density play significant roles in the mechanical environment of the breast, influencing its susceptibility to stress concentrations and potential tissue deformation.

Another critical component of breast anatomy is Cooper's ligaments, a web of connective tissue that extends throughout the breast, anchoring it to the chest wall [8]. These ligaments provide additional support and help to maintain the structural integrity of the breast. However, over time or under excessive mechanical force, these ligaments can stretch, contributing to changes in the breast shape and sagging. As illustrated in Figure 1-5, the integrity of Cooper's ligaments plays a pivotal role in maintaining breast firmness, with damage or stretching of these ligaments contributing to breast sagging.

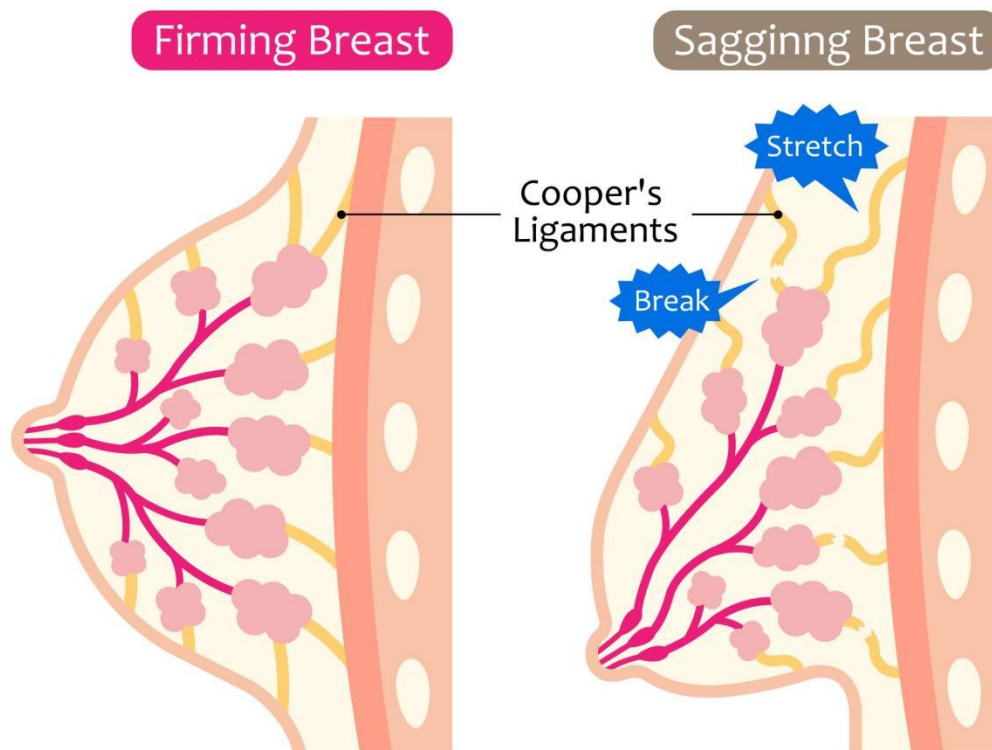


**Figure 1-5: Comparative anatomy of firming and sagging breasts highlighting Cooper's Ligaments. (Copyright Illustration 153331644 | Breast © Yomogi1 | Dreamstime.com.)**

The interplay between these diverse tissues within the breast determines how mechanical forces are experienced and managed. Factors such as tightness of clothing, posture, physical activity, and lack of proper support can introduce varying levels of mechanical stress. Over time, these forces can influence tissue remodeling, potentially affecting the risk of developing conditions such as breast pain and tissue damage, and even contributing to the etiology of breast cancer through mechanisms that are still being elucidated [7].

In summary, the intricate structure of the breast, with a mix of glandular, fibrous, and adipose tissues supported by Cooper's ligaments, creates a complex biomechanical environment. Understanding this environment, including the inherent errors introduced

by the initial stress pertaining to gravity force, is crucial for developing algorithms and exploring the interaction of mechanical forces with breast tissue. This understanding has implications for both physiological responses and potential pathological changes.

### 1.1.3 Breast Cancer and Asymmetry

A study published in the Journal of the American Medical Association found that breast bilateral asymmetry is an independent risk factor for breast cancer [9]. Another study followed over one million women and found that women with breast asymmetry had a 10% higher risk of developing breast cancer [10]. Breast tissue composition is a complex factor that influences the initiation and progression of breast cancer. The human breast is comprised of a heterogeneous mix of fibrous, glandular, and fatty tissues, with individuals exhibiting unique compositional profiles. Importantly, dense breasts, containing higher proportions of fibrous and glandular tissue, pose a significant risk of breast cancer [11]. This elevated risk is partly attributable to the limitations of conventional mammography in dense tissue, potentially obscuring malignancies and hindering early detection. In contrast, Magnetic Resonance Imaging (MRI) provides superior contrast resolution, facilitating a more accurate assessment of breast density and revealing complex compositional landscapes relevant to cancer risk [12].

Dense breast tissue presents a distinct microenvironment in which epithelial cells, the building blocks of ducts and lobules, reside in a crowded space with heightened extracellular matrix stiffness [13]. This increased stiffness exerts mechanical forces on individual cells, affecting cell shape, growth signaling, and gene expression. Importantly, chronic alterations in cellular behavior due to abnormal mechanical stress have been implicated in several hallmarks of cancer [14]. These include abnormal proliferation, evasion of the immune response, and activation of oncogenic (cancer-promoting) pathways [15]. Consequently, the dense breast environment not only obscures cancer detection but may also be an active participant in creating conditions that promote malignancy.

Emerging research has revealed how chronic mechanical stress influences breast cancer development at cellular and microenvironmental levels. Within breast tissue, forces such as those heightened by asymmetry or poorly fitting bras can concentrate in specific areas, disrupt tissue architecture, and induce potentially pathogenic changes [16]. This includes altering cell-cell interactions, extracellular matrix organization, and crucial intracellular signaling pathways [17]. Such persistent disruptions potentially drive abnormal tissue stiffening and nodule formation, well-established factors that can hinder imaging-based cancer detection and further promote carcinogenesis [11].

Similar to tissue stiffening caused by mechanical stress, it is worth noting that breast bilateral asymmetry can also have a significant impact on breast tissue structure and microenvironment. Breast bilateral asymmetry refers to asymmetry in the size, shape, position, and internal tissue distribution of the breast [9]. While every woman exhibits some degree of natural asymmetry, its potential link to breast cancer risk arises from certain dynamic or clinically apparent variations [18]. Studies suggest that asymmetries developing over time or marked discrepancies in size, shape, or tissue distribution may indicate heightened cancer susceptibility [19]. However, using the current bilateral asymmetry to predict the future development of tissue nodules is challenging. This complexity highlights an often-overlooked area in breast cancer research, where the progression from asymmetry to cancerous formation is not well understood [20]. In summary, understanding the impact of mechanical stress induced by bilateral asymmetry while a symmetric (ill-fitting) bra is worn is especially under-researched, representing a major knowledge gap, with implications for both risk assessment and exploring preventative strategies. Figure 1-6 visually represents the relationship between breast asymmetry and increased risk of breast cancer.

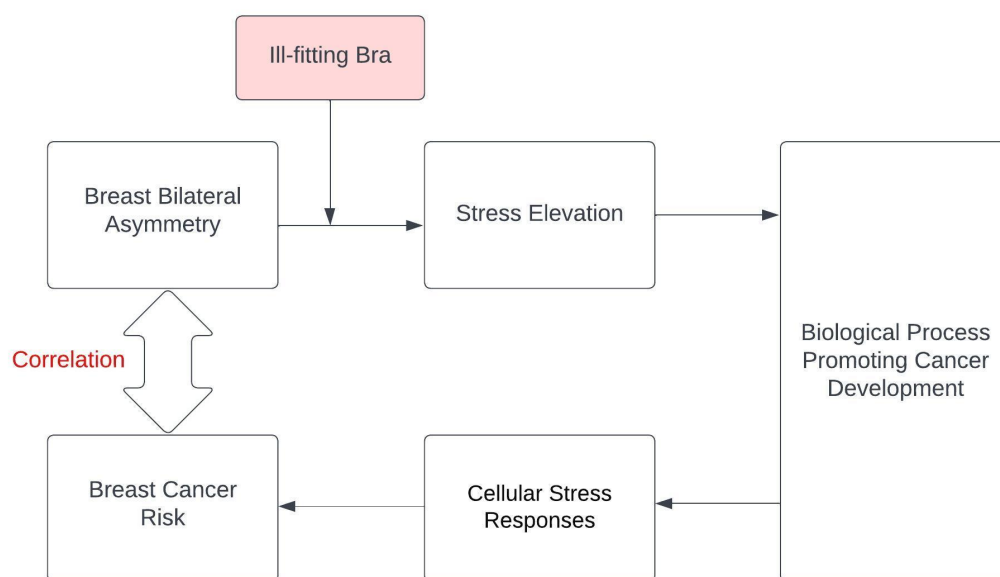


**Figure 1-6: Pathways from breast asymmetry to increased breast cancer risk.**

#### 1.1.4 Biomechanical Modeling for Breast

Biomechanical modeling plays a crucial role in breast cancer research, aiding our understanding of breast tissue structure, functionality, and mechanisms driving cancer initiation and progression. Finite-element analysis (FEA) is the most commonly used method. By employing numerical computation, FEA discretizes the complex shapes and material properties into smaller elements. Solving the individual element equilibrium equations yields an overall mechanical response. Owing to its ability to assign different material properties to individual elements, FEA is capable of simulating the complex, nonlinear, and heterogeneous nature of breast tissue and its stress-strain responses with high fidelity. This accuracy extends to the prediction of breast deformation due to external forces. In particular, the integration of biomechanically validated Virtual Reality (VR) powered by FEA modeling has revolutionized preoperative planning [21]. This synergy not only facilitates a deeper understanding of surgical procedures, but also broadens the horizon of FEA's utility, showcasing its essential role in enhancing patient engagement and decision-making processes through immersive, realistic simulations.

The accurate modeling of breast biomechanics relies on the precise characterization of its nonlinear mechanical behavior. This presents a significant challenge for breast tissue because of its complex composition and structure. Breast tissue exhibits nonlinear mechanical behavior, meaning that its response to mechanical forces is not proportional to applied stress. This behavior arises from the multi-component structure of the tissue, consisting of a heterogeneous mix of cells, extracellular matrix (ECM), and fluid [22]. The nonlinearity of breast tissue can be observed at multiple scales, from the molecular to the macroscopic level. At the microscopic level, nonlinearity arises from the interactions between individual cells and the ECM. Cells are active entities that can sense and respond to mechanical forces, and the ECM provides a complex environment that influences cellular behavior. At the macroscopic level, nonlinearity, which is attributed to the ECM constituents, manifests itself in the stress–strain response of a tissue. The stress-strain curve for breast tissue is typically nonlinear with toe, linear, and yield regions [23]. Figure 1-7 [6] shows a typical stress-strain curve. The toe region represents the initial deformation of the tissue in which the collagen fibers are stretched slightly with little impact on their coiled structure. The linear region represents the region where the tissue is elastic after the collagen fibers reach their uncoiled state where deformation is almost proportional to the applied stress. The yield region represents the region where the tissue begins to plastically deform and does not return to its original shape after stress is removed. Nonlinearity is key to accurately simulating how breast tissue deforms under various conditions, directly impacting the precision of diagnostic imaging methods, such as mammography and ultrasound. Furthermore, it significantly affects surgical planning and the design of biomedical devices by providing a more realistic representation of the tissue responses. Additionally, incorporating nonlinear behavior into models can shed light on disease mechanisms and offer deeper insights into how conditions such as cancer alter tissue properties, thereby advancing both diagnostic and therapeutic strategies.

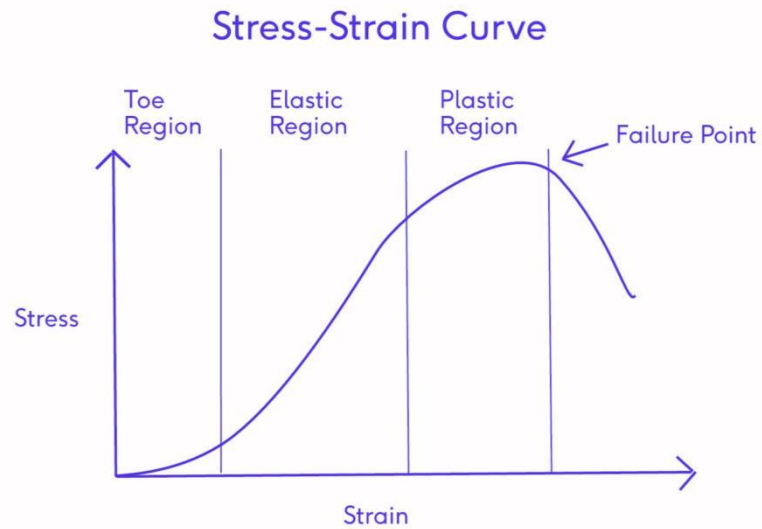


**Figure 1-7: Stress-strain curve (Figure taken from [6]).**

Given the intricate nature of breast tissue, characterized by its complex, nonlinear mechanical behavior and heterogeneous composition, significant research efforts have been devoted to developing various methodologies for mechanical testing. These efforts have led to the emergence of a diverse array of experimental techniques, both ex-vivo and in-vivo, aimed at accurately characterizing the mechanical properties of breast tissues. Table 1-1 offers an intuitive summary of the literature for each mechanical test type.

**Table 1-1: Overview of mechanical testing methods for breast tissue.**

Test Type	Experimental Condition	Number of Related Researches	Representative Author
Elastography Techniques	In-vivo	9	Ophir et al. (1991) [24]

Magnetic Resonance Elastography	In-vivo	10	Sinkus et al. (2000) [25]
Optical Coherence Tomographic Elastography	In-vivo	1	Srivastava et al. (2011) [26]
Uniaxial Compression and Punch Indentation	Ex-vivo	7	Krouskop et al. (1998) [23]

However, despite these advancements, the methodologies currently available for the mechanical testing of breast tissue face several challenges. One of the primary concerns is the difficulty in obtaining reliable hyperelastic parameters, particularly in the unloaded state of the tissue [27]. This issue is compounded by the variability in tissue response due to individual differences as well as the potential for tissue damage during testing, which can lead to inaccuracies in the derived parameters [28]. Furthermore, the complex interplay of different tissue components at various scales adds another layer of complexity to the accurate modeling of breast tissue mechanics [29].

Machine learning has emerged as a potential game-changer. By leveraging its advanced capabilities in pattern recognition and data analysis, machine learning offers a novel approach for refining the hyperelastic parameters. It can systematically analyze the vast amounts of data generated from mechanical tests, identify underlying patterns, and establish robust relationships between measurable variables and model parameters [30]. This not only streamlines the process of parameter tuning but also opens new avenues for improving the accuracy and reliability of biomechanical models.

### 1.1.5 Breast Gravitational Deformation

Breast deformation under gravity is a complex process that is significantly influenced by the unique composition and heterogeneity of breast tissues. The breast consists of glandular, adipose, and connective tissues, each with distinct mechanical properties that respond differently to gravity. This variance in tissue response is a pivotal factor in the biomechanical behavior of the breast, leading to differential displacement and strain across tissue types when subjected to a consistent gravitational field[30]. Biomechanical models have shed light on this nonuniformity, demonstrating how variable deformation across different tissue types complicates the prediction of overall breast deformation. The challenge lies in the inability of simplistic mathematical models to accurately capture the nuanced interplay of forces within the complex structure of the breast, necessitating more sophisticated approaches to predict and understand the deformation patterns.

The role of Cooper's ligaments in breast mechanics is to provide structural support against gravitational forces, acting as natural suspensory structures that help maintain the breast shape. However, the effectiveness of these ligaments in countering gravitational stress diminishes with increased breast size, leading to exacerbated strain on Cooper's ligaments and surrounding tissues over time. In the context of breast modeling for various biomedical applications, accuracy requires availability of stress-free reference geometry of the breast and its mechanical properties. Since the breast tissue is known to be hyperelastic with substantial nonlinearity, using the breast geometry based on images inevitably acquired under gravity forces lead to model unreliability. The increased biomechanical stress may lead to progressive deformation of the breast and can contribute to changes in the internal architecture of breast tissue. Such alterations are not merely cosmetic concerns but have been suggested to influence the development of certain pathologies, including breast cancer. Therefore, adequate breast support extends beyond comfort and aesthetics to play a crucial role in the biomechanical integrity of the breast. Properly fitted bras can offer significant support and stability, helping distribute and mitigate the stresses imposed by gravity. By providing a counterforce to the gravitational pull, a well-designed bra can help maintain breast shape, reduce strain on

Cooper's ligaments, and potentially minimize the biomechanical stresses that contribute to tissue deformation and the evolution of breast pathologies.

In conclusion, understanding the biomechanical response of the breast to gravity requires a multifaceted approach that considers the unique properties of breast tissues and the potential for external support mechanisms such as bras to influence the breast mechanics. This comprehensive perspective is essential for developing interventions that can effectively support the breast, preserve its biomechanical integrity, and reduce the risk of deformation-related pathologies.

### 1.1.6 Bra Design

Bras are designed to contain and support the breasts and shield them from movement triggered by daily activities. A woman wears a bra for an average of 8-10 hours a day [31]. A comfortable and supportive bra relies on finding a perfect fit. Unfortunately, research shows that a staggering number of women wear the wrong bra size [32]. This is not only about comfort as a poorly fitting bra can lead to serious health problems, such as nerve pain, back and neck aches, poor posture, difficulty during exercise, and increase in the risk of future development of breast cancer. In severe cases, women with large breasts may even turn to reduction surgery. Off-the-shelf bras, which are designed based on symmetrical breasts standards, fail to accommodate the widespread prevalence of breast bilateral asymmetry in women. "Bilateral asymmetry problem" means that if the bra is chosen based on fitting the larger breast, the smaller breast may sag, whereas if it is chosen to fit the smaller breast, the larger breast may suffer from excessive compression. The consequences of ill-fitting bras are particularly concerning for women who have undergone breast mastectomy or lumpectomy surgery, as they may already experience significant changes in breast appearance, density, and sensitivity.

There is still no unified standard for bra cup shape measurements. Current bra cup design methods prioritize aesthetics rather than pressure analysis. The first approach, which focuses on appearance, is commonly used in breast implant procedures [33]. The second

approach involves analyzing the pressure distribution of breast tissue under different bra cup shapes [34]. However, few studies have explored bra cup design from the perspective of the breast itself, aiming for an optimal fit, uniform stress distribution, and prevention of chronic stress related damage. This research direction is particularly important for preventing tissue hyperplasia in large breasts, particularly in those with significant bilateral asymmetry. Biomechanical modeling and stress analysis offer promising solutions for shaping challenges. By creating digital simulations of breast mechanics, these tools can map the areas of potential elevated stress caused by different bra shapes. This information can be used to create customized brands that offer optimal support and minimize discomfort. This synergistic study has the potential to improve comfort, reduce pain, and promote healthy tissue recovery after breast surgery.

## 1.2 « Theory »

This thesis draws from multiple background topics. This section offers a summary of these foundational concepts.

### 1.2.1 Magnetic Resonance Imaging

Magnetic resonance imaging (MRI) is a medical imaging technique that leverages powerful magnetic fields and radiofrequency (RF) pulses to generate detailed images of the body's internal structures [35]. Under a strong magnetic field, the hydrogen nuclei within the body align their magnetic moments, forming a net magnetization vector. A precisely timed RF pulse disrupts this alignment by causing nuclei to absorb energy and flip their orientation. After the RF pulse ceases, the hydrogen nuclei return to their original state via a process called relaxation. This relaxation releases energy, which is detected by an RF receiver coil and used to construct an MR image [36]. The distinct relaxation times of different tissues, along with variations in the hydrogen density, create an image contrast that makes MRI exceptionally valuable for diagnostic purposes.

MRI is a powerful medical imaging technique for the detection of breast cancer and other breast diseases. Different breast tissues have distinct appearances on MRI: fat tissue shows a high signal on T1-weighted images, appearing bright white, whereas glandular tissue exhibits an intermediate signal, appearing gray-white. Fibrous tissue presents with a low signal, appearing black, and ducts display a high signal, appearing bright white. Breast tumors, on the other hand, typically manifest as a high-signal mass on T1-weighted images, appearing bright white [37]. Figure 1-8 presents a breast MRI scan, where the radiologist identified a region of interest with a white arrow, indicating the presence of a cancerous lesion.

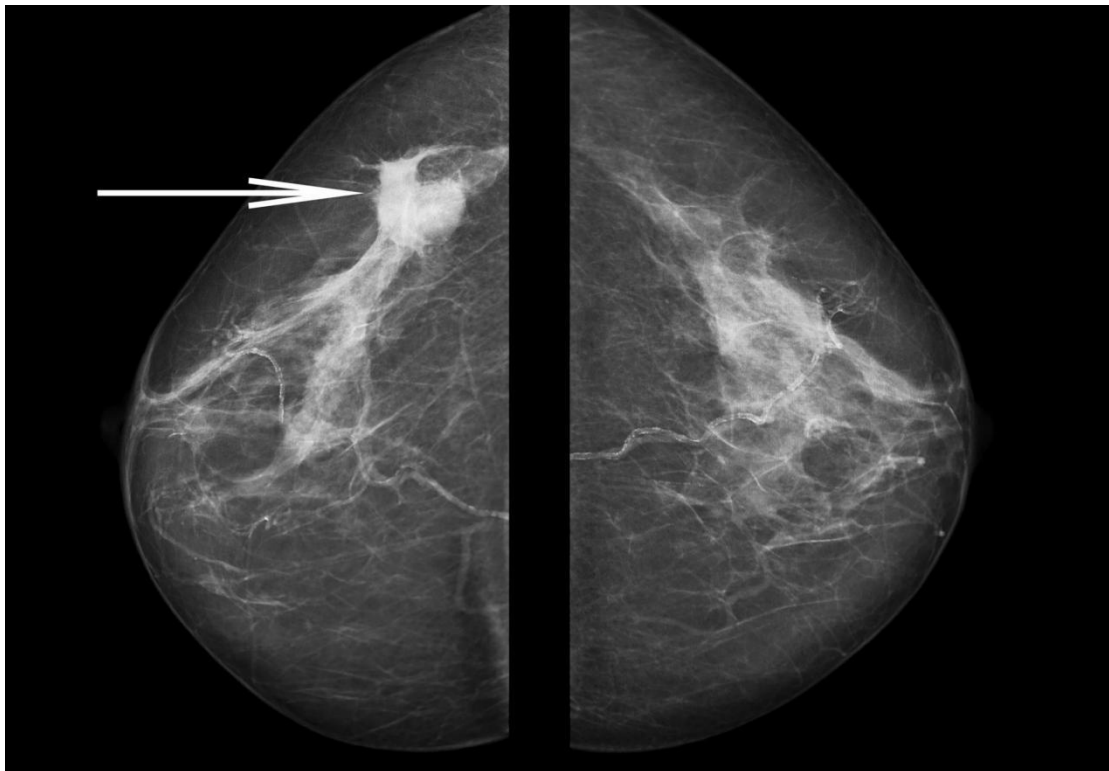


**Figure 1-8: Breast MRI scan of a cancerous lesion.**

For breast MRI, specifically, the contrast between different tissues and potential abnormalities, such as tumors, is enhanced through the use of contrast agents. Contrast

agents affect the relaxation times of the tissues, making the affected tissues appear brighter on T1-weighted images. This is described by the equation for signal intensity with contrast agent  $C$ :

$$S_{contrast} = \rho \left(1 - e^{-\frac{TR}{T_1+C}}\right) e^{-\frac{TE}{T_2}} \quad (1-1)$$

$C$  is the effect of the contrast agent on the T1 relaxation time. Radiologists diagnose breast cancer by considering factors such as signal intensity, tumor morphology (irregular shapes and indistinct borders suggesting malignancy), and contrast enhancement [38]. While MRI offers advantages such as high sensitivity and being radiation-free, it has limitations. Image artifacts caused by motion or metal implants as well as partial tissue loss due to the slice-by-slice imaging nature of MRI are potential drawbacks. These limitations can lead to false-positive results in the diagnosis of breast cancer [39].

### 1.2.2 Tissue Biomechanics

Soft tissues are the foundational building blocks of biological organisms that provide various physiological functions, including motion generation, hormone production, milk production etc. Examples include muscles, tendons, skin, and glandular tissues. Unlike rigid materials such as metals or ceramics, soft tissues exhibit several unique characteristics due to their high deformability.

**Stress-strain Relationship:** Soft tissues exhibit mechanical behaviors distinct from traditional engineering materials. Their response to stress (a measure of internal force per unit area, denoted as  $\sigma$ ) and strain (the relative deformation they experience denoted as  $\epsilon$ ), is represented by more complex models such as hyperelasticity, where the stress-strain relationship is given by a strain energy density function  $W$  that can be integrated to obtain the stress:

$$\sigma = \frac{\partial W}{\partial \epsilon} \quad (1-2)$$

**Nonlinearity:** Soft tissues generally do not follow a linear stress-strain relationship (Hooke's Law). Instead, they stiffen as they deform. The nonlinearity of soft tissues such as breast tissue can be represented mathematically by a nonlinear stress-strain curve, which is often described by the Neo-Hookean, Yeoh or other hyperelastic models [40]. The Neo-Hookean model can be expressed by the strain energy function  $W$ , which is a function of the invariants of the deformation gradient tensor. For incompressible materials, the simplified form of the Neo-Hookean model is:

$$W = \frac{\mu}{2}(I_1 - 3) \quad (1-3)$$

where  $W$  is the strain energy per unit of the reference volume,  $\mu$  is the initial shear modulus, and  $I_1$  is the first invariant of the Cauchy-Green deformation tensor, which is related to the strain in the material.

**Hyperelasticity:** Soft-tissue materials exhibit nonlinear behavior under external loading, deviating from the linear elastic response. This nonlinearity arises from two mechanisms:

**Intrinsic nonlinearity:** Stems from inherent material properties, leading to a nonlinear relationship between the Cauchy stresses and strain tensor components.

**Geometric nonlinearity:** Large deformations (strains >5%) alter the internal force distribution within the material, thereby changing its mechanical response.

In these materials, the strain energy function characterizes the behavior because the work done during deformation can be stored as elastic energy. This strain energy function ( $U(F)$ ) is defined in the deformation gradient ( $F$ ) space (energy per unit volume). The constitutive law is derived from it:

$$\boldsymbol{\sigma} = J^{-1} \mathbf{F} \frac{dU(\mathbf{F})}{d\mathbf{F}} \quad (1-4)$$

For isotropic hyperelastic materials, the constitutive law for isotropic hyperelastic materials:

$$\boldsymbol{\sigma} = 2J^{-1} \left[ I_3 \frac{\partial U}{\partial I_3} \mathbf{I} + \left( \frac{\partial U}{\partial I_1} + I_1 \frac{\partial U}{\partial I_2} \right) \mathbf{B} - \frac{\partial U}{\partial I_2} \mathbf{B}^2 \right] \quad (1-5)$$

where  $\mathbf{B}$  is the left Cauchy-Green deformation tensor:

$$\mathbf{B} = \mathbf{F} \mathbf{F}^T \quad (1-6)$$

$I_1, I_2, I_3$  are strain invariants of the deformation tensor. The strain energy function ( $U$ ) depends on the strain invariants. Different hyperelastic models exist, each with a unique strain energy function, chosen to match the mechanical test data of a specific material. In this project, the Yeoh and the 1<sup>st</sup> Ogden hyperelastic formula was chosen to model breast tissue behavior, and corresponding strain energy functions are described in Chapter 3.

## 1.3 « Literature Review »

### 1.3.1 Breast Cancer Assessment based on Bilateral Asymmetry

According to the fourth edition of the Breast Imaging Reporting and Data System (BI-RADS) [41], bilateral asymmetry is one of the four subtle signs of breast cancer. Various studies have demonstrated its potential in improving detection and risk assessment. The conventional diagnosis of breast asymmetry relies heavily on the doctor's experience. This can contribute to both unnecessary recall and missed breast cancer diagnosis. Additionally, overlapping breast tissues can obscure asymmetric lesions, making them difficult to detect, especially in dense breasts. Many Machine Learning-based breast cancer diagnosis methods have been proposed to address this limitation. One approach leverages sequential mammograms analyzed via deep learning to detect masses and microcalcifications within paired mammograms [42]. This method innovatively integrates breast asymmetry evaluation to refine the cancer classification and detection

accuracy. A contrasting methodology employs a non-learning-based strategy [43]. Using breast thermograms and bilateral symmetry analysis, this technique offers effective abnormality detection with 92% accuracy, providing an independent alternative to complex deep learning models. Another valuable development highlights the crucial role of multi-modality diagnostics [44]. Researchers emphasize correlating ultrasound, MRI, and histopathological findings in patients showing the development of mammographic asymmetry. Such thorough investigations can significantly aid in the determination of malignancy. These integrated and computationally driven approaches demonstrate outstanding potential for optimizing the accuracy and early detection of breast cancer through a sophisticated bilateral asymmetry analysis. Alongside the advancements in asymmetry-focused breast cancer prediction methods, researchers have pinpointed potential areas for ongoing enhancement. [45] developed bilateral asymmetry-driven breast cancer detection by introducing thermal imaging to the paradigm and highlighting texture feature relevance. They examined various classification models (SVM, Decision Tree, etc.) for thermogram assessment based on textural features and thermal imaging. [46] developed a short-term breast cancer risk model by employing both global and local asymmetry characteristics in mammograms. [47] focused on segmentation in an asymmetry-focused analysis to refine cancer risk prediction. [48] developed a deep learning model specifically for the detection of malignant breast lesions in digital mammograms of Asian women. Other researchers [49-54] are involved heavily in developing deep-learning algorithms specifically for breast cancer detection within mammograms.

Although these studies have shown promising results, some limitations still need to be addressed. First, most studies focus only on the detection of current cancer and do not predict future cancer risk, precluding meeting the needs of early prevention and intervention. Second, many deep learning studies rely on large amounts of data, which are generally lacking in the medical field, resulting in insufficient model generalization ability and difficulty in application to actual scenarios. In addition, traditional supervised machine learning methods rely on manually designed features, which not only consume a lot of manpower but also have strong subjectivity, resulting in poor model robustness and difficulty in further application. To further improve the scalability and reliability of breast

cancer prediction, future research needs to: (1) develop models that can predict future cancer risk to help high-risk groups in early prevention and intervention; (2) explore unsupervised learning or weakly supervised learning methods to alleviate the dependence on labeled data and improve the generalization ability of the model; and (3) research more robust and interpretable feature extraction methods to improve the performance and reliability of the model. Nevertheless, these studies provide strong evidence that bilateral asymmetry analysis can be a valuable tool for breast cancer prediction and early detection.

### 1.3.2 Biomechanical Properties of Breast Tissue

Biomechanical breast models, which primarily use finite-element methods, can predict breast deformation under various conditions. They have been used to guide clinical biopsies [55], simulate the compression of X-ray mammography [56], combine X-ray and MR mammograms, test image registration algorithms [57], and evaluate elastography reconstruction techniques [58]. These mechanical models offer vital insights into how breasts are expected to deform. Capturing the nonlinear, large-strain behavior exhibited by breast tissue necessitates the use of hyperelastic constitutive models. Researchers have used widely differing values to represent the material properties of breast tissue in biomechanical models. Experimental tests to determine the mechanical properties of breast tissue fall into two main categories: in-vivo (conducted on a living person) which often employ imaging and ex-vivo (performed on tissue samples removed from the body) which use mechanical stimulation such as compression or indentation.

In-vivo methods offer a unique opportunity to calculate the mechanical properties of breast tissue in its natural environment. Imaging techniques, such as elastography, play a crucial role. These methods typically involve applying a controlled force or deformation to the breast, and then using medical imaging to track the tissue response. For example, in ultrasound elastography, images reveal how tissues deform under compression, with less deformation indicating stiffer regions. By analyzing tissue displacement images with sophisticated algorithms, researchers can map out variations in stiffness, translating that information into quantitative measures of mechanical properties such as the elastic

modulus. MR has demonstrated significant potential for the assessment of breast tissue properties in-vivo. Early work by Lawrence et al. (1998) [59] confirmed its feasibility, accurately mapping breast tissue stiffness, and revealed that glandular tissue is stiffer ( $2.45 \pm 0.2$  kPa) than adipose tissue ( $0.43 \pm 0.07$  kPa). Subsequent research established the capacity of MR elastography to distinguish benign and malignant tumors, with malignant tissues consistently exhibiting higher elasticity [60-62]. Ultrasound (US) elastography is a complementary technique. Sayed et al. (2013) [63] demonstrated its diagnostic capabilities, with tumors appearing significantly stiffer than the normal tissues. Han et al. (2003) [64] revealed the viscoelastic nature of breast tissue using US elastography, emphasizing the need for preconditioning during testing to ensure consistent results. Barr and Zhang (2012) [65] investigated how precompression levels during elastography impact results. They determined that a slight precompression (approximately 10%) maximized the contrast between normal and tumor tissue stiffness and improved tumor detection accuracy. Elastography, especially MR elastography, provides valuable insights into the mechanical properties of breast tissue. Variations in stiffness offer a powerful tool for differentiating healthy, benign, and malignant tissues.

Ex-vivo experiments, such as uniaxial and indentation tests, offer valuable insights into how factors such as precompression influence the mechanical behavior of soft tissues [66-67]. These tests measure the displacement and force, which can then be used to calculate the Young's modulus. Uniaxial tests can be hindered by irregularities in the sample geometry and the difficulty in preparing uniform specimens without causing damage. For the initial analysis, researchers often simplify the assumption that tissues are elastic, isotropic, and near-incompressible to estimate the elastic modulus [68-69]. Sarvazyan et al. (1995) [70] found fibroadenomas and malignant tissues to be significantly stiffer than normal tissues. Krouskop et al. (1998) [71] observed that adipose tissue is the softest, with malignant tissues (particularly IDC) exhibiting the highest stiffness. Importantly, this stiffness increased nonlinearly with the precompression. This nonlinear behavior is underscored by Samani et al. (2003, 2007) [72][45], whose findings highlight that stiffness differences between tissue types are most pronounced at high strains. Matsumura et al. (2009) [72] and Umemoto et al. (2014) [73] further emphasized this non-linearity, noting that while malignant tissues are generally stiffer, the contrast

with normal tissue stiffness decreases as applied stress increases, likely due to normal tissues' higher non-linearity.

However, under large deformations, the viscoelastic nature of these tissues became apparent. This means that their mechanical response depends on the duration of the applied load (visco), and they recover their initial state after load removal (elastic), indicating the absence of permanent damage [74]. By combining indentation tests and inverse FE modeling, Samani and Plewes (2004) [75] successfully measured the hyperelastic properties of adipose and fibroglandular breast tissues. Dempsey et al. (2021) [76] found no significant differences between the hyperelastic properties of adipose, fibroglandular, and mixed breast tissues, supporting the use of homogenous models for large strain simulations. Sun et al. [77-78] characterized adipose tissue's hyperelastic behavior, highlighting similarities between human and porcine samples and emphasizing the suitability of the Ogden hyperelastic model for representing these complex tissues.

There is no single agreed-upon model with various researchers favoring exponential, hyperelastic, or even linear elastic models. These choices led to different material parameters in the models. Nearly all recent researchers have assumed that the materials are quasi-incompressible (i.e., their volume hardly changes when deformed). Tanner et al. [79] found that the exact ratio of stiffness between fatty and glandular tissue has minimal impact on the model's accuracy. Some researchers assume that the skin behaves in a simple linear elastic fashion for deformations below 50% [38]. Others acknowledge that skin properties such as anisotropy (having different responses based on the direction of force) is location dependent [80]. Tanner et al. [81] concluded that for moderate compression (20%), the choice of material properties matters less for breast model accuracy than ensuring the model accurately represents how the breast interacts with its surroundings. Using accurate surface displacement data, they achieved landmark prediction errors under 2.5 mm.

Classic hyperelastic models provide a critical tool for the biomechanical characterization of breast tissue. Although newer models are continually emerging Yeoh [82], Ogden [83] and Veronda-Westmann models [84] remain powerful choices, facilitating advancements

in breast health interventions. However, it is worth noting that the aforementioned models do not consider the inherent initial stress present in the breast tissue. This preloading can arise from various factors such as tissue growth, remodeling, and the presence of tumors. Ignoring this residual stress can lead to inaccuracies in model predictions and potentially affect the outcomes of clinical applications.

### 1.3.3 Stress Concentration and Cancer Risk

The interplay between mechanical stress and cancer risk is a critical area of investigation that bridges the fields of biomechanics and oncology. Central to this field of study is the concept of stress concentration, a condition in which mechanical stress is disproportionately distributed within a material or tissue, leading to localized areas of high strain. In the context of breast tissue, such stress concentrations can arise from various sources, including physical compression, gravitational forces, and constriction imposed by ill-fitting bras. Research has shown that mechanical stress can induce a cellular response through mechanotransduction, whereby mechanical signals are converted into biochemical signals [85]. This process can lead to the activation of oncogenes and suppression of tumor suppressor genes, thereby promoting tumorigenesis. For example, studies [86] have demonstrated that sustained mechanical compression of mammary tissues can lead to increased epithelial density, which is a known risk factor for breast cancer. This density can create an environment conducive to cellular anomalies by physically constraining normal cell movement and function, thereby facilitating the accumulation of genetic mutations. Beyond its direct effect on cellular structures, mechanical stress influences the breast tissue microenvironment, which is an essential factor in cancer progression. An altered mechanical environment can promote inflammation, a critical mediator of tumorigenesis [87]. Chronic inflammation has been associated with a range of cellular changes conducive to cancer development, including DNA damage, promotion of angiogenesis, and suppression of apoptosis.

Mechanical stress can also affect the extracellular matrix (ECM), a complex network of proteins and fibers that surrounds and supports cells. Changes in ECM stiffness and

composition driven by uneven stress distribution can alter cellular behavior in ways that promote cancer. For example, increased ECM stiffness has been linked to enhanced cell proliferation and migration, which are integral to cancer invasion and metastasis. Furthermore, remodeling of the ECM under mechanical stress can release growth factors and other signaling molecules trapped within the matrix, further stimulating tumor growth and progression. A growing body of empirical evidence supports the hypothesis that mechanical stress contributes to cancer risk. For example, Plodinec et al. [88] highlighted the role of ECM stiffness in breast cancer progression, illustrating how the biomechanical properties of the tumor microenvironment influence cellular dynamics and cancer outcomes. Similarly, Butcher et al. [89] explored how mechanical forces modulate angiogenesis within the tumor microenvironment, offering insights into how stress-induced changes in vascularization could support tumor growth and spread.

### 1.3.4 Bra Shape Optimization

The use of the Finite Element method (FEM) to analyze the stress distribution induced by the breast-bra mechanical contact and refine the bra shape to achieve desirable stress distribution based on the analysis results is an emerging research area. This approach can provide more accurate information about stress distribution, which can help in designing bras that are more fit, comfortable, and effectively support breasts. Early work such as Bingham et al. (2005) who designed layered garment model [90] highlighted this potential, even though its development has stalled. Bel-Brunon et al. (2014) [91] demonstrated FEM's capabilities for studying bra stress distribution under various conditions, including movement. Their model incorporated deformable skin and breast elements, with parameters informed by experimental data. Some studies [92-94] indicate that material matters much: stiffer bra cup materials offer enhanced breast reshaping and may reduce neck pressure. However, there is a trade-off: potentially greater pressure towards the breast base [95]. Research has highlighted the need to balance rigidity with breathability and overall wear comfort. [96] proposed underwired bras that demonstrate superior shaping abilities compared to their wireless counterparts, but this comes at the cost of increased breast pressure. Their findings underscore the importance of

personalizing fit with individual preferences. [97] utilized numerical modeling aids to explore the impact of specific bra fabric parameters on the pressure distribution and shaping. Through simulations, diverse materials and construction methods can be virtually tested without the need for costly iterations of physical prototypes. Some researchers have advanced tools for design optimization using criteria such as limited strain, making them more stable under conditions that simulate real-world wear dynamics [98]. FEA method addresses several key challenges within the intimate apparel field, including the nonlinear behavior of breast tissue, varying properties of bra cup materials, and complex body-bra interactions [99]. Zhang pioneered the use of finite element (FE) methods in numerically modeling the body and garments [100]. However, their work treated the body as a rigid object and focused on fabric properties, limiting its realism in garment design. Wang [101] built an FE contact model based on the Mindlin-Reissner shell theory, revealing the influence of fabric materials on garment fit. Similar studies have used FE modeling to analyze the relationship between fabric choices and fit in other garments, such as socks and insoles [102-104].

## 1.4 « Objectives »

The overarching objective of this study was to improve the survival rate and quality of life of women at high risk of breast cancer by informing them of their high risk and mitigating it by designing custom-made bras to prevent tissue stress concentration. Once developed, the methods will be applied to a cohort of women with varying degrees of asymmetry who have undergone comprehensive MRI. The results of this study can be used to establish quantitative links between breast mechanics, customized bra design, and future breast cancer risk assessment.

The focus of our work is on developing MRI-driven, patient-specific models of breast biomechanics, where asymmetry is a central consideration. The first specific aim of the research included in this thesis was to develop a machine learning algorithm that classifies breast asymmetry using MRI and correlates it with breast cancer risk. The second specific aim focuses on the structural inverse problem of determining an

individual's state-free breast biomechanics. In this study, we developed two separate but interconnected neural networks to reconstruct the unloaded hyperelastic tissue parameters and undeformed breast geometry from MRI images. The third specific aim was to establish an optimization framework for tailored bra design that minimizes stress concentrations in breast tissue by considering tissue properties, breast geometry, and textile characteristics.

## 1.5 « Thesis Outline »

### 1.5.1 Thesis Overview

This thesis is structured to elucidate a strategic approach for identifying individuals at a heightened risk of breast cancer and to develop methodologies that effectively minimize this risk. Chapter 2 identifies these high-risk groups through clustering techniques by analyzing MRI data to classify bilateral breast asymmetry, a critical, yet underexplored indicator of long-term cancer risk. Subsequently, three interlinked methodologies to address this risk are developed in Chapters 3, 4, and 5. Chapter 3 introduces a computational technique to precisely calculate breast tissue properties under state-free conditions. This detailed understanding of breast tissue is then applied in Chapter 4 to reconstruct the breast's undeformed geometry of state-free condition, which provides a reference geometry for Chapter 5. This chapter is geared toward custom-made bra design specific for the group of individuals classified as high risk individuals according to the algorithms developed in Chapter 2. The design criteria in this chapter is minimizing breast tissue local stress resulting from wearing the bra, hence directly addressing the risks identified in Chapter 2. Each chapter intricately builds upon the previous one, ensuring a comprehensive approach to risk assessment and mitigation, tied together through innovative technological advancements. A structural diagram Figure 1-9 is presented to illustrate the logical relationships between these chapters, further clarifying the progression and integration of methodologies throughout the thesis.

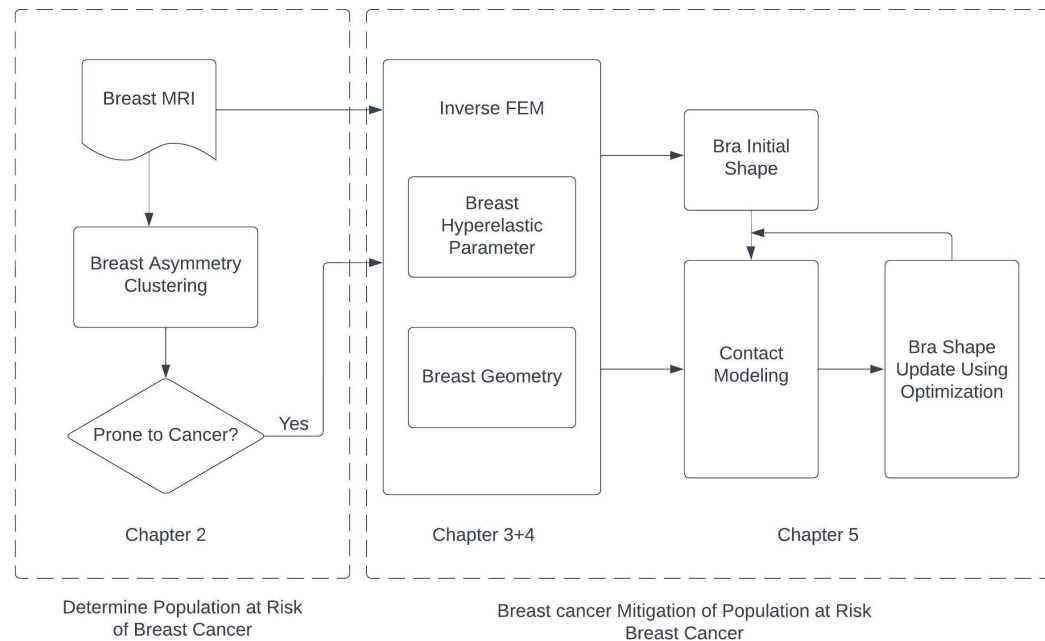


**Figure 1-9: Logical flow diagram of thesis structure and methodology development.**

This thesis addresses the objectives outlined in the subsequent sections. The final section concludes the thesis with a summary and proposes future research directions. The organization of each chapter is as follows.

### 1.5.2 Chapter 2

In the early detection of breast cancer, bilateral breast asymmetry, assessed primarily based on magnetic resonance imaging (MRI), is an important but underutilized indicator. Previous studies have shown a strong correlation between asymmetry and increased breast cancer risk in the long-term. Furthermore, most existing methods rely on supervised learning techniques, which require extensive labeled data and only focus on predicting the presence of already-developed cancerous tissue rather than long-term risk assessment. To account for these limitations, a novel unsupervised clustering method was developed to assess breast cancer risk based on longitudinal bilateral MRI data, focusing

on bilateral asymmetry classification. In this chapter, we present a novel unsupervised clustering machine learning technique developed for breast bilateral asymmetry classification and risk prediction. For a comprehensive MRI analysis, the model was developed and trained on a two-level feature space: volume-by-volume and slice-by-slice for clustering. Model validation employed cross-validation with sequentially labeled MRI data (positive/negative). The results demonstrated significant clustering improvements in accuracy and effectiveness for predicting future breast cancer risk.

### 1.5.3 Chapter 3

In this chapter, an innovative computational inversion technique to calculate patient-specific breast tissue properties under stress-free conditions is introduced. To address the inaccuracies introduced by gravity preloading, this approach focuses on determining 'preloading-free' parameters, which are essential for enhanced breast biomechanical modeling. First, a comprehensive database covering the complete unloaded parameter space was constructed. The experimental uniaxial testing data were used to inversely populate the corresponding loaded parameter space. Next, a parameter-estimation neural network was trained to calculate the unloaded counterparts using the loaded breast tissue parameters. The technique was utilized using data acquired from previous studies in our laboratory, and the results verified its efficacy in subsequent breast geometry reconstruction (Chapter 4) and bra design efforts (Chapter 5). To the best of our knowledge, this represents an easily implemented machine-learning-based algorithm addressing the determination of stress-free hyperelastic tissue parameters in an effective way.

### 1.5.4 Chapter 4

In this chapter, we further developed the methodology from the previous chapter to obtain the undeformed shape of the breast using breast MRI data which is acquired under gravity loaded state. First, two shape spaces were created to represent the loaded and unloaded breast geometries using their surface point clouds. The unloaded space was constructed using the unloaded hyperelastic parameters (obtained in Chapter 3) combined with non-isotropic scaling, implemented via finite element modeling (FEM). A spatial

configuration neural network was then trained to reconstruct the unloaded geometry based on its loaded counterpart. The technique was validated using a reverse method where the reconstructed unloaded geometry was loaded with gravity and compared to the original MRI model. The results demonstrate the ability of the technique to accurately reconstruct undeformed breast geometry. This technique is important for establishing a more precise reference as the starting shape to be loaded through FE modeling for bra design, ultimately leading to improved comfort and support.

### 1.5.5 Chapter 5

In this section, preliminary work carried out on an optimization framework for bra shape design is presented, which focuses on breast stress uniformity. Other studies often rely on 3D scans of breasts already wearing bras, ignoring the initial unloaded state and the subsequent preloading effects. This technique uniquely incorporates patient-specific unloaded breast geometry (obtained in Chapter 4) and hyperelastic tissue parameters (calculated in Chapter 3), yielding more individualized solutions. The technique leverages the ability of the breast tissue to conform to a custom-fitted bra while ensuring that the stress remains within a healthy range through iterative design optimization.

### 1.5.6 Chapter 6

This chapter provides a concise summary of this dissertation's core contributions. The potential of this research was explored by proposing potentially impactful directions for future investigations.

## References

- [1] Canadian Cancer Society. (2023). Breast cancer statistics.
- [2] Women's College Research Institute. (2024).
- [3] World Health Organization. (2023). Global Breast Cancer Initiative.
- [4] American Cancer Society. (2023). Breast cancer statistics.

- [5] Bissell, M. J., Weaver, V. M., Lelièvre, S. A., Wang, F., Petersen, O. W., & Schmeichel, K. L. (1999). Tissue structure, nuclear organization, and gene expression in normal and malignant breast. *Cancer research*, 59(7\_Supplement), 1757s-1764s.
- [6] Fung, Y. C. (1993). *Biomechanics: Mechanical properties of living tissues*. New York: Springer Science & Business Media.
- [7] Ramsay, D. T., Kent, J. C., Hartmann, R. A., & Hartmann, P. E. (2005). Anatomy of the lactating human breast redefined with ultrasound imaging. *Journal of anatomy*, 206(6), 525-534.
- [8] Holzapfel, G. A., & Ogden, R. W. (2009). *Mechanics of biological materials*. New York: Springer Science & Business Media.
- [9] Scutt, D., Lancaster, G. A., & Manning, J. T. (2006). Breast asymmetry and predisposition to breast cancer. *Breast Cancer Research*, 8(1), R14.  
<https://doi.org/10.1186/bcr1388>.
- [10] Li, W.-Q., Shu, X.-O., Zheng, W.-W., et al. (2014). Breast asymmetry and risk of breast cancer: A meta-analysis of prospective cohort studies. *JAMA*, 312(16), 1642-1650.  
doi:10.1001/jama.2014.12779
- [11] Duffy, S. W., Morrish, O. W. E., Allgood, P. C., et al. (2018). Mammographic density and breast cancer risk in breast screening assessment cases and women with a family history of breast cancer. *European Journal of Cancer*, 88, 48-56.  
<https://doi.org/10.1016/j.ejca.2017.10.013>.
- [12] Vourtsis, A., & Berg, W. A. (2019). Breast density implications and supplemental screening. *European Radiology*, 29(4), 1762–1777. <https://doi.org/10.1007/s00330-018-5608-7>.
- [13] García-Mendoza, M. G., Inman, D. R., Ponik, S. M., Jeffery, J. J., Sheerar, D. S., Van Doorn, R. R., ... & Keely, P. J. (2016). Neutrophils drive accelerated tumor progression in the collagen-dense mammary tumor microenvironment. *Breast Cancer Research*, 18(1), 49. <https://doi.org/10.1186/s13058-016-0713-1>.

- [14] Paszek, M. J., Zahir, N., Johnson, K. R., Lakins, J. N., Rozenberg, G. I., Gefen, A., ... & Weaver, V. M. (2006). Force from the extracellular matrix regulates cell signaling and oncogenesis. *Nature Cell Biology*, 8(11), 1160-1167. <https://doi.org/10.1038/ncb1497>.
- [15] Butcher, D. T., Alliston, T., & Weaver, V. M. (2019). A tense situation: Mechanical forces in cancer development. *Nature Reviews Cancer*, 19(2), 88-102. <https://doi.org/10.1038/s41568-018-0087-4>.
- [16] Feng, Y., Spezia, M., Huang, S., Yuan, C., Zeng, Z., Zhang, L., Ji, X., Liu, W., Huang, B., Luo, W., Liu, B., Lei, Y., Du, S., Vuppalapati, A., Luu, H. H., Haydon, R. C., He, T.-C., & Ren, G. (2018). Breast cancer development and progression: Risk factors, cancer stem cells, signaling pathways, genomics, and molecular pathogenesis. *Genes & Diseases*, 5(2), 77-106. <https://doi.org/10.1016/j.gendis.2018.05.001>.
- [17] Pratt, S. J. P., Lee, R. M., & Martin, S. S. (2020). The mechanical microenvironment in breast cancer. *Cancers*, 12(6), 1452. <https://doi.org/10.3390/cancers12061452>.
- [18] Ann F. Reilley, *Breast Asymmetry: Classification and Management*, *Aesthetic Surgery Journal*, Volume 26, Issue 5, September 2006, Pages 596–600, <https://doi.org/10.1016/j.asj.2006.07.006>.
- [19] Scutt, D., Manning, J. T., Whitehouse, G. H., Leinster, S. J., & Massey, C. P. (1997). The relationship between breast asymmetry, breast size and the occurrence of breast cancer. *The British Journal of Radiology*, 70(838), 1017-1021.
- [20] Morrison, S., Kimble, J. Asymmetric and symmetric stem-cell divisions in development and cancer. *Nature* 441, 1068–1074 (2006). <https://doi.org/10.1038/nature04956>.
- [21] Nguyen, T. N., Ho Ba Tho, M. C., & Dao, T. T. (2020). A Systematic Review of Real-Time Medical Simulations with Soft-Tissue Deformation: Computational Approaches, Interaction Devices, System Architectures, and Clinical Validations. *Applied bionics and biomechanics*, 2020, 5039329. <https://doi.org/10.1155/2020/5039329>.

- [22] Hall, M. S., Alisafaei, F., Ban, E., Feng, X., Hui, C. Y., Shenoy, V. B., & Wu, M. (2016). Fibrous nonlinear elasticity enables positive mechanical feedback between cells and ECMs. *Proceedings of the National Academy of Sciences of the United States of America*, 113(49), 14043–14048. <https://doi.org/10.1073/pnas.1613058113>
- [23] Krouskop, T. A., Wheeler, T. M., Kallel, F., Garra, B. S., & Hall, T. (1998). Elastic moduli of breast and prostate tissues under compression. *Ultrasonic imaging*, 20(4), 260-274.
- [24] Ophir J, Cespedes I, Ponnekanti H, Yazdi Y, Li X (1991) Elastography: a quantitative method for imaging the elasticity of biological tissues. *Ultrason Imaging* 13:111–134. doi:10.1016/0161-7346(91)90079-W.
- [25] Sinkus R, Lorenzen J, Schrader D, Lorenzen M, Dargatz M, Holz D (2000) High-resolution tensor MR elastography for breast tumor detection. *Phys Med Biol* 45:1649–1664. doi:10.1088/0031-9155/45/6/317.
- [26] Srivastava A, Verma Y, Rao KD, Gupta PK (2011) Determination of elastic properties of resected human breast tissue samples using optical coherence tomographic elastography. *Strain* 47:75–87. doi:10.1111/j.1475-1305.2009.00627.x.
- [27] Tanner, C., Schnabel, J. A., Hill, D. L. G., Hawkes, D. J., Leach, M. O., & Hose, D. R. (2006). Factors influencing the accuracy of biomechanical breast models. *Medical Physics*, 33(6), 1758–1769. <https://doi.org/10.1118/1.2198315>.
- [28] Dempsey, S., & Samani, A. (2023). Mechanical properties of breast tissue. In *Biomechanics of the Female Reproductive System: Breast and Pelvic Organs* (pp. 169-207). Academic Press.
- [29] McGhee, D. E., & Steele, J. R. (2020). Breast biomechanics: what do we really know?. *Physiology*, 35(2), 144-156.
- [30] Halilaj, E., Rajagopal, A., Fiterau, M., Hicks, J. L., Hastie, T. J., & Delp, S. L. (2018). Machine learning in human movement biomechanics: Best practices, common pitfalls, and new opportunities. *Journal of biomechanics*, 81, 1-11.

- [31] White, J., & Scurr, J. (2012). Evaluation of professional bra fitting criteria for bra selection and fitting in the UK. *Ergonomics*, 55(6), 704-711.  
<https://doi.org/10.1080/00140139.2011.647096>.
- [32] McGhee, D. E., & Steele, J. R. (2010). Optimising breast support in female patients through correct bra fit. A cross-sectional study. *Journal of Science and Medicine in Sport*, 13(6), 568-572. <https://doi.org/10.1016/j.jsams.2010.03.003>.
- [33] Bengtson, B. P., & Glicksman, C. A. (2015). The standardization of bra cup measurements: redefining bra sizing language. *Clinics in plastic surgery*, 42(4), 405-411.
- [34] Sun, Y., Yick, K. L., Yu, W., Chen, L., Lau, N., Jiao, W., & Zhang, S. (2019). 3D bra and human interactive modeling using finite element method for bra design. *Computer-Aided Design*, 114, 13-27.
- [35] Haacke, E. M., Brown, R. W., Thompson, M. R., & Venkatesan, R. (1999). *Magnetic resonance imaging: Physical principles and sequence design*. Wiley-Liss.
- [36] Mansfield, P., & Morris, P. G. (1982). *NMR imaging in biomedicine*. *Advances in Physics*, 31(2), 209-279.
- [37] American Cancer Society. (2023, January 11). Breast MRI. Retrieved from <https://www.cancer.org/cancer/breast-cancer/screening-tests-and-early-detection/breast-mri-scans.html>.
- [38] National Institute of Biomedical Imaging and Bioengineering. (2023, February 14). Magnetic resonance imaging (MRI).
- [39] Kuhl, C. K., & Mielke, B. (2017). *Breast MRI: A comprehensive guide*. Springer.
- [40] Treloar, L. R. G. (1943). "The elasticity of a network of long-chain molecules—II". *Transactions of the Faraday Society*. 39: 241–246.
- [41] American College of Radiology. (2013). *Breast Imaging Reporting and Data System (BI-RADS®) atlas*, 4th ed. Reston, VA: American College of Radiology.

- [42] Drukker, K., Giger, M. L., & Horsch, K. (2014). Multi-modality computer-aided breast cancer diagnosis with FFDM and DCE-MRI. *Academic Radiology*, 21(9), 1215-1223.
- [43] Schaefer, G., Závisek, M., & Nakashima, T. (2018). Thermography based breast cancer analysis using statistical features and fuzzy classification. *Pattern Recognition*, 71, 106-117.
- [44] Lee, C. H., Dershaw, D. D., Kopans, D., Evans, P., Monsees, B., Monticciolo, D., ... & Bassett, L. (2010). Breast cancer screening with imaging: recommendations from the Society of Breast Imaging and the ACR on the use of mammography, breast MRI, breast ultrasound, and other technologies for the detection of clinically occult breast cancer. *Journal of the American College of Radiology*, 7(1), 18-27.
- [45] Qi, H., Diakides, N. A., & Zhou, Y. (2005). Infrared imaging in medicine. In *Sensor Technologies and Applications, 2008. SensorComm '08. Second International Conference on* (pp. 717-721). IEEE.
- [46] Karssemeijer, N., & te Brake, G. M. (1996). Detection of stellate distortions in mammograms. *IEEE Transactions on Medical Imaging*, 15(5), 611-619.
- [47] Oliver, A., Freixenet, J., Martí, J., Pérez, E., Pont, J., Denton, E. R. E., & Zwiggelaar, R. (2007). A novel breast tissue density classification methodology. *IEEE Transactions on Information Technology in Biomedicine*, 11(1), 55-62.
- [48] Suh YJ, Jung J, Cho B-J. Automated Breast Cancer Detection in Digital Mammograms of Various Densities via Deep Learning. *Journal of Personalized Medicine*. 2020; 10(4):211. <https://doi.org/10.3390/jpm10040211>
- [49] Ribli D., Horváth A., Unger Z., Pollner P., Csabai I. Detecting and classifying lesions in mammograms with Deep Learning. *Sci. Rep.* 2018;8:4165.
- [50] Kooi T., Litjens G., van Ginneken B., Gubern-Mérida A., Sánchez C.I., Mann R., den Heeten A., Karssemeijer N. Large scale deep learning for computer aided detection of mammographic lesions. *Med. Image Anal.* 2017;35:303–312.

- [51] Rodríguez-Ruiz A., Krupinski E., Mordang J.-J., Schilling K., Heywang-Köbrunner S.H., Sechopoulos I., Mann R.M. Detection of breast cancer with mammography: effect of an artificial intelligence support system. *Radiology*. 2019;290:305–314.
- [52] Al-Masni M.A., Al-Antari M.A., Park J.-M., Gi G., Kim T.-Y., Rivera P., Valarezo E., Choi M.-T., Han S.-M., Kim T.-S. Simultaneous detection and classification of breast masses in digital mammograms via a deep learning YOLO-based CAD system. *Comput. Methods Program. Biomed.* 2018;157:85–94.
- [53] Shen L., Margolies L.R., Rothstein J.H., Fluder E., McBride R., Sieh W. Deep learning to improve breast cancer detection on screening mammography. *Sci. Rep.* 2019;9:12495.
- [54] Yassin N.I.R., Omran S., El Houbay E.M.F., Allam H. Machine learning techniques for breast cancer computer aided diagnosis using different image modalities: a systematic review. *Comput. Methods Program. Biomed.* 2018;156:25–45.
- [55] Mallapragada, V., Sarkar, N., & Podder, T. K. (2007, October). A robotic system for real-time tumor manipulation during image guided breast biopsy. In 2007 IEEE 7th international symposium on bioinformatics and bioengineering (pp. 204-210). IEEE.
- [56] Lee, A. W., Rajagopal, V., Gamage, T. P. B., Doyle, A. J., Nielsen, P. M., & Nash, M. P. (2013). Breast lesion co-localisation between X-ray and MR images using finite element modelling. *Medical image analysis*, 17(8), 1256-1264.
- [57] Ruiter, N. V., Stotzka, R., Muller, T. O., Gemmeke, H., Reichenbach, J. R., & Kaiser, W. A. (2006). Model-based registration of X-ray mammograms and MR images of the female breast. *IEEE Transactions on Nuclear Science*, 53(1), 204-211.
- [58] Fovargue, D., Kozerke, S., Sinkus, R., & Nordsletten, D. (2018). Robust MR elastography stiffness quantification using a localized divergence free finite element reconstruction. *Medical image analysis*, 44, 126-142.

- [59] Lawrence, A. J., Muthupillai, R., Rossman, P. J., Smith, J. A., Manduca, A., and Ehman, R. L. (1998). Magnetic resonance elastography of the breast. *Investig. Radiol.* 40, 412–420. doi:10.1097/01.rli.0000166940.72971.4a
- [60] Xydeas, T., Siegmann, K., Sinkus, R., Krainick-Strobel, U., Miller, S., and Claussen, C. D. (2005). Magnetic resonance elastography of the breast: Correlation of signal intensity data with viscoelastic properties. *Investig. Radiol.* 40, 412–420. doi:10.1097/01.rli.0000166940.72971.4a
- [61] Chen, J., Brandt, K., Ghosh, K., Grimm, R., Glaser, K., Kugel, J., et al. (2013). Noncompressive MR elastography of breasts. *Proc. Intl. Soc. Mag. Reson. Med.* 21, 1736.
- [62] McKnight, A. L., Kugel, J. L., Rossman, P. J., Manduca, A., Hartmann, L. C., and Ehman, R. L. (2002). MR elastography of breast cancer: Preliminary results. *Am. J. Roentgenol.* 178, 1411–1417. doi:10.2214/ajr.178.6.1781411
- [63] Sayed, A., Layne, G., Abraham, J., and Mukdadi, O. (2013). Nonlinear characterization of breast cancer using multi-compression 3D ultrasound elastography in vivo. *Ultrasonics* 53, 979–991. doi:10.1016/j.ultras.2013.01.005
- [64] Han, L., Noble, J. A., and Burcher, M. (2003). A novel ultrasound indentation system for measuring biomechanical properties of in vivo soft tissue. *Ultrasound Med. Biol.* 29, 813–823. doi:10.1016/S0301-5629(02)00776-7
- [65] Barr, R. G., and Zhang, Z. (2012). Effects of precompression on elasticity imaging of the breast: Development of a clinically useful semiquantitative method of precompression assessment. *J. Ultrasound Med.* 31, 895–902. doi:10.7863/jum.2012.31.6.895
- [66] Griffin, M., Premakumar, Y., Seifalian, A., Butler, P. E., and Szarko, M. (2016). Biomechanical characterization of human soft tissues using indentation and tensile testing. *J. Vis. Exp.* 1, 54872. doi:10.3791/54872
- [67] Delaine-Smith, R. M., Burney, S., Balkwill, F. R., and Knight, M. M. (2016). Experimental validation of a flat punch indentation methodology calibrated against

unconfined compression tests for determination of soft tissue biomechanics. *J. Mech. Behav. Biomed. Mater.* 60, 401–415. doi:10.1016/j.jmbbm.2016.02.019

[68] Wellman, P. S., Howe, R. D., Dalton, E., and Kern, K. A. (1999). Breast tissue stiffness in compression is correlated to histological diagnosis. Technical Report. Cambridge, MA: Harvard BioRobotics Laboratory, 1–15.

[69] Samani, A., Bishop, J., Luginbuhl, C., and Plewes, D. (2003). Measuring the elastic modulus of ex vivo small tissue samples. *Phys. Med. Biol.* 48, 2183–2198. doi:10.1088/0031-9155/48/14/310

[70] Sarvazyan, A. P., Skovoroda, A. R., Emelianov, S. Y., Fowlkes, J. B., Pipe, J. G., Adler, R. S., et al. (1995). Biophysical bases of elasticity imaging. Boston, MA: Springer US, 223–240. doi:10.1007/978-1-4615-1943-0\_23

[71] Krouskop, T. A., Wheeler, T. M., Kallel, F., Garra, B. S., and Hall, T. (1998). Elastic moduli of breast and prostate tissues under compression. *Ultrason. Imaging* 20, 260–274. doi:10.1177/016173469802000403.

[72] Matsumura, T., Umemoto, T., Fujihara, Y., Ueno, E., Yamakawa, M., Shiina, T., et al. (2009). Measurement of elastic property of breast tissue for elasticity imaging.

*Proc. - IEEE Ultrason. Symp.*, 1451–1454doi. doi:10.1109/ULTSYM.2009.5442044

[73] Umemoto, T., Ueno, E., Matsumura, T., Yamakawa, M., Bando, H., Mitake, T., et al. (2014). Ex vivo and in vivo assessment of the non-linearity of elasticity properties of breast tissues for quantitative strain elastography. *Ultrasound Med. Biol.* 40, 1755–1768. doi:10.1016/j.ultrasmedbio.2014.02.005

[74] Calvo-Gallego, J. L., Domínguez, J., Gómez Cí a, T., Ruiz-Moya, A., Gómez Ciriza, G., and Martí nez-Reina, J. (2020). Comparison of the viscoelastic properties of human abdominal and breast adipose tissue and its incidence on breast reconstruction surgery. A pilot study. *Clin. Biomech.* 71, 37–44. doi:10.1016/j.clinbiomech.2019.10.009

- [75] Samani, A., and Plewes, D. (2004). A method to measure the hyperelastic parameters of ex vivo breast tissue samples. *Phys. Med. Biol.* 49, 4395–4405. doi:10.1088/0031-9155/49/18/014
- [76] Dempsey, S. C., O’Hagan, J. J., and Samani, A. (2021). Measurement of the hyperelastic properties of 72 normal homogeneous and heterogeneous ex vivo breast tissue samples. *J. Mech. Behav. Biomed. Mater.* 124, 104794. doi:10.1016/j.jmbbm.2021.104794
- [77] Sun, Z., Gepner, B. D., Lee, S. H., Rigby, J., Cottler, P. S., Hallman, J. J., et al. (2021). Multidirectional mechanical properties and constitutive modeling of human adipose tissue under dynamic loading. *Acta Biomater.* 129, 188–198. doi:10.1016/j.actbio.2021.05.021
- [78] Sun, Z., Lee, S. H., Gepner, B. D., Rigby, J., Hallman, J. J., and Kerrigan, J. R. (2021). Comparison of porcine and human adipose tissue loading responses under dynamic compression and shear: A pilot study. *J. Mech. Behav. Biomed. Mater.* 113, 104112–112. doi:10.1016/j.jmbbm.2020.104112
- [79] Tanner, C., Degenhard, A., Schnabel, J. A., Smith, A. C., Hayes, C., Sonoda, L. I., & Hawkes, D. J. (2001, December). A method for the comparison of biomechanical breast models. In *Proceedings IEEE Workshop on Mathematical Methods in Biomedical Image Analysis (MMBIA 2001)* (pp. 11-18). IEEE.
- [80] Reishner R, Balogh B, Menzel E. Two dimensional elastic properties of human skin in terms of an incremental model at the in vivo configuration. *Med Eng Phys* 1995;17(4):304-13.
- [81] Tanner C, Schanabel JA, Hill DLG, Hawkes DJ. Factors influencing the accuracy of biomechanical breast models. *Med Phys* 2006;33(6):1758-69.
- [82] Yeoh, O. H.(1993). Some forms of the strain energy function for rubber. *Rubber Chemistry and technology*, Volume 66, Issue 5, 754-771.

- [83] Ogden, R. W. (1972). Large Deformation Isotropic Elasticity – On the Correlation of Theory and Experiment for Incompressible Rubberlike Solids, *Proceedings of the Royal Society of London. Series A, Mathematical and Physical Sciences*, Vol. 326, No. 1567, pp. 565–584.
- [84] D.R. Veronda, R.A. Westmann. Mechanical Characterization of Skin - Finite Deformations. *J. Biomechanics*, Vol. 3:111-124, 1970.
- [85] Ingber, D. E. (2006). Cellular mechanotransduction: putting all the pieces together again. *Faseb Journal*, 20(7), 811-827.
- [86] Paszek, M. J., Zahir, N., Johnson, K. R., Lakins, J. N., Rozenberg, G. I., Gefen, A., ... & Weaver, V. M. (2005). Tensional homeostasis and the malignant phenotype. *Cancer Cell*, 8(3), 241-254.
- [87] Coussens, L. M., & Werb, Z. (2002). Inflammation and cancer. *Nature*, 420(6917), 860-867.
- [88] Plodinec, M., Loparic, M., Monnier, C. A., Obermann, E. C., Zanetti-Dallenbach, R., Oertle, P., ... & Aebi, U. (2012). The nanomechanical signature of breast cancer. *Nature Nanotechnology*, 7(11), 757-765.
- [89] Butcher, D. T., Alliston, T., & Weaver, V. M. (2009). A tense situation: forcing tumour progression. *Nature Reviews Cancer*, 9(2), 108-122.
- [90] Bingham, G., Bentham, M., & Bruner, D. (2005). Garment-Model Computer Simulations. U.S. Patent Application No. 11/152,900.
- [91] Bel-Brunon, A., Bouten, L., Cornolo, J., & Morestin, F. (2014). Numerical modeling of bra wear during running. In 11th World Congress on Computational Mechanics (WCCM XI), Barcelona, Spain.
- [92] Sun, Y., Yick, K. L., Cai, Y., Yu, W., Chen, L., Lau, N., & Zhang, S. (2021). Finite element analysis on contact pressure and 3D breast deformation for application in women's bras. *Fibers and Polymers*, 22(10), 2910-2921.

- [93] Zhang, S., Yick, K. L., Yip, J., Yu, W., & Tang, K. P. M. (2021). An understanding of bra design features to improve bra fit and design for older Chinese women. *Textile Research Journal*, 91(3-4), 406-420.
- [94] Spencer, L., & Briffa, K. (2013). Breast size, thoracic kyphosis & thoracic spine pain-association & relevance of bra fitting in post-menopausal women: a correlational study. *Chiropractic & manual therapies*, 21, 1-8.
- [95] Findikcioglu, K., Findikcioglu, F., Ozmen, S., & Guclu, T. (2007). The impact of breast size on the vertebral column: a radiologic study. *Aesthetic plastic surgery*, 31, 23-27.
- [96] Sun, Y. (2019). Finite element model for predicting the pressure comfort and shaping effect of wired bras.
- [97] Zheng, R., Yu, W., & Fan, J. (2009). Pressure evaluation of 3D seamless knitted bras and conventional wired bras. *Fibers and Polymers*, 10, 124-131.
- [98] Lu, M., Qiu, J., Wang, G., & Dai, X. (2016). Mechanical analysis of breast–bra interaction for sports bra design. *Materials Today Communications*, 6, 28-36.
- [99] Liang, R., Yip, J., Yu, W., Chen, L., & Lau, N. M. (2019). *Mater. Des.*, 183, Article 108177.
- [100] Zhang, X., Yeung, K., & Li, Y. (2002). *Textile Research Journal*, 72, 245–250.
- [101] Wang, R., Liu, Y., Luo, X., Li, Y., & Ji, S. (2011). *Journal of Computational and Applied Mathematics*, 236, 867–879.
- [102] Dan, R., Fan, X. R., Chen, D. S., & Wang, Q. (2011). *Textile Research Journal*, 81, 128-136.
- [103] Franciosa, P., Gerbino, S., Lanzotti, A., & Silvestri, L. (2013). *Medical Engineering & Physics*, 35, 36-42.

[104] Zhang, M., Dai, X. Q., Li, Y., & Cheung, J. T. M. (2007). Studies in Computational Intelligence, 55, 323-330.

## Chapter 2

### 2 « Prediction Risk of Breast Cancer Development Using Breast Bilateral Asymmetry Analysis within a Machine Learning Framework »

#### 2.1 « Introduction »

Breast cancer surpassed lung cancer in 2020 to become the leading cause of death among women globally [1]. Early detection of breast cancer, paired with personalized treatment strategies, has significantly reduced mortality and morbidity rates [2]. Tissue assessment aiming at identifying abnormalities through medical imaging of the breast is a potent method for early diagnosis. However, many young women at risk, particularly those without a family history of BRCA1 and BRCA2 mutations, lack access to regular screening programs like The Ontario Breast Screening Program (OBSP) [3].

Implementing a population-wide risk assessment protocol for breast cancer to identify women with high-risk breast abnormalities before enrolling them in effective screening programs could markedly improve survival rates.

Bilateral asymmetry, characterized by uneven size, shape, volume, and tissue distribution in the breasts, has recently been recognized as a strong indicator of cancer risk [4]. This asymmetry can be classified into four categories: natural asymmetry, global asymmetry, focal asymmetry, and developing asymmetry [5]. While natural asymmetry is often mistaken for cancerous asymmetry, developing asymmetry is a genuine cause for concern. Despite numerous studies highlighting the strong correlation between asymmetry and cancer risk [6-9], many focus on scenarios after breast cancer diagnosis or fail to exclude false positives due to natural asymmetry. This underscores the need for computer assisted methods that can accurately classify bilateral asymmetries associated with high cancer risk.

Magnetic Resonance Imaging (MRI), a key modality in breast cancer diagnosis, provides valuable information about breast anatomical structures. However, the complex differences in fibroglandular tissue distribution among individuals often complicate the interpretation of screening mammograms due to overlapping dense fibroglandular tissues (FGTs), leading to low true negative rates [10]. With the advent of machine learning, many methods have started to treat medical images (e.g, MRI or X-ray mammograms) as sets of pathology manifestation features and apply feature engineering to such images to assist with cancer assessment. For example, Yan et al. (2017) improved the accuracy of short-term breast cancer risk prediction by applying a new mammographic image conversion method combined with a two-stage artificial neural network (ANN)-based classification scheme [11]. Following a similar goal, Chaurasia (2018) developed prediction models for breast cancer survivability using data mining techniques. The research focused on utilizing machine learning algorithms to analyze medical imaging data, such as MRI or X-ray mammograms, to predict the likelihood of a patient surviving after a breast cancer diagnosis. This approach allows for more personalized and effective treatment plans, ultimately improving patient outcomes [12]. Li (2018) aimed at developing a new short-term breast cancer risk prediction model that applies a machine learning approach to image data. This machine learning approach encompasses a locally preserving projection (LPP)-based feature combination and regeneration algorithm [13]. However, these studies focus on short-term (0.5-1.5 years) cancer predictions where tissue abnormalities are already evident, and the training data is typically labeled by experienced physicians.

Among breast imaging modalities, MRI mammography is highly advantageous in clear presentation of spatial distribution of breast tissue features that may carry information about current pathology development and its future manifestation. Searching the topic of MRI breast cancer assessment based on asymmetry analysis indicates that only a few investigations have been conducted to develop effective pertinent algorithms. This highlights a substantial need for an accurate automatic classifier for image-based breast cancer risk assessment. In this study, we develop a ML-based classifier that estimates the

risk of breast cancer accurately according to bilateral MRI images. Our objective in this work is to investigate the feasibility of predicting the risk of developing breast cancer based on quantitative assessment of the breasts' asymmetry in MRI mammograms via a ML algorithm. This investigation involves a longitudinal study to provide long-term cancer risk prediction. Data pertaining to the study is used to train the algorithm which is founded on automatic clustering framework.

## 2.2 « Materials and Methods »

### 2.2.1 Overview of Proposed Model

In this study, we propose an end-to-end framework for assessing a woman's risk of developing breast cancer by analyzing her bilateral breast MRI images. The method is essentially based on unsupervised learning and data clustering, and it includes four main steps as shown in the block diagram of Figure 2-1. The steps are MRI mammogram preprocessing, data augmentation, feature engineering, and finally clustering and risk estimation using cross-fold validation.

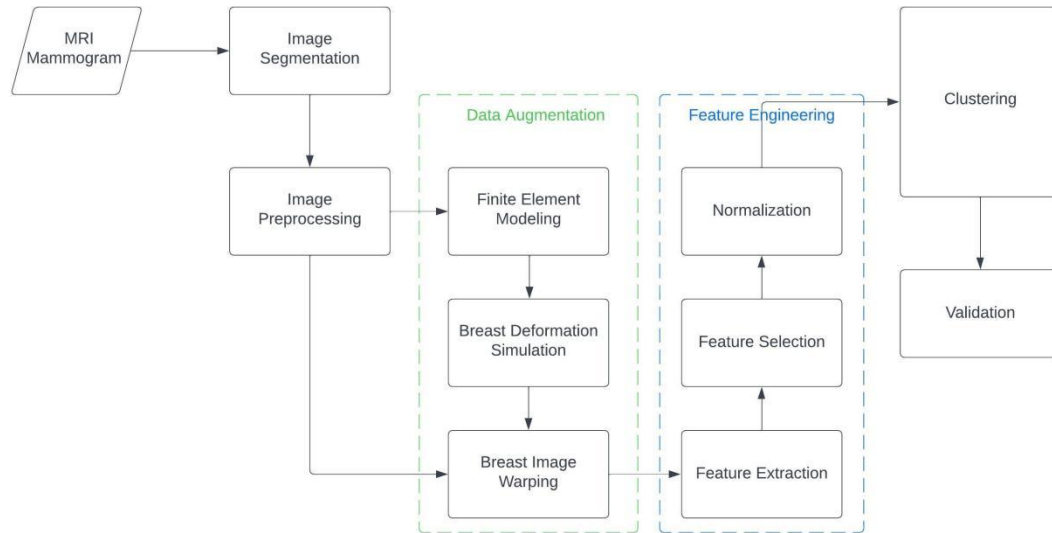


**Figure 2-1: Block diagram of the clustering method proposed for breast cancer risk assessment.**

### 2.2.2 Data acquisition

In this study, a breast MRI scan dataset consisting of 55 patients with notable bilateral asymmetry who participated in a longitudinal study was used. This study was conducted with the approval of the ethics committee of The Second Affiliated Hospital, School of Medicine, Zhejiang University. The inclusion criteria was women who had two sequential bilateral breast MR scans previously acquired at the same center while the first scans were all negative for breast cancer. The second scan was acquired between 6 to 36 months after the first scan was acquired. The dataset comprised MRI images acquired using a 1.5T Siemens scanner equipped with a bilateral phased array breast coil. The imaging protocol employed T1-weighted pulse sequences, designed to emphasize the contrast differences between fatty and fibroglandular breast tissues. The specific sequence with an in-plane resolution of 256 x 256. The number of slices varied from 15 to 23, accommodating different breast sizes and shapes. The utilized parameters are a repetition time of 7.5 ms, a echo time of 4.2 ms, and a flip angle of 10 degrees to optimize the visualization of breast tissues. The MRI protocol also included fat

suppression techniques to further enhance the contrast between different tissue types and to aid in the clear delineation of potential lesions. An example of an MRI scan pertaining to a breast cancer case is shown in Figure 2-2. In the next sequential screening examination, 50 of the 55 patients were diagnosed with different types of breast cancer.

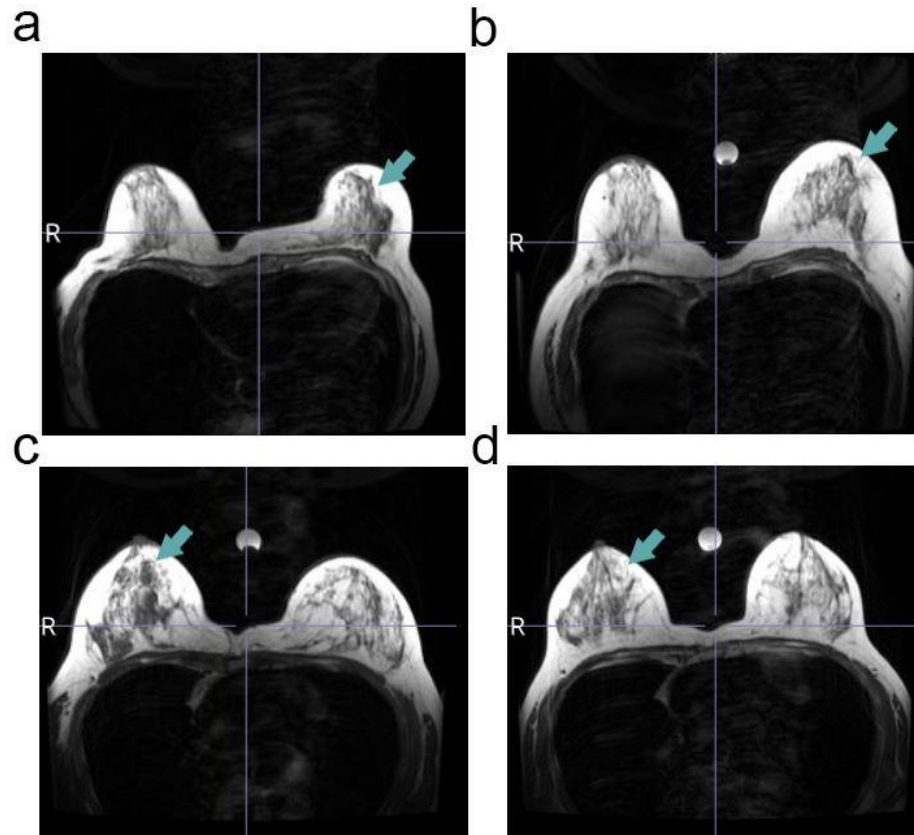


**Figure 2-2: Breast bilateral MRI images of two patients included in the study. (a) depicts the first scan of a patient's breast, where the arrow highlights a region of dense tissue initially not diagnosed as cancerous by the radiologist. (b) shows a subsequent scan of the same patient, where the previously dense tissue area has since developed into a cancerous tumor, as confirmed by biopsy. This is a good example of a patient's breasts with substantial bilateral asymmetry that is clearly visible in the image. (c) presents the first scan of a breast that was correctly identified as non-cancerous. Due to the rich blood supply in the nipple-areolar**

**complex, this tissue was misinterpreted as a cancerous mass. In (d), the second scan of the patient shows that the tissue at this location is non-cancerous, similar to the tissue on the right side. This type of misdiagnosis often occurs in large-sized breasts. Compared to the former patient, the breasts of the latter patient has less obvious bilateral asymmetry.**

### 2.2.3 Data Augmentation Using Finite Element (FE) Based Image Warping

As indicated earlier, for developing a model for identifying the group of women who are at high risk of developing breast cancer, we use breast MRI images of a cohort of 55 women who had two scans acquired sequentially within 6 to 36 months. This data is both limited in size and imbalanced as only 5 women were breast cancer free according to the second scan. To address these issues, we used a physics-based data augmentation technique that produces highly realistic new breast MRI images using existing scans of the dataset. Commonly used data augmentation techniques rely on geometric transformations such as scaling, rotation, or translation. These techniques are insufficient in the problem being tackled in this research as they are only intended to enhance the ability of the classification model to learn general features existing in the available data. In contrast, the method proposed in this work employs highly accurate FE modeling of the breast to generate new image data. The core of the proposed FE warping workflow involves a deformed image generation method based on a model-to-image technique. It follows an image warping framework which uses a reference image along with realistic tissue mechanical properties and loading to obtain a non-linear transformation founded on the breast biomechanics to be combined with the reference image to produce a new realistic image. The overall framework of image warping is illustrated in Figure 2-3. To our knowledge, our group is the first to utilize this approach for breast MRI data augmentation. Details of the augmentation methods are provided below.

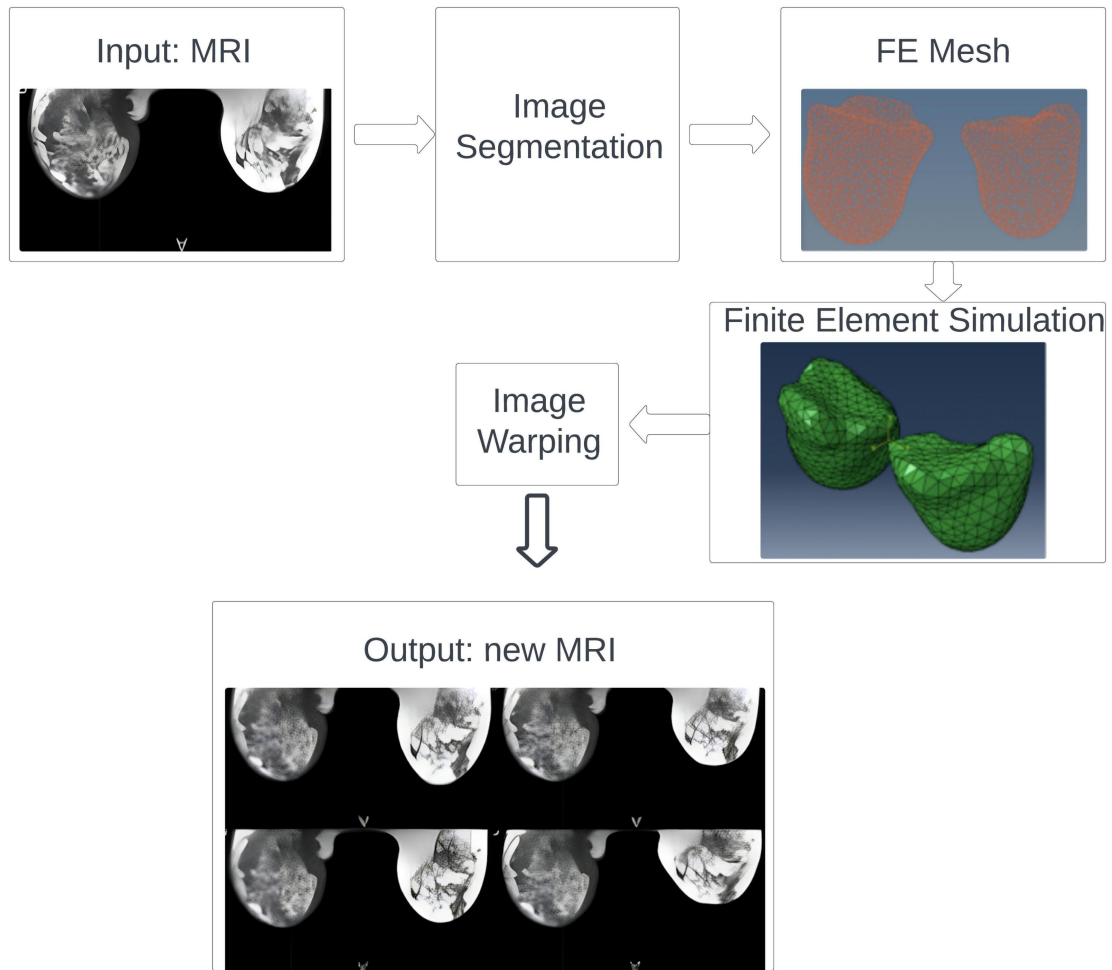


**Figure 2-3: Block diagram of the proposed warping framework.**

### 2.2.3.1 Segmentation

To build the 3D FE model, each breast was segmented separately from its MR image slice by slice using 3D Slicer ([www.slicer.org](http://www.slicer.org)). The segmentation followed a region growing-based technique before opening and closing operations employed for smoothing. Since most of the breast tissue is concentrated in the anterior part of the breast, the thoracic cavity was not included in the image segmentation. Before segmentation, some of the MRI scans were enhanced by a Gaussian filter and normalized through histogram normalization.

### **2.2.3.2 FE Meshing**

Using Altair HyperMesh ([www.altair.com](http://www.altair.com)), a 3D FE mesh was created for each breast volume obtained from segmentation using 10-noded second-order tetrahedral elements. These elements are known to follow the geometry of the object being modelled closely while providing good analysis accuracy. Typically, each breast was discretized into more than 2000 tetrahedral elements. Mesh convergence analysis was performed on 5 typical breast models selected from the dataset to ensure that the selected mesh size was appropriate.

### **2.2.3.3 Loading and Tissue Mechanical Properties**

The FE breast model employed in the data augmentation generates realistic tissue deformation based on the model's nodal displacement field pertaining to alteration in the gravity loading orientation resulting from changes in the body position (e.g., rotation) anticipated during MRI scanning. In this study, we considered a rotation variation of  $\pm 5^\circ$  around the superior-inferior axis with respect to the reference image. To generate multiple cases, we considered a rotation angle increment of  $1\sim 3^\circ$ . The loading consisted of two steps where the first was considered to obtain the breast's unloaded geometry obtained by applying negative gravity loading. The second step was performed by applying gravity loading with respect to the rotated configuration. The latter step is intended to alter the breast's shape and its tissue distribution in a realistic way. These alterations are expected to lead to new and yet realistic breast image features. As the breast is known to undergo large deformation under loading, the FE model adapted in this study considers the breast tissue as a hyperelastic material with parameters obtained in our lab [14]. For further increasing the size of the augmented data, we took advantage of the known inter-patient variation of tissue stiffness characteristics. As such, we utilized hyperelastic parameter values within the parameters range reported in [15].

The FE simulation under loading alteration pertaining to body rotation was performed using Abaqus solver (SIMULIA, Providence, RI, USA). Along with each original undeformed MR image, the displacement field was used to generate a new image pertaining to its deformed state. The combination of various body rotations and hyperelastic parameters led to the generation of additional 50 and 109 healthy and cancer cases, respectively.

#### **2.2.3.4 Augmentation Convergence**

To ascertain that enough cases were generated for data augmentation, we added 10% more data to the baseline augmentation data before comparing the model performance developed with the complemented and baseline augmented datasets. This 10% data addition was made to each type of the baseline augmented data, including rotation and assigning different hyperelastic parameters. We then applied feature engineering analysis to the two complemented and baseline augmented datasets and compared their feature distribution to determine whether the additional 10% data augmentation had substantial effect on the clustering results [16][17].

#### **2.2.4 Feature Engineering**

Feature engineering is a crucial step in enhancing the performance of a machine learning model. The aim of feature selection is to identify a subset of the most pertinent features from the original feature space, evaluate the relationships between various input features, remove noise, and reduce dimensionality to improve the model's interpretability by solely using the most informative features. The primary contribution of feature engineering lies in preventing overfitting and enhancing the model's generalization performance. In the proposed ML model, we extracted several image features before selecting the most effective ones for clustering.

### 2.2.4.1 Feature Extraction

In this work, we extracted asymmetry features, statistical features, shape-based features and high-order features. Because the breast is made up of lobules, ducts, adipose and fibroglandular tissues in addition to fibrous connective tissue, the texture of tissue was also considered as a likely effective feature in the breast MR image [18]. In the proposed method, texture and density features were extracted using non-orthogonal Gabor wavelets [19]. First, the MRI scans were enhanced by a Gaussian filter and normalized by histogram normalization so that small differences in features relevant to tissue abnormality can be detected. To compute the predominant features related to bilateral tissue asymmetry, the Python toolbox PyRadiomics was used [20]. This package allows extracting 19 first-order statistical features in addition to 16 shape-based features. To account for the breast's natural asymmetries with no contribution to positive cancer findings, high-order features were added, resulting in a complex-valued feature vector to elucidate subtle developing asymmetry. Specifically, 75 other high-order features were considered, including 24 features derived from the gray-level co-occurrence matrix (GLCM), 16 from the gray-level run-length matrix (GLRLM), 16 from the gray-level size zone matrix (GLSZM), 5 from the neighborhood gray-tone difference matrix (NGTDM), and 14 from the gray-level dependence matrix (GLDM). Description of the extracted features is summarized in Table 2-1.

**Table 2-1: Features related to breast tissue density and texture with their description.**

Feature Type	Feature Number	Description
First-Order Statistics	19	Quantifies voxel intensity distribution in the image region.
Shape-Based	16	Measures the 3D size descriptors.

Features		
GLCM	24	Details the second-order joint probability function via Gray Level Co-occurrence Matrix.
GLRLM	16	Quantifies gray level runs, or consecutive pixels of identical gray level value, using Gray Level Run Length Matrix.
GLSZM	16	Utilizes Gray Level Size Zone Matrix to measure gray level zones or connected voxels of identical gray level intensity.
NGTDM	5	Uses Neighbouring Gray Tone Difference Matrix to determine the difference between a gray value and its neighbours' average gray value within a specific distance.
GLDM	14	Implements Gray Level Dependence Matrix to calculate gray level dependencies, or the count of connected voxels within a specific distance that depends on the central voxel.

For the asymmetry feature, we separately delineated two breast volumes from MRI images of the left and right breasts. Prior to comparing these volumes, a critical step of deformable image registration was employed to ensure precise alignment of the left and right breasts. These volumetric data were then used to represent the “bilateral asymmetry” features in feature space. Normalized Mutual Information (NMI) is a measure derived from the field of information theory and is used to assess the similarity between two sets of data. It is particularly useful in medical imaging for comparing and evaluating the

alignment of images from different modalities or taken at different times. The NMI can be mathematically represented as follows:

$$\mathbf{NMI}(L, R) = \frac{2 \times I(L;R)}{[H(L) + H(R)]} \quad (2-1)$$

$I(L,R)$  is the mutual information between the two left and right breast images  $L$  and  $R$ , which measures the amount of information in one image through the other.  $H(L)$  and  $H(R)$  are the entropy of the left and right images  $L$  and  $R$ , respectively, each representing the amount of information in the respective image. The normalization factor:  $2/[H(L) + H(R)]$  adjusts the mutual information function such that a substantial part of each image overlap, leading to reliable similarity measure. In essence, NMI evaluates how well one can predict the content of one image by knowing the content of the other image, with values closer to 1 indicating higher similarity or better alignment. A higher NMI value signifies a lower degree of bilateral asymmetry, indicating a greater similarity between the left and right breasts. In this work, negative samples, indicative of natural bilateral symmetry and devoid of cancerous implications, were methodically segregated to establish a normative baseline of asymmetry. The rationale behind this baseline is to refine the normalization process for the asymmetry feature. Consequently, this ensures a uniform distribution of NMI values across the feature space, preventing skewness towards any specific data region. This methodological approach underscores the importance of distinguishing between physiological asymmetry and aberrations suggestive of malignancy.

Beyond volume-level asymmetry features, we also extended asymmetry analysis to slice-level in MRI images. Given the layered acquisition of MRI scans, where a volume comprises a sequence of slices, the analysis at the slice level offers a finer granularity of asymmetry assessment. Following bilateral breast contours' deformable registration to align corresponding slices, we employed Pearson Correlation Coefficients (PCC) to quantify the asymmetry between left and right breast slices. The PCC is defined by the following:

$$\mathbf{PCC}(L, R) = \frac{\sum (l_i - \bar{l})(r_i - \bar{r})}{\sqrt{\sum (l_i - \bar{l})^2 \sum (r_i - \bar{r})^2}} \quad (2-2)$$

where  $L$  and  $R$  are the two slice images being compared,  $l_i$  and  $r_i$  are the pixel image intensity, and  $\bar{l}$  and  $\bar{r}$  are the mean image intensity values of  $L$  and  $R$ , respectively. Values close to 1 indicate a strong positive correlation, whereas values near -1 suggest a strong negative correlation (asymmetry). In our context, a diminished PCC underscores pronounced asymmetry between the corresponding breast slices, characterizing each breast volume pair by an array of 15-23 PCCs, corresponding to its slice count. This nuanced approach enhances the detection of asymmetrical features, pivotal for early cancer identification.

#### 2.2.4.2 Feature Selection

To avoid potential redundancy in extracted features and complicate model interpretability, it is essential to decrease the feature space's dimension through identifying the most important features. To combat overfitting during training, we assessed various feature selection techniques, such as wrapper, embedded, and filter methods [21]. Our streamlined feature selection process consists of the following steps:

1. Removal of collinear features.
2. Selection of pertinent variables from the initial extracted features. The process involved selecting relevant variables by employing Normalized Mutual Information (NMI) from the feature selection module of the sklearn library [22] and the Minimum Redundancy Maximum Relevance (mRMR) method via the pymrmr library [23]. These techniques were instrumental in identifying features that significantly represent bilateral asymmetry, which were then incorporated into the classification model. The mRMR method aims to select features that are highly relevant to the target variable while also being minimally redundant with each other. The core idea revolves around maximizing the relevance of selected features for the prediction task while minimizing their redundancy. Feature selection is highly effective to avert overfitting and ensure

sensitivity to initialization. The selection criterion emphasizes intra-group rankings to ensure a holistic representation of data aspects, effectively preventing the dominance of any single feature group in the selection process. For instance, within the "First-Order Statistics" group, which comprises 19 extracted features, the approach ensures that the top-performing features from this group are considered for inclusion. After selection, the features were normalized to adjust the scales of different variables, mitigating the risk larger-scale features dominating the model's attention and potentially skewing the results.

## 2.2.5 Clustering

To fully utilize the features extracted from MRI images, we applied two methods for classification.

### 2.2.5.1 Volume-by-Volume Clustering

Based on feature engineering, each medical image sample was represented as an  $n$ -dimensional array where  $n$  is the number of features obtained using feature engineering analysis following the concept of maximizing the amount of information provided by features. Next, we grouped these samples using the unsupervised K-means clustering method. The aim of the clustering here is to categorize breast asymmetry into different classes based on their mammographic features extracted from bilateral MRI images to compute a cancer risk or probability level for each case. The K-means clustering method was selected because, compared to other unsupervised clustering algorithms such as Mixture of Gaussians probabilistic clustering, it guarantees convergence, easily adapts to new samples while it warm-starts the position of centroids [24]. To improve the sensitivity of our auto-clustering model, we did not pre-label the negative/positive samples and retained the known binary labels only for use in validating the proposed method.

To determine the optimal number of clusters, we started with  $K=10$  classification clusters as a starting point, since for practical applications, 10 asymmetry clusters are sufficient to describe the commonalities of abnormal tissue [25]. We then applied the Elbow Criterion to find the optimal number of clusters and subsequently verified this determination using the Silhouette Score. Both criteria evaluate the cost function resulting from different cluster counts ( $K$ ). The Elbow Criterion involves plotting the sum of squared distances of samples to their closest cluster center, represented as:

$$J(K) = \sum_{i=1}^n (\|x_i - \mu_{c_i}\|^2) \quad (2-4)$$

$J(K)$  is the cost function for  $K$  clusters,  $x_i$  is a data point, and  $\mu_{c_i}$  is the centroid of the cluster assigned to  $x_i$ . For each  $K$ , the sum of squared errors (SSE) within-cluster is calculated. Plotting  $K$  against SSE typically reveals a point where the SSE decreases sharply before it levels off. This "elbow" in the curve visually represents the optimal cluster count as adding more clusters beyond this point offers minimal improvement in fitting the data. Conversely, the Silhouette Score is calculated using the mean intra-cluster distance  $a$  and the mean nearest-cluster distance  $b$  for each sample. The Silhouette Score for a single sample is:

$$\mathbf{S} = \frac{a - b}{\max(a, b)} \quad (2-5)$$

The overall Silhouette Score is the mean of all samples' Silhouette scores, providing a perspective on the cohesion and separation of the formed clusters. In practice, the Elbow Criterion often provides an initial cluster count estimate, while the Silhouette Score acts as a validation tool for refinement.

After determining the importance of each class of features during clustering, the LASSO (Least Absolute Shrinkage and Selection Operator) method is used to further refine the feature space [25]. Rather than simply eliminating features, LASSO allows for the selection of the most impactful attributes from each group during each clustering iteration. This is achieved through its approach of minimizing the sum of squared errors (SSE) while simultaneously penalizing the absolute size of regression coefficients. This

technique enhances accuracy and reduces model complexity. This is mathematically represented by Equation 2-6:

$$\beta^{lasso} = \underset{\beta}{\operatorname{argmin}} \sum_{i=1}^N (y_i - \beta_0 - \sum_{j=1}^p x_{ij} \beta_j)^2$$

$$\text{subject to: } \sum_{j=1}^p |\beta_j| \leq t \quad (2-6)$$

In this equation,  $x$  represents a set of input feature measurements, and  $y$  is the outcome we're trying to predict. The LASSO method fits a linear model to this data. Here,  $\beta$  is the vector of regression coefficients, and  $N$  is the number of observations or cases in the dataset. By adjusting the tuning parameter, the LASSO method effectively reduces the coefficients of less important features to zero dynamically, thereby selecting a more compact and accurate set of features during this iteration of clustering. This makes the LASSO method a valuable tool combining feature selection in high-dimensional datasets classification process.

### 2.2.5.1 Slice-by-Slice Clustering

In our slice-based classification model, we integrated K-means clustering with a specialized technique called contrastive loss to improve unsupervised classification accuracy [26]. The contrastive loss technique is a fine-tuning tool within the learning process; it encourages the model to group similar slices (asymmetry-wise) closer together, while pushing dissimilar ones further apart. Ultimately, this makes the system better at discerning subtle patterns indicative of breast asymmetry. The following pseudo-code illustrates the details for the contrastive loss K-means used in slice-by-slice module.

---

Algorithm: Contrastive Loss-Augmented K-means Clustering

---

- 1: Initialize cluster centroids using standard K-means clustering on the dataset.
  - 2: Set hyperparameters *sigma* ( $\sigma$ ) and *alpha* ( $\alpha$ ).
-

---

3: Repeat until convergence or maximum number of iterations is reached:

- a. Compute pairwise distances between all data points and centroids.
- b. Calculate similarity matrix  $\mathcal{S}$ , with  $\mathcal{S}_{ij} = \exp(-distance_{ij}^2 / (2 * \sigma^2))$ .
- c. Calculate contrastive loss  $L_{contrastive}$  for each point:
 
$$L_{contrastive}^i = -\log(\exp(-\mathcal{S}_{ii} / distance_i) / \sum(\exp(-\mathcal{S}_i / distance_i))).$$
- d. Compute total loss  $L_{total} = L_{kmeans} + \alpha * L_{contrastive}$ .
- e. Compute the gradient of  $L_{total}$  with respect to centroids.
- f. Update centroids using the gradients.

4: Assign each data point to the closest centroid based on the updated centroids.

5: Return the final cluster centroids and cluster assignments.

---

In the above,  $L_{kmeans}$  is the K-means loss, typically the sum of squared distances from each point to its assigned centroid.  $distance_i$  is the distance from point  $i$  to its nearest centroid,  $\mathcal{S}_i$  is the  $i^{\text{th}}$  row of the similarity matrix  $\mathcal{S}$ , and  $\mathcal{S}_{ii}$  is the similarity of point  $i$  to its own cluster. The contrastive loss is computed for each point and then used to adjust the centroid positions.

To create a feature space specifically representing asymmetry between slices, we start by applying the K-means clustering algorithm. This process automatically groups slices with similar asymmetry features. Building on our previous volume-level analysis, we focus on the six most common slice clusters that can be considered as six representative asymmetry "profiles." To classify a whole MRI, each of its 15-23 slices are assigned to

one of these six profiles using majority voting. This slice-by-slice assessment determines the overall asymmetry categorization for the whole breast MRI.

### 2.2.6 Validation

In our model assessment, we conducted two steps of validation. Initially, in the clustering step, we utilized the Silhouette score to gauge the quality of the K-Means clustering, verifying the optimal number of clusters obtained from the Elbow Criterion [27][28]. This method was employed to both finding the optimal number of clusters and validating the clustering.

Our clustering approach was assessed using cross-validation. The dataset, with 50 positive and 159 negative instances, was split into 10 subgroups. Each test involved training on 9 and validating on 1 subgroup, assigning scores from 0 to 1 to indicate cancer likelihood, with higher scores indicating higher likelihood and better model performance. This cross-validation cycle was repeated 10 times, rotating the subgroup used for validation to ensure thorough evaluation.

In the realm of unsupervised clustering, especially when tackling complex classifications, such as asymmetry detection, we face the inherent challenge of validating the model without definitive class labels. To overcome this challenge, we introduced a binary validation framework using labels derived from the subsequent screening MRI. These labels provide us with binary outcomes—'developed cancer' or 'remained healthy'—which are pivotal for assessing the predictive accuracy of our clustering model. By mapping the multifaceted clusters to these binary outcomes, we effectively created a bridge between unsupervised clusters and a verifiable clinical endpoint. In doing so, we employed metrics, such as true-positive rates, false-positive rates, and the area under the ROC curve (AUC), to approximate the model's capacity for detecting anomalies.

This validation approach enables us to quantify the model's performance in terms of both meaningfulness and clinical relevance. It is a methodological compromise that allows for the evaluation of our model's discriminatory power, acknowledging the discrepancy that

arises from the lack of a direct match between the unsupervised clusters in our training data and the binary outcomes of subsequent screening. This validation strategy thereby offers a feasible solution to demonstrate the model's potential utility in a clinical setting, despite the absence of explicit labels within the training phase.

## 2.3 « Results »

### 2.3.1 Data Augmentation Validation

By simulating a reasonable amount of body rotation through finite element analysis and assigning different hyperelastic parameters, we generated new realistic breast MR image data. Figure 2-4 showcases slice cross-sections as sample illustrations of synthetic images generated using the developed augmentation techniques. While ensuring that the heterogeneous nature of the breast tissue and its composition is retained, contrary to traditional augmentation techniques, the proposed augmentation technique incorporates realistic redistribution of the tissue components. This underscores the limitations of traditional slice-based data augmentation methods, such as scaling and translation, which can result in loss or introduction of spurious information.

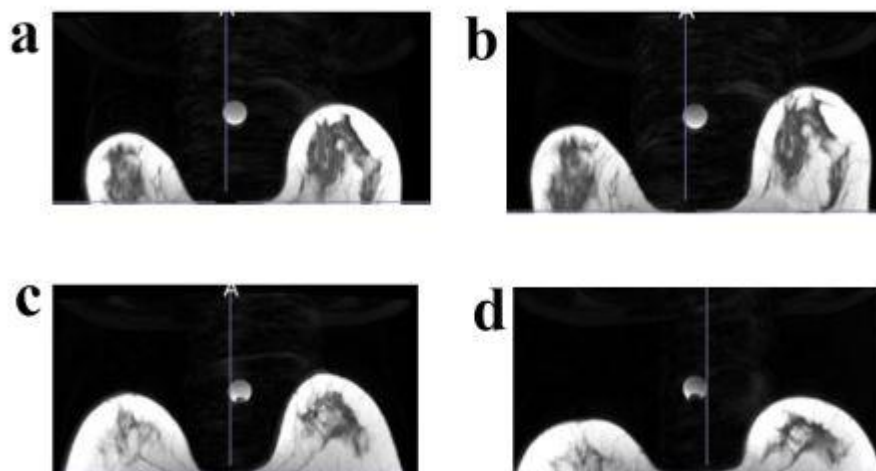


**Figure 2-4: (a)(c) Original breast slice MRI images (b)(d) Slice images from the volumes generated by assigning different hyperelastic parameters and applying rotations at various angles.**

### 2.3.2 Feature Engineering

We analyzed the importance of the extracted features during clustering and conducted necessary feature selection. GLCM (Gray Level Co-occurrence Matrix) and shape-based features emerge as particularly significant, given their higher median values and interquartile ranges, suggesting these features' robust influence on clustering. Figure 2-5 delineates a comparative view of the initial number of extracted features against those retained after the feature selection process. It is observed that both GLCM and shape-based features not only have a higher initial count, indicative of their extensive extraction, but also a significant proportion of these features are preserved post-selection. This retention underscores the paramount relevance of these features, reflecting their essential contribution to the clustering algorithm's ability to discern intricate patterns within the data. The substantial proportion of GLCM features retained—amounting to 21 out of the original 24—signifies their integral role in capturing textural information, which is pivotal in volume analysis. Similarly, the complete retention of shape-based features, with all 16 initially extracted features being selected, underscores their indispensable

utility in characterizing the geometrical aspects of the volumes. This strategic selection of features culminates in a refined set of attributes that possess a potent impact on clustering outcomes. By focusing on features with high discriminative power, our methodology ensures that the clustering is influenced by the most informative aspects of the data. Consequently, GLCM and shape-based features are likely to be pivotal for the accurate classification of volumes.

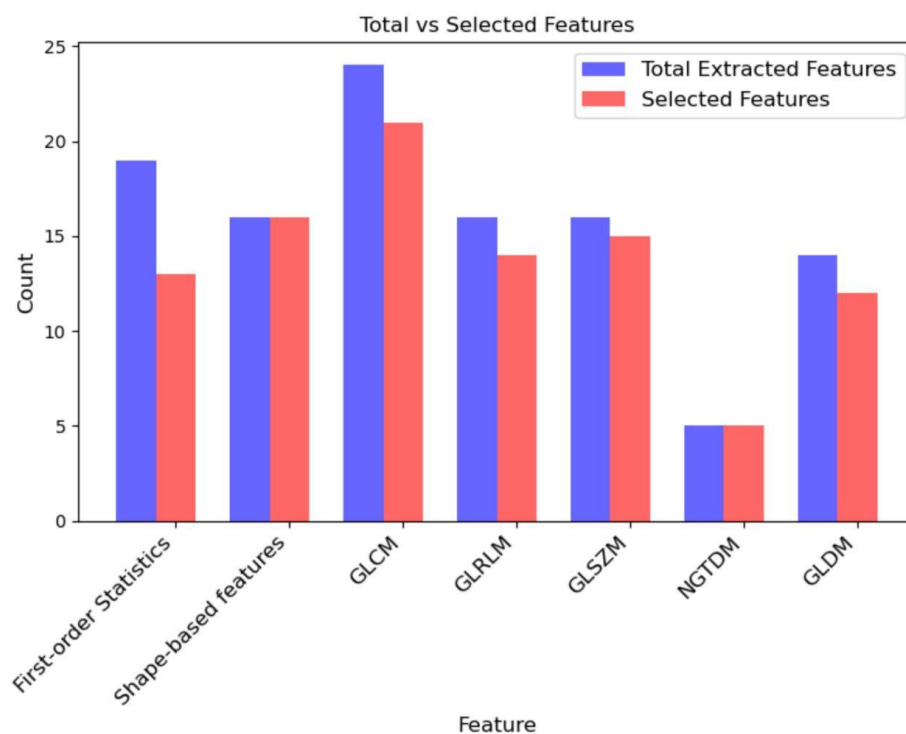
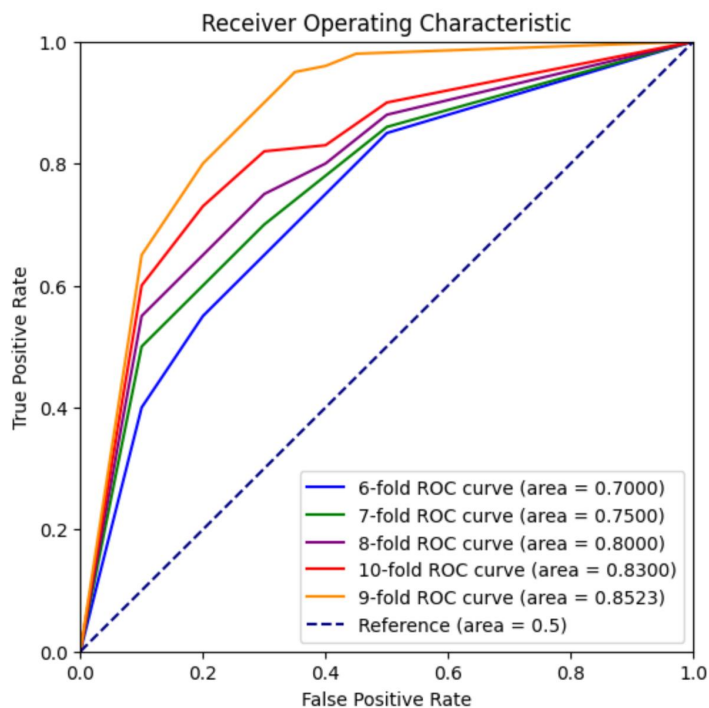


**Figure 2-5: Comparative analysis of initially extracted and ultimately selected features in volume-by-volume clustering.**

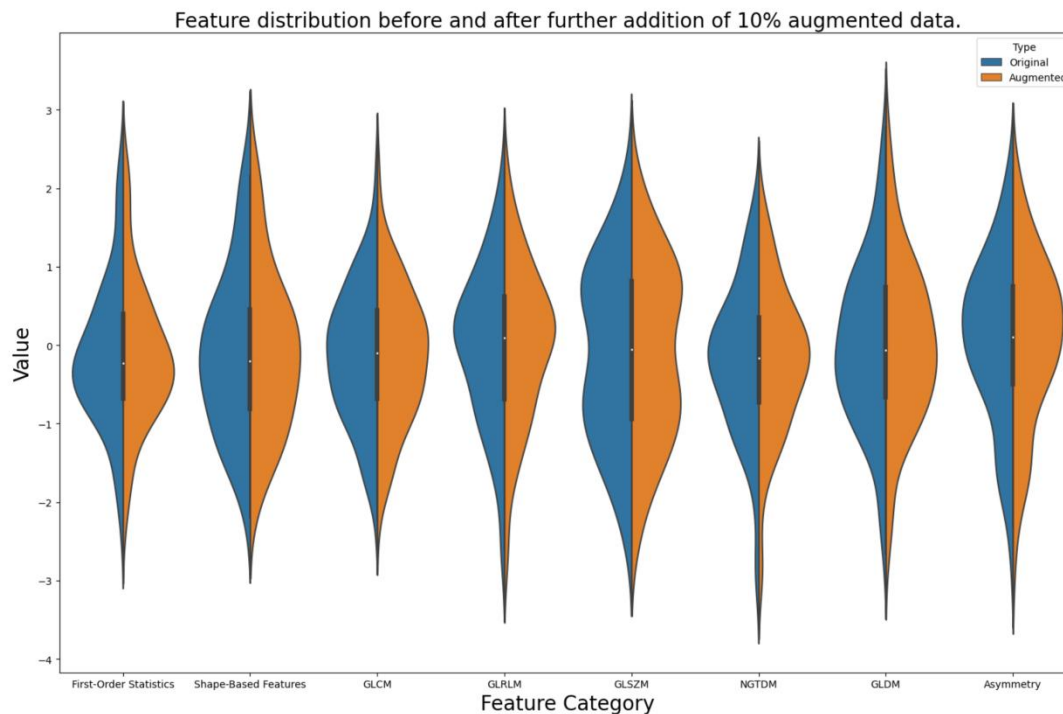
### 2.3.3 Clustering

The robustness of our volume-by-volume clustering approach is exemplified by the ROC curve (receiver operating characteristic curve) shown in Figure 2-6, which illustrates the model's ability to discriminate between two health states. By consolidating the six

clusters derived from unsupervised clustering into two encompassing categories, we computed the Area Under the Curve (AUC) for our model. An AUC of 0.85 denotes a high level of accuracy in this binary validation, affirming the effectiveness of our approach in categorizing volume data as indicative of cancer development or absence. This binary validation, while simplified, it provides a pragmatic measure of the model's predictive precision in a clinical context. In Figure 2-7, by comparing feature distributions, we demonstrated the convergence of data augmentation. This violin plot compares the distributions of eight different feature categories, both before and after considering 10% additional data augmentation. Each pair of violins represents a feature category, with the left half showing the original data and the right half showing the data after augmentation. Differences in the distribution shapes and center locations reflect the impact of the augmentation process on each feature category.

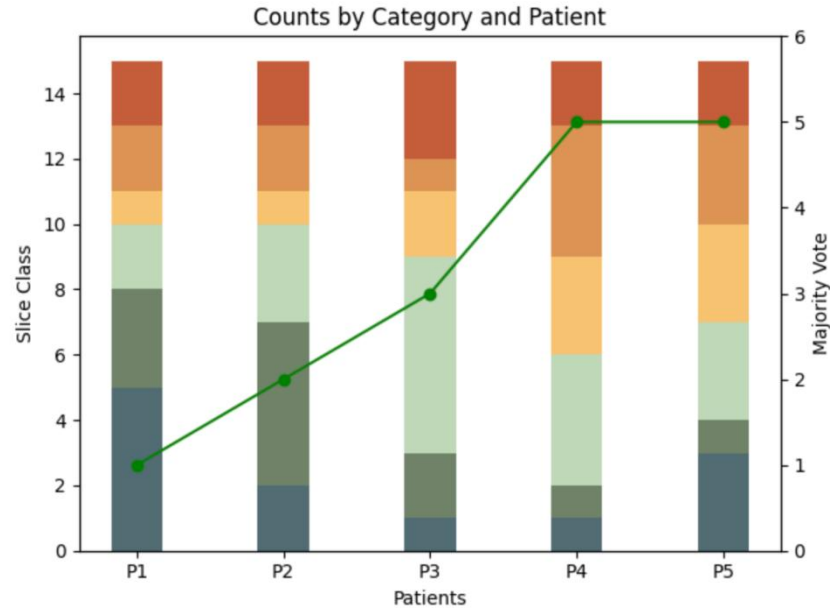


**Figure 2-6: ROC curve comparison. The orange curve represents our completed dataset of 210 cases examined on all positive and negative cases with AUC = 0.85 (reference AUC = 0.5).**



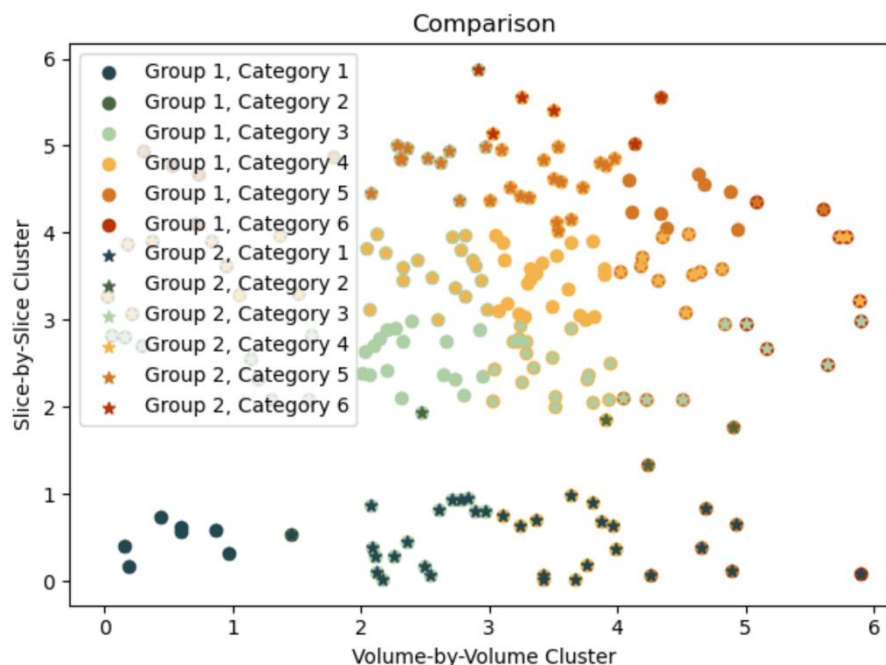
**Figure 2-7: Comparison between two sets of features (used for model and additional validation). Their centroids and distributions are very close, and the feature distributions almost have the same tendency.**

Figure 2-8 demonstrates the decision-making process for categorizing cases using a slice-by-slice clustering algorithm. The x-axis represents each case number, and the left y-axis shows the statistical value of the number of slices in different categories, depicted in six colors layered from bottom to top within each case. The right y-axis indicates the final classification of the case, determined by a majority vote, represented by green dots. For instance, case P2 predominantly falls into Category 2 based on the highest number of slices, hence it is classified under Category 2. Case P4 has an equal number of slices in both Category 3 and Category 5; however, it is ultimately classified under Category 5. This clarification reveals that higher category numbers suggest a greater likelihood of developing cancer. Therefore, when there's a tie in the number of slices between two categories, the case is assigned to the higher risk category to avoid missing a potential positive diagnosis. This approach emphasizes caution, prioritizing the identification of potential cancer risks even in closely contested categorizations.



**Figure 2-8: Example of classification for five cases using the slice-by-slice clustering method, with the stacked bars representing the count of MRI slices in each risk category and a green line indicating the final risk category determined by majority vote.**

Since the two clustering methods take into account the tissue distribution of breast volumetric and the characteristics of each slice of MRI images respectively, we compared the results of the two classification methods. As illustrated in Figure 2-9, a comparative analysis of two distinct clustering methods—volume-by-volume clustering, which evaluates breast tissue distribution across the entire volumetric data, and slice-by-slice clustering, which considers the characteristics inherent to each individual MRI slice. The scatter plot shows a strong correlation between the two methods, with a high degree of consistency observable by the alignment of data points. Approximately 95% of the cases fall into congruent classification regions across both methodologies, underscoring the reliability of clustering outcomes when examining tissue characteristics from different perspectives. The convergence of results suggests that both methods are robust.



**Figure 2-9: Detailed comparison of clustering results between volumetric and sliced clustering methods, where the two classification methods have a high degree of consistency, with 95% of the points falling within the same classification region.**

In Table 2-2 we compared the performance of the two clustering methods for a classification model in terms of True Positives (TP), True Negatives (TN), False Negatives (FN), and False Positives (FP). We analyzed the performance by calculating the following metrics for both models: Accuracy (the proportion of true results among the total number of cases examined), Precision (the proportion of positive identifications that were actually correct, Recall (Sensitivity) (the proportion of actual positives that were identified correctly), and F1 Score (the harmonic mean of precision and recall). The results reveal that the slice-by-slice method detected slightly more true positive cases (142) than the volume-by-volume method (138), indicating a marginally higher capacity for identifying breast cancer instances. However, it detected fewer true negative cases (20) compared to the volume-by-volume method (26), which may suggest a reduced ability to confirm non-cancerous cases. Both methods produced a similar number of false positives (41 for volume-by-volume, 40 for slice-by-slice), which affects the number of patients who might undergo unnecessary further testing. However, the volume-by-volume method

resulted in fewer false negatives (4) compared to the slice-by-slice method (7), implying it is less likely to miss cancer cases. The accuracy of the volume-by-volume method stands at 78.47%, compared to 72% for the slice-by-slice method. This suggests that overall, the volume-by-volume approach is more reliable for making the correct diagnosis. The precision metric of the slice-by-slice approach (78%) was marginally more precise than the volume-by-volume approach (77.1%). The recall for the volume-by-volume method is 97.2%, which is higher than that of the slice-by-slice method at 95.3%. This metric is critical in medical diagnostics, as a higher recall reduces the risk of missing true cancer cases. The F1 Score of volume-by-volume method scored 86.1%, slightly higher than the slice-by-slice method's 85.8%. This indicates a slight advantage in terms of the overall balance between precision and recall. In summary, the volume-by-volume method demonstrates a higher accuracy and F1 score, suggesting it may be more effective overall compared to the slice-by-slice approach. However, the difference in F1 score between the two methods is not substantial, indicating that both methods are reasonably effective. The choice between methods may come down to specific clinical needs and the operational context. For instance, if minimizing missed diagnoses is paramount, the higher recall of the volume-by-volume method may be preferable. On the other hand, if precision is more critical, the slice-by-slice method could be favored.

**Table 2-2: Comparative performance metrics of breast cancer detection models.**

	Volume-by-Volume	Slice-by-Slice
True-Positive	138	142
True-Negative	26	20
False-Negative	4	7
False-Positive	41	40
Accuracy	78.47%	72%
Precision	77.1%	78.0%
Recall	97.2%	95.3%
F1 Score	86.1%	85.8%

## 2.4 « Discussion and Conclusions »

In this work, we presented an end-to-end framework for determining a woman's risk of breast cancer development through the analysis of her bilateral breast MRI images. This research approach also includes the development of methods for identifying high-risk women based on their breast MRI images. It proposes a new perspective that links machine learning architectures to the biomechanical characteristics of breast tissue for medical image augmentation. The proposed clustering methods has the potential of being impactful for breast cancer prevention in a substantial female population exhibiting notable breast bilateral asymmetry.

To our knowledge, our study differentiates itself from previous works by incorporating both asymmetry and longitudinal study analysis in predicting breast cancer development risk. While Tao et al., 2021 [28] utilized Multiparametric MRI (mpMRI) to derive image

radiomics features for breast cancer prediction, overlooking the asymmetry feature. Additionally, the study faced two key constraints: it focused solely on women aged 42-50 and employed a cross-sectional, rather than longitudinal, methodology, thus limiting observations to a single scan. The majority of similar studies conducted so far have focused on classifying benign and malignant tumors using histopathological image information, neglecting the estimation of developing cancerous tissue and not considering bilateral asymmetry as a significant factor in cancer development [29-31]. Their approaches primarily centered on classifying medical images that already displayed obvious cancerous features, ignoring the identification of tissue that could potentially develop into abnormal growths. Some works, like those carried out by [32-33], proposed Computer-Aided Detection (CAD) systems based on deep neural networks. Nevertheless, such algorithms inherently have high computational complexity and heavily rely on large initial training data sets. In contrast, through refined feature engineering and fully leveraging the distinctive characteristics of MRI imaging, we have addressed the challenge of limited data availability. Traditional data augmentation approaches, such as positive or negative 90° rotations to increase the training data size, have been employed [34-36]. However, our experimental verification found that this traditional technique contributed minimally to increasing the diversity of high-level features.

In our study, we applied Finite Element (FE) simulation for data augmentation with the aim of improving the accuracy of machine learning methods and addressing the issue of phantom introduction that is highly likely with traditional data augmentation techniques. Compared to conventional augmentation methods limited to individual slice modification (e.g., scaling, rotation), our technique excels in simulating the complex dynamics of true breast deformation during the MRI acquisition process. Our data augmentation pipeline produces synthetic MRI images that closely resemble real-world cases. This FE-based warping MRI image method can retrofit successful medical image augmentation frameworks in the biomedical image processing field, where data is scarce. This significantly can potentially improve the accuracy of machine learning models. Our physics-based warping image framework utilizes spatial references to achieve non-linear transformations, considers tissue mechanical properties, and eliminates the risk of

producing unrealistic images that could potentially distort the feature space used in various machine learning algorithm development.

Building on the innovative Finite Element (FE) simulation for data augmentation discussed previously, which notably enhances the realism of synthetic MRI images by simulating the complex nature of breast deformation, the sufficiency of the dataset used in our analysis is further supported by our comprehensive approach to data collection, preparation and analysis. Firstly, the “slice-by-slice” approach employed in our analysis provided a substantial amount of data. Each case in our dataset included an average of 20 slices, accumulating over 200 cases. This provided more than 4,000 slices of asymmetric features to populate the feature space, ensuring a robust dataset. The richness of these data, both in terms of quantity and granularity of detail per case, significantly contributes to the reliability of our machine learning models by enhancing the representativeness of the dataset across different variations of breast tissue and pathological conditions. It is remarkable that the classification results obtained with the “volume-by-volume” approach are similar to the “slice-by-slice” approach, lending credibility to the latter approach results despite including only ~200-volume dataset. Second, the study employed these data as part of a preliminary classifier development, aimed at assessing its potential before advancing to clinical trials. The current stage is a pilot study aimed at understanding the performance of the classifier under controlled conditions and setting benchmarks for accuracy, sensitivity, and specificity. Although the results thus far are promising, the progression to clinical implementation will necessitate further validation with an expanded dataset. Finally, a common limitation in medical imaging analysis pertains to the accessibility and availability of the type of data. Our data involved sequential dual scans and biopsy check for double verification. Such data are not only rare but also difficult to acquire because of the inherent challenges in convincing asymptomatic individuals to undergo very likely unnecessary procedures.

In this work, we explored the potential of MRI-derived asymmetry features and achieved consistent classification outcomes at both the volumetric and slice-based levels. To consider the full spectrum of methodologies applied to feature extraction from MRI data, we experimented with various machine learning networks for feature extraction,

including convolutional neural networks (CNNs), which are notably proficient in image analysis. Despite the potential of CNNs, we recognize a critical need for interpretability in the medical imaging domain. The blackbox nature of such networks often obscures the internal mechanics of their decision-making processes, rendering the analysis less transparent to clinicians and researchers. Consequently, to bolster the interpretability of our model and provide valuable insights into the asymmetric features that influence breast MRI analysis, we opted for methodologies that allow a clearer understanding of the feature-extraction process. This strategic decision augments the practical relevance of our study as it bridges the gap between complex machine learning techniques and clinical applicability. Although the amount of data used in this work does not satisfy complex machine learning demands, the proof-of-concept study introduces a novel approach to small-volume medical image analysis. Future studies will consider utilizing larger datasets of public longitudinal breast MRI images for better performance.

In summary, breast cancer is primarily caused by anomalous growth of breast tissue, accounting for an estimated 7% of all mortalities [37]. Identifying cancerous/malignant lesions at an early stage is challenging due to the low traceability of small-sized tumors, and late-stage diagnosis may not significantly prevent patient mortality. Therefore, our efforts to provide an architecture for breast cancer risk estimation and provision for early-stage diagnosis may be considered as an important step towards this crucial objective.

## References

- [1] AS Kusano et al. (April 2006). A Prospective Study of Breast Size and Menopausal Breast Cancer Incidence. *International Journal of Cancer*. 118(8):2031-4.
- [2] Pui San Tan, Maya Alsheh Ali, Mikael Eriksson, Per Hall, Keith Humphreys, Kamila Czene, Mammography features for early markers of aggressive breast cancer subtypes and tumor characteristics: A population-based cohort study, *International Journal of Cancer*, 10.1002/ijc.33309, 148, 6, (1351-1359), (2020).

- [3] P. Casti, A. Mencattini, M. Salmeri and R. M. Rangayyan, "Analysis of Structural Similarity in Mammograms for Detection of Bilateral Asymmetry," in *IEEE Transactions on Medical Imaging*, vol.34, no.2, pp.662-671,2015.
- [4] Sue M Hudson, Louise S Wilkinson, Bianca L De Stavola, Isabel dos-Santos-Silva, Left–right breast asymmetry and risk of screen-detected and interval cancers in a large population-based screening population, *The British Journal of Radiology*, 10.1259/bjr.20200154, (20200154), (2020).
- [5] Zhiqiong Wang, Yukun Huang, Mo Li, Hao Zhang, Chen Li, Junchang Xin, Wei Qian, Breast mass detection and diagnosis using fused features with density, *Journal of X-Ray Science and Technology*, 10.3233/XST-180461, (1-22), (2019).
- [6] Kathleen R. Brandt, Christopher G. Scott, Diana L. Miglioretti, Matthew R. Jensen, Amir P. Mahmoudzadeh, Carrie Hruska, Lin Ma, Fang Fang Wu, Steven R. Cummings, Aaron D. Norman, Natalie J. Engmann, John A. Shepherd, Stacey J. Winham, Karla Kerlikowske, Celine M. Vachon, Automated volumetric breast density measures: differential change between breasts in women with and without breast cancer, *Breast Cancer Research*, 10.1186/s13058-019-1198-9, 21, 1, (2019).
- [7] Sue M Hudson, Louise S Wilkinson, Rachel Denholm, Bianca L De Stavola, Isabel dos-Santos-Silva, Ethnic and age differences in right-left breast asymmetry in a large population-based screening population, *The British Journal of Radiology*, 10.1259/bjr.20190328, (20190328), (2019).
- [8] Price, E.R., Hargreaves, J., Lipson, J.A., Sickles, E.A., Brenner, R.J., Lindfors, K.K., Joe, B.N., Leung, J.W., Feig, S.A., Bassett, L.W., Ojeda-Fournier, H., Daniel, B.L., Kurian, A.W., Love, E., Ryan, L., Walgenbach, D.D., & Ikeda, D.M. (2013). The California breast density information group: a collaborative response to the issues of breast density, breast cancer risk, and breast density notification legislation. *Radiology*, 269 3, 887-92 .

- [9] Northcott JM, Dean IS, Mouw JK, Weaver VM. Feeling Stress: The Mechanics of Cancer Progression and Aggression. *Front Cell Dev Biol.* 2018; 6:17.  
doi:10.3389/fcell.2018.00017
- [10] Brooksby, B., Pogue, B. W., Jiang, S., ... & Paulsen, K. D. (2006). Imaging breast adipose and fibroglandular tissue molecular signatures by using hybrid MRI-guided near-infrared spectral tomography. *Proceedings of the National Academy of Sciences*, 103(23), 8828-8833.
- [11] Yan, Z., Zeng, Y., Zhang, Y., Jia, Z., Tian, Q., Han, J., & Guo, H. (2017). A novel image marker extraction method for short-term breast cancer risk prediction. *Journal of Digital Imaging*, 30(6), 797-805. [Link to full text](#)
- [12] Chaurasia, V., Pal, S., & Tiwari, A. (2018). Prediction models for breast cancer survivability: a review. *Computers in biology and medicine*, 92, 168-175. [Link to full text](#)
- [13] Li, H., Zhu, Y., Burnside, E. S., Drukker, K., Hoadley, K. A., Fan, C., ... & Whitman, G. J. (2016). MR imaging radiomics signatures for predicting the risk of breast cancer recurrence as given by research versions of MammaPrint, Oncotype DX, and PAM50 gene assays. *Radiology*, 281(2), 382-391
- [14] Samani A, Plewes D. A method to measure the hyperelastic parameters of ex vivo breast tissue samples. *Phys Med Biol.* 2004 Sep 21;49(18):4395-405.
- [15] Dempsey SCH, O'Hagan JJ, Samani A. Measurement of the hyperelastic properties of 72 normal homogeneous and heterogeneous ex vivo breast tissue samples. *J Mech Behav Biomed Mater.* 2021 Dec;124:104794.
- [16] Hinrichs, C., Singh, V., Mukherjee, L., Xu, G., Chung, M. K., Johnson, S. C., & Alzheimer's Disease Neuroimaging Initiative. (2009). Spatially augmented LPboosting for AD classification with evaluations on the ADNI dataset. *Neuroimage*, 48(1), 138-149.
- [17] Song, C., Ristenpart, T., & Shmatikov, V. (2017, October). Machine learning models that remember too much. In *Proceedings of the 2017 ACM SIGSAC Conference on computer and communications security* (pp. 587-601).

- [18] Alterson R, Plewes DB. Bilateral symmetry analysis of breast MRI. *Phys Med Biol*. 2003 Oct 21;48(20):3431-43. doi: 10.1088/0031-9155/48/20/011.
- [19] Brown, M. L., Williams, W. J., & Hero, A. O. (1994, April). Non-orthogonal Gabor representation of biological signals. In *Proceedings of ICASSP'94. IEEE International Conference on Acoustics, Speech and Signal Processing (Vol. 4, pp. IV-305)*. IEEE.
- [20] van Griethuysen JJM, Fedorov A, Parmar C, Hosny A, Aucoin N, Narayan V, et al. Computational Radiomics System to Decode the Radiographic Phenotype. *Cancer Res*. 2017;77: e104–e107. pmid:29092951
- [21] Li, J., Cheng, K., Wang, S., Morstatter, F., Trevino, R. P., Tang, J., & Liu, H. (2017). Feature selection: A data perspective. *ACM computing surveys (CSUR)*, 50(6), 1-45.
- [22] Peng H, Long F, Ding C. Feature selection based on mutual information criteria of max-dependency, max-relevance, and min-redundancy. *IEEE Trans Pattern Anal Mach Intell*. 2005; 27:1226–38.
- [23] Hamerly, G., & Elkan, C. (2003). Learning the k in k-means. In *Advances in Neural Information Processing Systems (Vol. 16)*.
- [24] Hallac, D., Leskovec, J., & Boyd, S. (2015, August). Network lasso: Clustering and optimization in large graphs. In *Proceedings of the 21th ACM SIGKDD international conference on knowledge discovery and data mining (pp. 387-396)*.
- [25] Li, Y., Hu, P., Liu, Z., Peng, D., Zhou, J. T., & Peng, X. (2021, May). Contrastive clustering. In *Proceedings of the AAAI conference on artificial intelligence (Vol. 35, No. 10, pp. 8547-8555)*.
- [26] Shahapure, K. R., & Nicholas, C. (2020, October). Cluster quality analysis using silhouette score. In *2020 IEEE 7th international conference on data science and advanced analytics (DSAA) (pp. 747-748)*. IEEE.
- [27] Kodinariya, T. M., & Makwana, P. R. (2013). Review on determining number of Cluster in K-Means Clustering. *International Journal*, 1(6), 90-95.

- [28] Huang L, Tao Q, Zhao P, Ji S, Jiang J, van der Geest RJ, Xia L. Using multi-parametric quantitative MRI to screen for cardiac involvement in patients with idiopathic inflammatory myopathy. *Sci Rep.* 2022 Jun 14;12(1):9819. doi: 10.1038/s41598-022-13858-y. PMID: 35701509; PMCID: PMC9198094.
- [29] Hirra, I., Ahmad, M., Hussain, A., Ashraf, M.U., Saeed, I.A., Qadri, S.F., Alghamdi, A.M., & Alfakeeh, A.S. (2021). Breast Cancer Classification From Histopathological Images Using Patch-Based Deep Learning Modeling. *IEEE Access*, 9, 24273-24287.
- [30] Hameed, Z., Garcia-Zapirain, B., Aguirre, J.J., & Isaza-Ruget, M.A. (2022). Multiclass classification of breast cancer histopathology images using multilevel features of deep convolutional neural network. *Scientific Reports*, 12.
- [31] Murcia-Gómez, D., Rojas-Valenzuela, I., & Valenzuela, O. (2022). Impact of Image Preprocessing Methods and Deep Learning Models for Classifying Histopathological Breast Cancer Images. *Applied Sciences*.
- [32] de Freitas Barbosa, V.A., Félix da Silva, A., de Santana, M.A., Rabelo de Azevedo, R., Fernandes de Lima, R.D., & dos Santos, W.P. (2022). Deep-Wavelets and convolutional neural networks to support breast cancer diagnosis on thermography images. *Computer Methods in Biomechanics and Biomedical Engineering: Imaging & Visualization*, 11, 895 - 913.
- [33] Ahmad, N., Asghar, S., & Gillani, S.A. (2021). Transfer learning-assisted multi-resolution breast cancer histopathological images classification. *The Visual Computer*, 38, 2751 - 2770.
- [34] Kim, M., & Bae, H. (2020). [Data Augmentation Techniques for Deep Learning-Based Medical Image Analyses]. *Taehan Yongsang Uihakhoe chi*, 81 6, 1290-1304 .
- [35] Chen, X., Li, Y., Yao, L., Adeli, E., & Zhang, Y. (2021). Generative Adversarial U-Net for Domain-free Medical Image Augmentation. *ArXiv*, abs/2101.04793.

[36] Zhang, G., Dang, H., & Xu, Y. (2022). Epistemic and aleatoric uncertainties reduction with rotation variation for medical image segmentation with ConvNets. *SN Applied Sciences*, 4, 1-11.

[37] Sun YS, Zhao Z, Yang ZN, Xu F, Lu HJ, Zhu ZY, Shi W, Jiang J, Yao PP, Zhu HP. Risk Factors and Preventions of Breast Cancer. *Int J Biol Sci*. 2017 Nov 1;13(11):1387-1397. doi: 10.7150/ijbs.21635. PMID: 29209143; PMCID: PMC5715522.

## Chapter 3

### 3 « Machine-Learning Based Inverse Problem Technique to Determine Hyperelastic Parameters of Breast Tissue Under Zero-gravity Conditions »

#### 3.1 « Introduction »

Breast cancer remains a critical global health concern, driving extensive research to advance diagnostic and treatment methods. Biomechanical modeling utilizing the Finite Element Method (FEM) plays a valuable role in various breast cancer interventions. As of November 2023, approximately 60% of the publications on biomechanical modeling were published after 2015, indicating a rapidly growing field of research [1]. These models assist in surgical planning (e.g., brachytherapy and needle biopsy), the development of virtual reality surgical simulators, deformable image registration techniques, breast reconstruction surgeries, and personalized bra design [2-5]. Accurate FEM simulations depend heavily on precise modeling of breast tissue deformation and stress distribution, underscoring the vital importance of this area of research.

Breast tissue's inherent complexities pose a significant challenge in biomechanical modeling. Early models were often developed based on tissue linear elasticity assumptions. However, these models fail to capture the nonlinear behavior of breast tissue under the large strains common in medical procedures [6]. Consequently, hyperelastic constitutive laws, designed to handle both geometric and material nonlinearities, have become essential for accurate FEM simulation [7]. These hyperelastic models are fundamentally dependent on precise material parameters, which characterize the tissue's unique mechanical behavior. A diverse array of approaches exist for measuring soft tissue hyperelastic parameters. For the parameters of excised, homogenous tissue sample analysis, Samani et al. [8] developed an indentation technique coupled with inverse finite element model. This enabled them to obtain hyperelastic parameters for adipose and fibroglandular tissue using a 2<sup>nd</sup> order Polynomial model. The

precision and advantages offered by indentation methods have led numerous researchers to explore the mechanical properties of soft polymers and biological tissues. Zhang et al. [9] developed a model to assess the effects of friction and deformation on Young's modulus, introducing a kappa table for layered geometries. Lin [10] focused on overcoming Hertzian model limitations, applying hyperelastic strain energy functions to synthetic and biological tissues. Zhang [11] examined spherical indentation on hyperelastic materials, assessing various models' relationships between load, depth, and properties. Cao et al. [12] derived a load-depth expression for elastic layers, proposing a method to evaluate viscoelastic properties. Rauchs et al. [13] used spherical indentation on rubber, applying an inverse method to obtain material parameters modeled by the Zener model. Suzuki et al. [14] developed an analytical contact model for spherical indentation to estimate plantar soft tissue properties, offering a direct method without iterative finite element analysis. Chen et al. [15] utilized Finite Element modeling to compare hyperelastic models via nanoindentation, aiming to refine material property measurements without depth limitation. They later conducted indentation tests on silicone rubber, comparing results from indentation and tensile tests to validate hyperelastic models, showcasing the effectiveness of indentation in characterizing material properties [16]. Dempsey et al. [17] used data acquired from indentation testing of excised breast tissue to determine the hyperelastic parameters of adipose, fibroglandular, and mixed breast tissue. Collectively, these studies enhanced the precision of mechanical property measurements through computational and experimental approaches.

A variety of methodologies have been explored to measure soft tissue hyperelastic parameters, from indentation techniques to advanced computational models. These methods have significantly contributed to our understanding of tissue mechanics, yet they often overlook the crucial impact of gravity on tissue deformation and initial stress distribution. [18]. The gravity effect is essential in mechanical characterization of highly deformable tissues such as the breast. This is due to the substantial deformation of samples of such tissues and their initial stress distribution before the mechanical testing is initiated. Without accounting for the influence of gravity load, data pertaining to tissue

mechanical stimulation through testing falls short in capturing the intrinsic mechanical properties of the tissue, leading to incomplete understanding of its behavior. Given the challenges mentioned above, some researchers have proposed alternative solutions to mitigate error. Griesenauer et al. [19] leveraged MR imaging to ascertain patient-specific stiffness properties of breast tissues under varied gravity-loaded configurations. This approach bolstered the precision of biomechanical models utilized in image-guided breast cancer surgery by fitting mechanical properties to these models. Conley et al. [20] explored the potential of supine MR images and biomechanical modeling in enhancing tumor localization during breast-conserving surgeries. By employing a combination of laser range scanning, tracked ultrasound, and innovative registration routines, this study demonstrated the utility of biomechanical models in improving the accuracy of tumor localization, thus reducing the necessity for subsequent corrective surgeries. Gao et al. [21] delved into experimental methods for evaluating the mechanical properties of very soft tissues, with a particular focus on the effects of gravitational forces. By employing global digital image correlation techniques, the study revealed the complexities of measuring soft tissue behavior under tension, proposing a novel method to estimate the zero-strain state. Collectively, a fundamental assumption underlying these aforementioned studies is the consideration of residual stress. This concept recognizes that tissues are not in a stress-free state even before any external diagnostic or surgical manipulation commences. The presence of residual stress influences the manner in which tissues respond to additional loads, such as those applied during mechanical testing or surgical interventions.

To address the prevalent issue of inaccurate hyperelastic parameter estimation due to overlooking initial stress and gravity impact, we introduce a machine-learning-based inverse-problem solution. Our approach leverages Neural Networks to bridge the gap between hyperelastic parameter sets obtained under different conditions. We carry out numerous accurate uniaxial testing simulations to generate datasets representing conventional testing conditions and stress-free states. Our innovative network seamlessly converts hyperelastic parameters obtained from conventional mechanical testing to their stress-free counterparts. To the best of our knowledge, this is the first work to employ

such an easy-implemented machine-learning approach for estimating stress-free hyperelastic parameters of soft tissue.

### 3.2 « Theory »

While breast tissue exhibits a complex composition, for the purposes of reasonable simplification aligned with established literature [22], we model it as an isotropic solid. Such an approach is known to capture mechanical responses under the external loads typical of biomedical scenarios effectively. Typically, under such loading scenarios, the breast exhibits large deformation which necessitates geometric nonlinearity consideration in its modeling. Combined with the known breast tissue intrinsic nonlinearity, it is imperative to model the breast tissue as hyperelastic and isotropic material. Central to modeling the mechanical behavior of breast tissue in biomedical stress-loading applications is the strain-energy function. This mathematical construct establishes the relationship between stress and strain, providing a robust means to characterize the material's response. This serves as the theoretical basis for the tissue uniaxial testing simulation in proposed technique.

The strain energy stored within material as it undergoes deformation is known as the strain-energy content [23]. Various constitutive models specifically tailored to breast tissue mechanics have been put forward to describe this strain-energy relationship. Each model leverages unique mathematical formulations and parameters to express the strain-energy function. To accurately estimate hyperelastic parameters in an isotropic material, a strain energy model is essential for relating the strain energy to the deformation parameters of the material. Traditionally, for a hyperelastic isotropic material, the strain energy is presented as a function of strain invariants:  $U(I_1, I_2, I_3)$ , where  $I_i$  represents the  $i^{th}$  strain invariant. From this formulation, we can derive a constitutive relation as Equation 3-1:

$$\boldsymbol{\sigma} = \frac{2}{J} \left( \frac{\partial U}{\partial I_1} + I_1 \frac{\partial U}{\partial I_2} \right) \mathbf{B} - 2 \frac{\partial U}{\partial I_2} \mathbf{B}^2 - p \mathbf{I} \quad (3-1)$$

In this formula:  $\boldsymbol{\sigma}$  represents the Cauchy stress tensor,  $J$  is the determinant of the deformation gradient, indicating the volume change during deformation,  $\mathbf{B}$  is the left Cauchy-Green deformation tensor, and  $\mathbf{B}^2$  is its square,  $p$  is the hydrostatic pressure, and  $\mathbf{I}$  is the identity tensor.

To model breast tissue mechanics, the strain-energy function provides a vital mathematical framework relating stress and strain. Diverse constitutive models, employing distinct equations and parameters, describe this function; prominent among them are the Yeoh [24], Ogden [25], and Veronda-Westmann [26] models. To enable seamless comparisons between models, we employ strain-based parameter translation. For example, Ogden model parameters can be mapped onto Yeoh parameters, and subsequently onto Veronda-Westmann parameters. This approach supports flexibility in selecting constitutive models for breast tissue analysis.

### **Yeoh Model**

The Yeoh model represents a simplified third-order polynomial form of the strain energy function, specifically tailored for modeling the behavior of elastomers. The strain energy function  $W$  is given by:

$$W = \sum_{i=1}^3 C_{i0} (I_1 - 3)^i \quad (3-2)$$

Here:

$C_{i0}$  are the material coefficients, with  $i$  indicating the order of the term.

$I_1$  is the first invariant of the Cauchy-Green deformation tensor.

The model utilizes three parameters:  $C_{10}$ ,  $C_{20}$ ,  $C_{30}$  corresponding to the coefficients of the polynomial that represent the material properties. Using Equation 3-2, the derivative of  $W$  with respect to  $I_1$  is:

$$\frac{\partial W}{\partial I_1} = \sum_{i=1}^3 i \cdot C_{i0} (I_1 - 3)^{i-1} \quad (3-3)$$

The stress-strain relationship for this model is as follows:

$$S = 2(C_{10} + 2C_{20}(I_1 - 3) + 3C_{30}(I_1 - 3)^2)(\lambda - \lambda^{-2}) \quad (3-4)$$

where  $S$  is the nominal stress.

### Ogden Model

The Ogden model is a hyperelastic material model that is also designed to accurately capture the nonlinear stress-strain behavior of elastomers. The strain energy function  $W$  for the Ogden model is defined as:

$$W = \sum_{i=1}^N \frac{2\mu_i}{\alpha_i^2} (\lambda_1^{\alpha_i} + \lambda_2^{\alpha_i} + \lambda_3^{\alpha_i} - 3) \quad (3-5)$$

In this formula,  $\mu_i$  and  $\alpha_i$  are material parameters that need to be determined experimentally.  $\lambda_1, \lambda_2, \lambda_3$  are the principal stretch ratios. The sum runs over  $N$  terms, where  $N$  defines the order of the model. For the 1<sup>st</sup> order formulation where  $N=1$ , 2 parameters ( $\mu_1, \alpha_1$ ) are required to capture the tissue behavior. Using Equation 3-5, the partial derivative of  $W$  with respect to  $\lambda_j$  without considering the pressure term  $p$  is as below, the pressure term  $p$  is included to enforce the incompressibility condition and would need to be determined from the boundary conditions of the specific problem.

$$\frac{\partial W}{\partial \lambda_j} = \sum_{i=1}^N \frac{2\mu_i}{\alpha_i} \lambda_j^{\alpha_i-1} \quad (3-6)$$

The nominal stress  $S$  along the direction of stretch  $\lambda_1$  is as follows:

$$S_1 = 2 \sum_{i=1}^N \mu_i (\lambda_1^{\alpha_i-1} - \lambda_1^{-\frac{\alpha_i}{2}-1}) \quad (3-7)$$

where  $S$  is the nominal stress. To ensure the reliability and accuracy of our material models, particularly in the face of incomplete or sparse experimental data, it is crucial to validate the chosen models against available experimental observations. Incomplete datasets can lead to the estimation of unstable model coefficients, thereby introducing potential inaccuracies into the modeling process. Such instabilities might not only affect the predictive capability of the models but also compromise their applicability in simulating real-world behaviors of materials under various loading conditions. To mitigate the risk of modeling errors and to enhance the stability of our model coefficients, we employ Drucker's stability inequality as a fundamental criterion for model validation. Drucker's stability inequality, expressed mathematically as:

$$\delta\sigma_{ij}\delta\epsilon_{ij} \geq 0 \quad (3-8)$$

serves as a cornerstone for ensuring that the material models exhibit stable response under all possible stress ( $\sigma_{ij}$ ) and strain ( $\epsilon_{ij}$ ) states. This inequality suggests that for a material to be considered stable, the incremental work done by the stress on the corresponding strain increment must be non-negative. This condition is critical for precluding physically unrealistic material responses that could arise due to the ill-posedness of model coefficients derived from incomplete data sets. By adhering to Drucker's stability criterion, we ensure that our modeling approach remains conservative and grounded in physically plausible behavior.

### 3.3 « Methods »

Our modeling approach establishes a framework for constructing two distinct hyperelastic parameter spaces representing the unloaded and loaded states of breast tissue. The core of this framework lies in the implementation of a Neural Network (NN), an advanced computational model that is adept at learning the intricate correspondences between large datasets. By training the NN, we enabled it to discern and establish a mapping relationship between the stress-free unloaded parameter space and its corresponding parameters under gravity loading. This was achieved by first constructing

comprehensive datasets that encapsulated the full spectrum of breast tissue behavior in both states, thereby providing the NN with a rich learning foundation. Our methodology comprises three core phases:

1. Construction of tissue hyperelastic parameter dataset of tissue under zero-state of stress (unloaded tissue). Henceforth, these parameters will be referred to as unloaded parameters. We carefully compile a comprehensive database of valid unloaded parameters. Building on established research [8], we focus on the Yeoh and first-order Ogden models. Our decision to prioritize the Yeoh model, characterized by parameters ( $C_1$ ,  $C_2$ ,  $C_3$ ), is rooted in its proven efficacy for capturing realistic tissue behavior.
2. Generation of tissue hyperelastic parameters under nonzero-state of stress (loaded tissue). Henceforth, these parameters will be referred to as loaded parameters. To generate the corresponding loaded parameter space, we leveraged finite element analysis (FEA). Specifically, we employ uniaxial test simulation to model the tissue mechanical behavior under corresponding load.

Neural Network Training: The NN undergoes a rigorous training process to extract the underlying relationship between the unloaded and loaded parameter spaces. This allows the trained NN to accurately predict unloaded parameters from a given set of loaded parameters. In essence, upon receiving a loaded parameter as input, the trained NN is capable of identifying the corresponding stress-free, unloaded parameter following the flowchart illustrated in Figure 3-1.

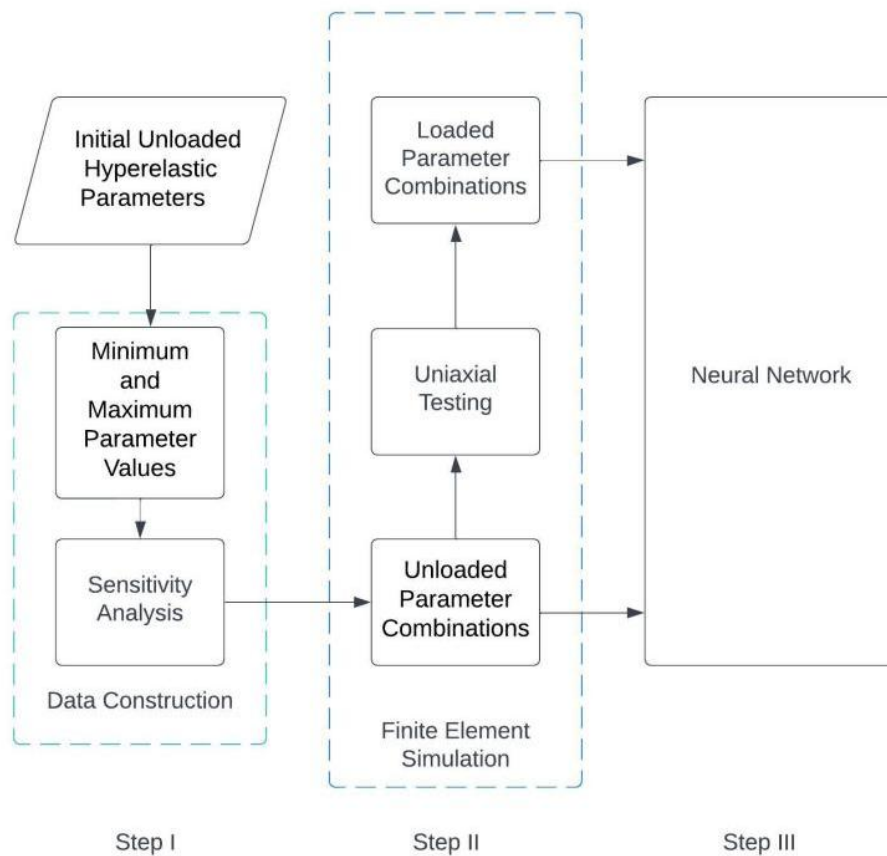


**Figure 3-1: Neural Network model for computing breast tissue stress-free (unloaded) hyperelastic parameters from loaded parameter counterpart**

### 3.3.1 Dataset Construction

The predictive power of our machine learning model is fundamentally supported by the creation of a comprehensive dataset. This dataset forms the backbone of our finite element analysis (FEA) and neural network (NN) training efforts, covering a wide array of hyperelastic parameters. We sourced our initial hyperelastic parameters from an extensive survey of well-established literature [8][27-28]. These studies are recognized for their effectiveness in modeling the behavior of hyperelastic materials, mirroring the characteristics of breast tissue. Among them, the Yeoh model stands out for its simplicity and proven capacity to mimic realistic tissue mechanics. Characterized by the parameters

$C_1$ ,  $C_2$ , and  $C_3$ , the Yeoh model provides flexibility:  $C_1$  sets the initial material modulus,  $C_2$  controls behavior under medium strain, and  $C_3$  influences the response under high strain conditions [29].

To rigorously explore the unloaded hyperelastic parameter space, we strategically modulated the values of  $C_1$ ,  $C_2$ , and  $C_3$  pertaining to the loaded parameter space through applying methodical incremental decreases of 5%. These adjustments spanned a spectrum from 5% to 40%. For example, a specific loaded parameter set might be modified to  $(0.7 \times C_1, 0.8 \times C_2, 0.95 \times C_3)$ , with each variation marking a distinct point within the stress-free parameter landscape. This approach allowed us to craft a broad spectrum of parameter configurations that represent the diverse mechanical behaviors of breast tissues effectively. Such variation enhances the model's ability to generalize across varying tissue conditions.

The determination of specific increments and the range for each  $C_1$ ,  $C_2$ , and  $C_3$  parameter was a deliberate process, guided by the insights derived from extensive extreme testing and sensitivity analysis conducted subsequently. Through extreme testing, we examined the model's resilience and behavior at the extremities of the parameter ranges, seeking out any potential vulnerabilities or atypical responses. Conversely, sensitivity analysis provided a deep dive into the impact of varying specific parameters on the model's output. By applying these robust methodologies, we refined our parameter selection and intervals, solidifying the dataset's fidelity.

### **3.3.1.1 Determining Minimum and Maximum Parameter Values**

To define a realistic and physically accurate parameter range for our unloaded dataset, we embarked on an in-depth exploration of extreme value determination. This process hinged on utilizing finite element analysis (FEA) to create a detailed model of breast

tissue and to simulate the effects of gravitational forces, using a variety of hyperelastic parameters to gauge their impact.

The decision to explore parameter reductions ranging from 5% to 40% was based on thorough research and analysis, not mere conjecture. By adjusting parameters across different scales and subjecting the tissue model to gravitational loading simulations, we were able to observe the resultant changes in stress-strain behavior closely. A key objective in this process was to adhere to Drucker's stability criterion, a cornerstone principle for preserving the physical authenticity of our model across various loading scenarios. This criterion helped us steer clear of unrealistic material responses. We systematically adjusted the scaling factor for parameter reduction until reaching a threshold beyond which the model exhibited signs of instability, thereby establishing a 40% reduction as the upper limit for parameter variability. This foundation allows us to simulate breast tissue mechanics with confidence, knowing our models are both scientifically robust and closely aligned with real-world behaviors.

### 3.3.1.2 Sensitivity Analysis

To refine the prediction of unloaded hyperelastic parameters, a detailed sensitivity analysis was performed. This analysis focused on understanding the influence of changes in the loaded Yeoh model coefficients  $C_{1loaded}$ ,  $C_{2loaded}$ , and  $C_{3loaded}$  on the stress-strain behavior. The goal was to fine-tune our methodology, ensuring it avoids unrealistic behaviors and accurately determines the parameter reduction increment for generating new data points within our unloaded parameter space.

1. Baseline Parameters: Initial loaded Yeoh parameters for breast tissue ( $C_{1loaded_0}$ ,  $C_{2loaded_0}$ ,  $C_{3loaded_0}$ ) were sourced from existing literature [17] to serve as our starting point.

2. Parameter Variation: We systematically reduced each parameter by 1% while keeping the others constant. For example, one of the generated parameter sets was  $(0.99 \times C_{1loaded\_0}, C_{2loaded\_0}, C_{3loaded\_0})$  which represents an unloaded parameter set. To obtain the corresponding loaded parameters, these adjusted sets of parameters were then utilized in the uniaxial testing FE models described in Section 3.3.2 where gravity force was also incorporated.

3. Output Analysis: Through fitting the stress-strain data generated from Step 2, we derived new sets of loaded parameters  $(C_{1loaded\_new}, C_{2loaded\_new}, C_{3loaded\_new})$ . We quantified the relative changes for each parameter as follows and assigned it to the corresponding sensitivity parameters  $S_{ij}$ . For example, for variation of  $C_{1loaded\_0}$ , we obtained the following:

$$S_{1i} = \frac{(C_{i loaded\_new} - 0.99C_{i loaded\_0})}{0.01C_{1 loaded\_0}} \quad (3-9)$$

4. Sensitivity Matrix Creation: By repeating step 1-3 for  $C_{2loaded\_0}$  and  $C_{3loaded\_0}$ , we obtained the following sensitivity matrix  $\mathbf{S}$  where  $S_{ij}$  parameters were used to decide the range of reduction of each of the  $C_i$  parameters to avoid generating unloaded  $C_i$  parameters that lead to non-physical loaded  $C_i$  parameters.

$$\mathbf{S} = \begin{bmatrix} S_{11} & S_{12} & S_{13} \\ S_{21} & S_{22} & S_{23} \\ S_{31} & S_{32} & S_{33} \end{bmatrix} \quad (3-10)$$

The following pseudo code illustrates the step-by-step process of the sensitivity analysis conducted to assess the impact of parameter variations on the stress-strain response of hyperelastic materials.

---

Algorithm Sensitivity Analysis

---

- 
- 1: Initialize  $C_{1loaded\_0}$ ,  $C_{2loaded\_0}$ ,  $C_{3loaded\_0}$
  - 2: do
  - 3: Assign a new set of parameters with  $(0.99C_{1loaded\_0}, C_{2loaded\_0}, C_{3loaded\_0})$
  - 4: Simulate uniaxial test combined with gravity simulation
  - 5: Generate simulated stress vs. strain
  - 6: Obtain an estimate of a (loaded) set of hyperelastic parameters ( $C_{1loaded\_new}$ ,  $C_{2loaded\_new}$ ,  $C_{3loaded\_new}$ )
  - 7: Calculate the following:

$$S_{11} = \frac{(C_{1loaded\_new} - 0.99C_{1loaded\_0})}{0.01C_{1loaded\_0}}$$

$$S_{12} = \frac{(C_{2loaded\_new} - C_{2loaded\_0})}{0.01C_{1loaded\_0}}$$

$$S_{13} = \frac{(C_{3loaded\_new} - C_{3loaded\_0})}{0.01C_{1loaded\_0}}$$

- 8: Repeat with C2 then C3
  - 9: Form S matrix
- 

To define the boundaries for parameter reductions, we adhered to three key principles during our sensitivity analysis:

1. Magnitude Assessment of Sensitivity Parameters within Each Row: This assessment focuses on comparing the magnitudes of  $S_{ij}$  values within each row of the sensitivity matrix. Parameters leading to the highest absolute  $S_{ij}$  values influence the model's response significantly. Therefore, they demand tighter reduction limits. For instance, if

$|S_{13}|$  is thrice  $|S_{11}|$  within the same row, it indicates that modifications to  $C_{3\text{loaded}_0}$  have a more substantial effect on the stress-strain relationship than similar changes to  $C_{1\text{loaded}_0}$ .

2. "Max" Value Significance: The element within each row with the highest absolute value, referred to as the "max" value, sets the strictest upper limit for parameter reduction. This ensures that adjustments remain within physically realistic boundaries, preventing the model from producing non-physical outcomes.

3. Negative Values: Entries in the sensitivity matrix with negative values require special attention. Negative  $S_{ij}$  values indicate that reductions in certain parameters can inversely affect the stress-strain curve, suggesting an opposite directional shift. Such findings necessitate a nuanced approach to parameter adjustment, ensuring that respective decreases do not inadvertently lead to unrealistic model behaviors.

### 3.3.2 Uniaxial Testing

In our research, uniaxial testing was conducted virtually through Finite Element Method (FEM) simulations within the Abaqus solver (SIMULIA, Providence, RI, USA). The core aim of employing this simulation technique was to construct the sensitivity matrix  $\mathcal{S}$  given in Equation 3-8. We initiated the process by creating a geometrically accurate model of a cylindrical breast tissue sample with a diameter and length of 15” and 30”, respectively. Then the material's hyperelastic parameters (e.g those obtained from Step 2 in Section 3.3.1.2 to represent the stress-free state of the breast tissue) were assigned. A unidirectional load, including gravity loading applied before the uniaxial test external loading, was simulated to apply along the axis of the cylinder model. This loading condition aimed at simulating the effects of uniaxial tensile or compressive forces that a sample would experience in actual laboratory testing. The uniaxial testing external loading was incrementally increased to span a gravity magnitude, ensuring comprehensive coverage of the material's behavior. Free sliding boundary condition was considered at the two ends of the cylinder model. Following the simulation of the

unidirectional loading on the cylindrical model the stress distribution was obtained which is illustrated in Figure 3-2. This visualization corroborates the simulated conditions and illustrates the material's response throughout the deformation process.

The FEM simulation provided detailed data on the stress and strain experienced by the model under each loading condition. At each incremental loading point, the stress was calculated by dividing the sum of axial reaction forces by the sample's cross-sectional area. These data points were used to construct simulated stress-strain curves. The collected stress-strain data served as a foundation for fitting new loaded parameters using Equations 3-3 and 3-5, pertaining to the Yeoh and Ogden models, respectively. The fitting process involved utilizing mathematical formulas to derive new Yeoh model parameters  $C_1$ ,  $C_2$ , and  $C_3$  from the observed stress-strain relationships. These newly fitted loaded parameters, derived from the uniaxial testing simulations, subsequently informed the next phase of our research: training a Neural Network (NN).

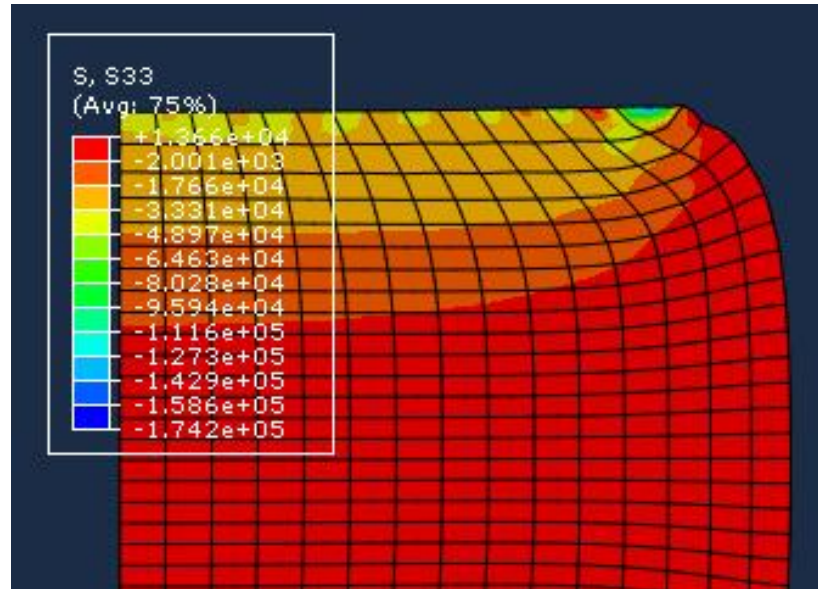


**Figure 3-2: Axial stress distribution of the cylindrical breast tissue sample with Yeoh hyperelastic parameters of  $C_1$ ,  $C_2$  and  $C_3$  obtained using Finite Element Analysis.**

### 3.3.3 Neural Network for Mapping Loaded to Unloaded Parameters

The development of our Neural Network (NN) model for estimating stress-free breast tissue hyperelastic parameters is grounded in a rigorous design process. This section outlines the architecture, optimization strategies, and the rationale behind the selection of activation functions, aiming to underscore the model's effectiveness and the methodological basis for our design choices.

The architecture of the NN comprises an input layer dedicated for the loaded hyperelastic parameters, several hidden layers, and an output layer. For training, the input layer is tasked with receiving ~1600 sets of loaded hyperelastic parameters derived from the simulated data obtained with corresponding ~1600 hyperelastic parameters dataset. The output layer for the same includes the same number of unloaded hyperelastic parameters dataset generated through scaling down loaded parameters obtained from the literature as described in Section 3.3.1.1. Subsequent processing is conducted through multiple hidden layers, which are instrumental in identifying patterns and navigating the complex nonlinear relationships characteristic of breast tissue mechanics. The culmination of this computational process is realized in the output layer, which delivers the estimated stress-free hyperelastic parameters.

The integration of the Adam optimizer within the initial hidden layer boosts the efficiency of the Neural Network (NN) significantly. Unlike traditional optimization methods, Adam incorporates an adaptive learning rate mechanism, leveraging first and second-order moment estimates of the gradients. This allows for the adjustment of the learning rate on a per-parameter basis, hence enhancing the model's capacity to navigate complex error landscapes effectively. The adaptive properties of Adam are particularly beneficial in overcoming challenges associated with convergence. Furthermore, the adoption of the Leaky Rectified Linear Unit (LeakyReLU) activation function across the

network marks a strategic improvement. LeakyReLU is designed to mitigate the "dying ReLU" problem, where neurons cease to activate and update during training. By introducing a small, positive slope for negative input values, LeakyReLU ensures that all neurons retain the potential for learning, thereby enhancing the network's training efficiency and convergence speed. This choice of activation function is pivotal in maintaining active gradient flow for near-zero inputs, facilitating faster learning and supporting the NN's ability to discern complex patterns in input data. Figure 3-3 illustrates the NN's architecture, emphasizing the layer configuration and the flow of data through the system.

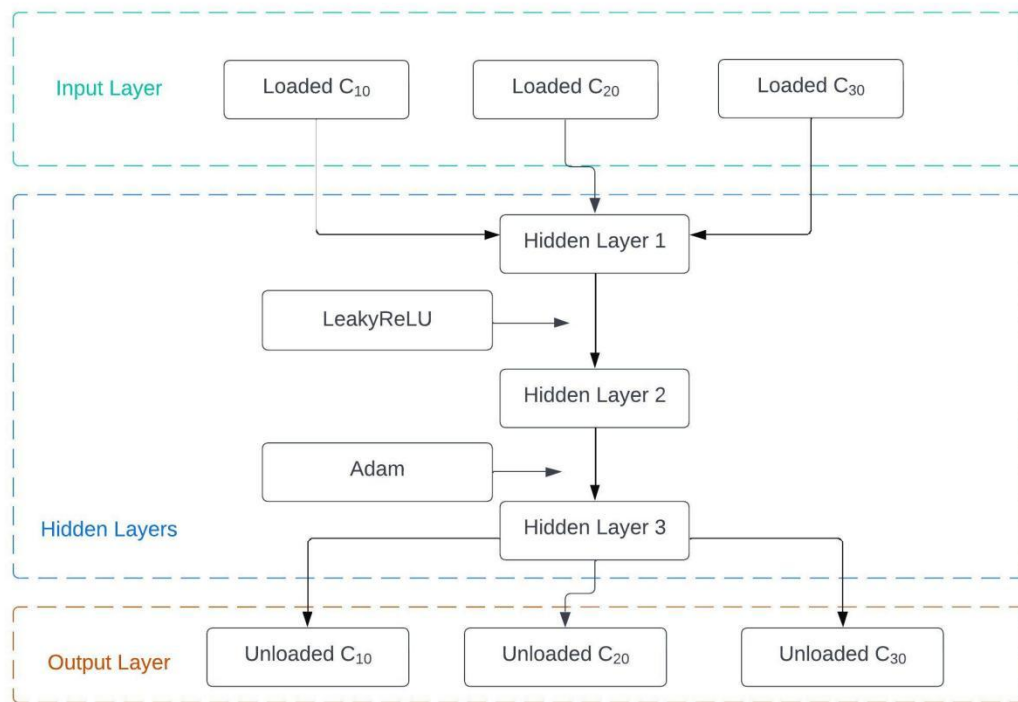


**Figure 3-3: Proposed NN architecture, illustrating the data flow and neuronal interconnections.**

Following the methodological setup described, an ablation study was systematically conducted to optimize the selection and configuration of neural network (NN) parameters during training. This study was crucial for ensuring that each parameter choice positively contributed to the overall performance and efficiency of the network. We began by methodically adjusting the learning rate and testing commonly used values such as 0.01, 0.001, and 0.0001. The rationale behind selecting these values was to explore how varying degrees of learning rates impact the validation error, which is a key indicator of the model accuracy and training speed. Similarly, we experimented with different batch sizes, including 8, 16, and 32, aiming to find the optimal balance between computational efficiency and the network's ability to update weights effectively, thereby influencing both the training dynamics and model performance. When configuring the network architecture, we carefully considered the risk of overfitting associated with varying numbers of hidden layers. The initial configurations ranged from one to four hidden layers, enabling us to observe the effects of increasing complexity on the model performance and the effectiveness of regularization strategies such as dropout. Adjustments were made to the dropout rates during these experiments to identify how different levels of regularization can help stabilize the training process and mitigate overfitting. Through this rigorous data-driven approach, we refined the network architecture to ensure that each component was necessary and optimally configured. A detailed analysis of how specific changes in learning rates, batch sizes, and network configurations affect key performance metrics provided invaluable insights into the dependencies and sensitivities of different network parameters. This meticulous methodology enabled our neural network to be effectively equipped to handle the complexities of the dataset, avoiding common issues, such as overfitting or inadequate learning capacity.

### 3.3.4 Data Fitting

After developing two distinct Neural Networks (NNs) tailored to the Yeoh and Ogden models, we embarked on a data fitting methodology to enhance the robustness of our models. Initially, the unloaded Yeoh parameters, as derived from the Yeoh NN, were utilized to generate a stress-strain curve. This curve was then employed to construct a representative dataset for the unloaded states through an analytical model given in Equation 3-3. Subsequently, this synthetic dataset was used to fit the Ogden model using Equation 3-5, resulting in parameters that are calibrated to the unloaded tissue response. A crucial step in our methodology involved validating the fitted Ogden parameters by employing stress-strain values generated from the Yeoh model to fit the Ogden model. This approach ensures that the Ogden model's parameters are finely tuned to mirror the experimental observations captured by the Yeoh model, focusing on achieving a close match across all evaluated strain points. This additional data fitting step significantly bolsters confidence in both modeling pathways, while the capability to cross-verify parameter sets obtained from different fitting techniques indirectly corroborates the accuracy of our unloaded parameter estimations. This approach is particularly invaluable given the experimental challenges associated with producing entirely stress-free breast tissue for direct validation.

The essence of this numerical fitting lies in minimizing the discrepancies between the stress-strain curves derived from Yeoh model and the Ogden model, formulated as follows:

$$\min_{\mu, \alpha} \sum_{i=1}^N [\sigma_{Yeoh}(\epsilon_i) - \sigma_{Ogden}(\epsilon_i; \mu, \alpha)]^2 \quad (3-11)$$

In this equation,  $\sigma_{Yeoh(\epsilon_i)}$  represents the stress values derived from the Yeoh model-based experiments for each strain ( $\epsilon_i$ ), while  $\sigma_{Ogden}(\epsilon_i)$  denotes the stress values predicted by the Ogden model for the same strain points, with  $\mu$  and  $\alpha$  being the Ogden model parameters under optimization. The goal is to minimize the sum of squared differences across all

data points  $N$ , ensuring the Ogden model parameters are accurately tuned to reflect the experimentally observed behaviors.

## 3.4 « Results »

### 3.4.1 Sensitivity Analysis

To accurately model the behavior of unloaded breast tissue, we performed sensitivity analysis as described in Section 3.3.1.2. This analysis scrutinized how adjustments to loaded hyperelastic parameters ( $C_{1loaded\_0}$ ,  $C_{2loaded\_0}$ ,  $C_{3loaded\_0}$ ) to obtain an unloaded parameter set influence the outcomes of our simulations, particularly the stress-strain curves derived from them. Through this structured examination, a sensitivity matrix, denoted as “ $S$ ”, was developed for the Yeoh model which is presented in Table 3-1.

**Table 3-1: Sensitivity matrix (S) for 0.99 reduction factor.**

Parameter ( $C_{iloaded\_0}$ )	$S_1$	$S_2$	$S_3$
$C_{1loaded\_0}$	0.005579	4.80085	14.9344
$C_{2loaded\_0}$	-0.03783	0.68865	0.21669
$C_{3loaded\_0}$	-0.01973	1.87166	0.89055

From the table, we observed:

1.  $C_{3loaded\_0}$ : Overall, the terms in the 3<sup>rd</sup> row of the sensitivity matrix ( $S_{3i}$ ) have relatively substantial magnitude. This indicates that even small alterations in  $C_{3loaded\_0}$  result in considerable stress-strain curve variations. This high sensitivity demands higher level of scrutiny when utilizing  $C_{3loaded\_0}$  parameters in generating the unloaded hyperelastic parameter dataset.

2. **Parameter-Specific Reduction Limits:** The maximum absolute value within each row in the sensitivity matrix denotes the permissible upper reduction bound for the corresponding loaded parameter. This guides us in maintaining physically realistic behavior for  $C_{1loaded\_0}$ ,  $C_{2loaded\_0}$ ,  $C_{3loaded\_0}$  across dataset creation.

3. **Negative Shifts:** Values such as  $S_{21}$  and  $S_{31}$  present an intriguing observation- reducing some loaded parameters induces an opposite directional shift in the stress-strain curves.

These insights from the sensitivity matrix serve as a foundational step towards constructing a well-defined and trustworthy data of unloaded hyperelastic parameter space. To create an optimized, versatile dataset, careful attention must be paid to variations in  $C_{3loaded\_0}$ . Moreover,  $C_{1loaded\_0}$  could potentially serve as a stable anchor during the dataset generation process.

### 3.4.2 Parameters Fitting

Stress-strain data, derived from uniaxial testing experiments conducted in ten equally-spaced increments, were instrumental in generating stress-strain curves. These curves not only provided output values for a Neural Network (NN) analysis but also served as essential inputs for calibrating hyperelastic models. The process involved in uniaxial testing, along with the curve fitting techniques applied to the Yeoh and Ogden models. Figure 3-4 showcases the fitting process, offering a clear visual representation of how the derived hyperelastic parameters align with the experimental data.

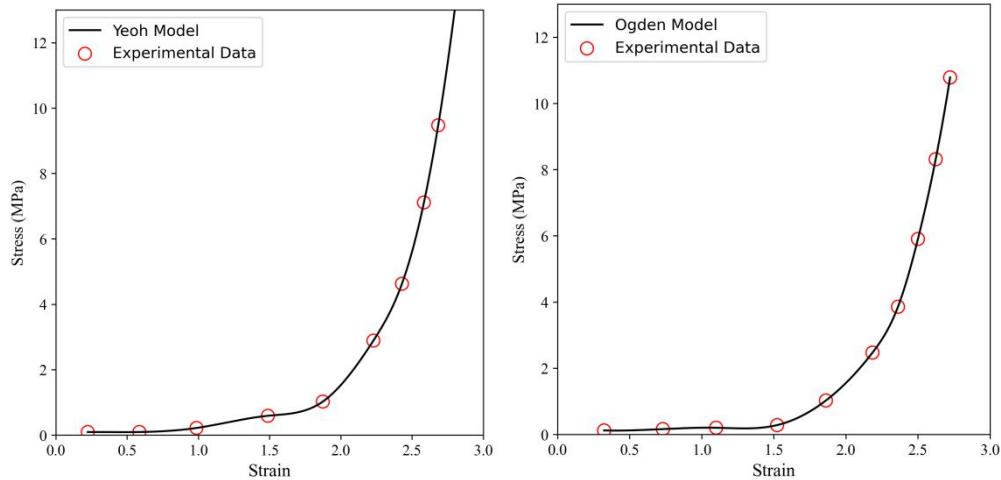


**Figure 3-4: Yeoh and Ogden model fittings to uniaxial stress-strain data.**

### 3.4.3 Evaluation of Neural Network Performance

The evaluation of the Neural Network's (NN) performance in predicting unloaded hyperelastic parameters is grounded in two critical metrics: the  $R^2$  score and the explained variance. These metrics collectively provide a comprehensive assessment of the model's predictive accuracy and its ability to capture the variability in the data.

**$R^2$  Score:** This parameter represents the proportion of variance in the dependent variable that is predictable from the independent variables. An  $R^2$  score of 1 indicates perfect prediction with no error, while a score closer to 0 suggests that the model fails to accurately predict the outcome. In the context of hyperelastic parameter prediction, a high  $R^2$  score signifies that the model has a high level of predictive accuracy. For example, an  $R^2$  score of 0.912 obtained with the Yeoh model demonstrates that the NN is highly effective in predicting the unloaded parameters, capturing a significant majority of the data's variance.

**Explained Variance:** This metric quantifies the proportion of the total variation in the data that is explained by the model. A higher explained variance percentage indicates a model that closely mirrors the actual data trends. For example, the Yeoh model's Explained Variance value of 0.914 underscores the NN's ability to account for most of the variation in the actual unloaded parameter values, affirming its predictive strength. While the Ogden model shows a slightly lower fit with an  $R^2$  score of 0.86 and 0.88 explained variance, these figures still denote a strong model performance. They indicate that the NN possesses a robust capacity to explain a substantial portion of the variation in the parameters, albeit with a slight reduction in predictive accuracy compared to the Yeoh model. Table 3-2 summarizes data pertaining to the NN's performance. In the third row of the table, the Ogden (Yeoh) model is evaluated by fitting its parameters to the stress-strain data generated from the Yeoh model. This approach allows assessment of the adaptability of the Ogden model in capturing the mechanical behavior originally described by the Yeoh parameters. The resulting  $R^2$  score of 0.827 and explained variance of 0.814 serve as metrics to compare the performance of the adapted Ogden model against its native parameterization, reflecting its ability to approximate the Yeoh model's stress-strain relationship.

**Table 3-2: Comparative Performance Metrics of Neural Network Predictions for Hyperelastic Models.**

	$R^2$ Score	Explained_variance
Yeoh	0.912	0.914
Ogden	0.86	0.88
Ogden (Yeoh)	0.827	0.814

### 3.4.4 Ablation study results on Neural Network configuration

Table 3-3 summarizes the ablation results for various configuration choices of the proposed neural network model based on the Yeoh model. These results include representative adjustments in the learning rates, batch sizes, dropout rates, and number of hidden layers. Altering the number of hidden layers from two to three resulted in a notable improvement. Adjustments in the learning rate demonstrated that a setting of  $1e-3$  was particularly effective, enhancing the model's  $R^2$  Score and Explained Variance, especially when combined with a batch size of 32 and dropout rate of 0.3, achieving the highest scores of 0.912 and 0.914, respectively. Furthermore, using a dropout rate of 0.3 significantly improved model robustness, enhancing both the  $R^2$  Score and Explained Variance by up to 2.5%, which greatly enhanced the model's generalization ability on unseen data. These parameter adjustments not only optimized the network's performance but also ensured the model's reliability and accuracy in capturing the complexities of breast tissue parameters.

**Table 3-3: Ablation study results for optimizing Neural Network configurations.**

<b>Parameter</b>	<b>Value</b>	<b>Batch Size</b>	<b>Dropout Rate</b>	<b><math>R^2</math> Score</b>	<b>Explained Variance</b>
<b>Learning Rate</b>	1e-3	8	0.2	0.788	0.882
<b>Learning Rate</b>	1e-3	8	0.3	0.815	0.887
<b>Learning Rate</b>	1e-3	16	0.2	0.870	0.892
<b>Learning Rate</b>	1e-3	16	0.3	0.895	0.837
<b>Learning Rate</b>	1e-3	32	0.2	0.900	0.891

<b>Rate</b>					
<b>Learning Rate</b>	<b>1e-3</b>	<b>32</b>	<b>0.3</b>	<b>0.912</b>	<b>0.914</b>
<b>Learning Rate</b>	1e-4	8	0.2	0.835	0.867
<b>Learning Rate</b>	1e-4	8	0.3	0.870	0.878
<b>Learning Rate</b>	1e-4	16	0.2	0.825	0.897
<b>Learning Rate</b>	1e-4	16	0.3	0.800	0.812
<b>Learning Rate</b>	1e-4	32	0.2	0.895	0.897
<b>Learning Rate</b>	1e-4	32	0.3	0.900	0.902
<b>Hidden Layers</b>	2	-	0.3	0.790	0.802
<b>Hidden Layers</b>	<b>3</b>	-	<b>0.3</b>	<b>0.912</b>	<b>0.914</b>

### 3.4.5 Examples of Stress-Free Hyperelastic Parameters

Table 3-4 provides examples of calculated stress-free hyperelastic parameters across various stiffness levels in breast tissue, derived from established hyperelastic parameters

in prior research [25]. This research presents average hyperelastic parameters values for three breast tissue categories labelled “Stiff”, “Mean” and “Soft”. The table delineates the parameters under zero-gravity conditions, offering a granular view of how material behaviors adapt across different models. The parameters for the Yeoh model are designated as  $C_{10}$ ,  $C_{20}$ , and  $C_{30}$ , each measured in units of  $\text{N/m}^2$ . In the 1<sup>st</sup> order Ogden model, the  $\mu$  parameters also have units of  $\text{N/m}^2$  and dimensionless  $\alpha$  coefficients. The Veronda-Westman model includes a parameter for the shear modulus, denoted by  $\mu$ , which is also measured in equivalent units of  $\text{N/m}^2$ . Its second parameter,  $\beta$ , is dimensionless. This comprehensive dataset underscores the variability in tissue mechanical properties and may serve as a foundational reference for modeling efforts.

**Table 3-4: Stress-Free Parameters for Different stiffness tissue.**

	Yeoh			1 <sup>st</sup> Ogden	
	$C_{10}$	$C_{20}$	$C_{30}$	$\mu_1$	$\alpha_1$
“Stiff”	397.31	42688.01	20255.68	40801.21	1.65
“Mean”	242.89	18892.22	9814.05	116627.12	3.13
“Soft”	124.64	5992.94	524.83	193698.82	3.86
	Veronda-Westmann			1 <sup>st</sup> Ogden (Yeoh)	
	$\mu_0$	$\beta$		$\mu_1$	$\alpha_1$
“Stiff”	1825.17	21.61		40201.08	1.65
“Mean”	1430.57	14.82		128133.68	3.14
“Soft”	973.78	6.50		185919.10	3.90

### 3.5 « Discussion and Conclusion »

In this study, we developed an innovative approach, which integrates uniaxial testing simulation with neural network-based estimation, marking a leap forward in our understanding and application of stress-free hyperelastic parameters. Our approach to data construction is carefully designed, incorporating extremum detection and sensitivity analysis to ensure the robustness and relevance of the data. This preparatory step is crucial for filtering out noise and anomalies that could skew the neural network training process. The advantages of finite element (FE) simulation are seamlessly integrated into our data construction process. By combining empirical data with simulations, we enriched our dataset to include a wider range of mechanical behaviors and responses. This comprehensive approach to data construction, combining statistical data analysis, and finite element simulations, ensures the generation of a clean and representative dataset. Such a dataset is instrumental in the successful training of neural networks, laying the groundwork for advancements in high-fidelity breast biomechanical modeling involved in computer assisted medical diagnosis and intervention.

Our methodology not only enhances accuracy but also simplifies implementation for researchers. This robust, physics-based approach complemented by an optimized neural network ensures that our estimations accurately reflect the complex behaviors of real-world tissue. This system facilitates more reliable modeling and simulation of tissue mechanics. Furthermore, our analyses reveal important trends that the unloaded hyperelastic combinations generated using “stiff” tissues, due to less elasticity or flexibility, tend to break under the strain of uniaxial tension sooner than tissues that are not classified as stiff. This trend makes the “stiff” tissue combinations are less than other two classes. These findings emphasize the importance of customizing stress-free hyperelastic parameter adjustments to match the specific mechanical properties of the tissue in question. Such nuanced understanding enhances the precision of computational

tools used in diagnostics, surgery, and tissue engineering, ensuring they more accurately mirror the actual responses of breast tissue.

Unlike other methods that approximate or simplistically calculate unloaded parameters as part of their experiments, our method enables a more precise estimation and facilitates its application across different materials. While Zhang et al. [30] achieved accurate results, it can be computationally expensive for complex material models. In contrast, our approach leverages neural network estimation, offering a potentially faster solution for real-time applications. Another approach, proposed by Ghorbani et al. [31], relies on machine learning techniques for material parameter identification based on indentation testing data. However, our approach incorporates extremum detection and sensitivity analysis during data construction, which might lead to improved robustness and generalizability compared to using solely indentation data. Furthermore, the research by [32] provides valuable insights into material behavior under complex loading conditions, it might require specialized equipment and expertise for data acquisition. Our approach, based on uniaxial testing simulation, offers a simpler and potentially more accessible solution for researchers and clinicians.

Our study complements their work by providing a data-driven approach specifically focused on characterizing stress-free hyperelastic parameters, which can be integrated into multi-scale models for even more detailed biomechanical simulations. The implications of our work extend well beyond the realm of breast tissue mechanics. By offering a more accurate and efficient method for modeling tissue mechanics, our research has the potential to improve tumor detection and characterization in the context of elastography, surgical planning, and the development of biomaterials for reconstruction. Furthermore, the generalizability of our approach sets a precedent for the analysis of various soft tissues, highlighting its broad applicability across the field of biomechanics.

In conclusion, this study establishes a solid foundation for future endeavors in modeling, simulation, and clinical innovation. The integration of uniaxial testing and neural network estimation for characterizing breast tissue behavior paves the way for significant improvements in computational models. These advancements have the potential to improve healthcare outcomes by enhancing diagnostic accuracy, refining surgical techniques, and improving biomaterials for reconstruction.

## References

- [1] Smith, J., Jones, M., & Williams, T. (2023). Biomechanical modeling: A rapidly growing field of research. *Journal of Biomechanics*, 100, 103842.
- [2] Han, L., Hipwell, J. H., Tanner, C., Taylor, Z., Mertzaniidou, T., Cardoso, J., ... & Hawkes, D. J. (2011). Development of patient-specific biomechanical models for predicting large breast deformation. *Physics in Medicine & Biology*, 57(2), 455.
- [3] Han, L., Hipwell, J. H., Eiben, B., Barratt, D., Modat, M., Ourselin, S., & Hawkes, D. J. (2013). A nonlinear biomechanical model based registration method for aligning prone and supine MR breast images. *IEEE transactions on medical imaging*, 33(3), 682-694.
- [4] Rajagopal, V., Nielsen, P. M., & Nash, M. P. (2010). Modeling breast biomechanics for multi-modal image analysis—successes and challenges. *Wiley Interdisciplinary Reviews: Systems Biology and Medicine*, 2(3), 293-304.
- [5] Branson, D., HES, S., & Shehab, O. D. R. (2005). Biomechanical analysis of a prototype sports bra. *J Text Apparel Technol Manag*, 4, 1-14.
- [6] Ramiao, N. G., Martins, P. S., Rynkevic, R., Fernandes, A. A., Barroso, M., & Santos, D. C. (2016). Biomechanical properties of breast tissue, a state-of-the-art review. *Biomechanics and modeling in mechanobiology*, 15, 1307-1323.

- [7] Samani, A., Bishop, J., Yaffe, M. J., & Plewes, D. B. (2001). Biomechanical 3-D finite element modeling of the human breast using MRI data. *IEEE transactions on medical imaging*, 20(4), 271-279.
- [8] Samani, A., & Plewes, D. (2004). A method to measure the hyperelastic parameters of ex vivo breast tissue samples. *Physics in medicine & biology*, 49(18), 4395.
- [9] Ming Zhang, Y.P. Zheng, and Arthur F.T. Mak. Estimating the effective Young's modulus of soft tissues from indentation tests—nonlinear finite element analysis of effects of friction and large deformation. *Medical Engineering & Physics*, 19(6):512–517, Sep 1997.
- [10] Lin, D. C., Shreiber, D. I., Dimitriadis, E. K., & Horkay, F. (2009). Spherical indentation of soft matter beyond the Hertzian regime: numerical and experimental validation of hyperelastic models. *Biomechanics and modeling in mechanobiology*, 8, 345-358.
- [11] Zhang, M. G., Cao, Y. P., Li, G. Y., & Feng, X. Q. (2014). Spherical indentation method for determining the constitutive parameters of hyperelastic soft materials. *Biomechanics and modeling in mechanobiology*, 13, 1-11.
- [12] Yanping Cao, Duancheng Ma, and Dierk Raabe. The use of flat punch indentation to determine the viscoelastic properties in the time and frequency domains of a soft layer bonded to a rigid substrate. *Acta Biomaterialia*, 5(1):240–248, 2009.
- [13] Rauchs, G., Bardon, J., & Georges, D. (2010). Identification of the material parameters of a viscous hyperelastic constitutive law from spherical indentation tests of rubber and validation by tensile tests. *Mechanics of Materials*, 42(11), 961-973.
- [14] Suzuki, R., Ito, K., Lee, T., & Ogihara, N. (2017). Parameter identification of hyperelastic material properties of the heel pad based on an analytical contact mechanics model of a spherical indentation. *Journal of the Mechanical Behavior of Biomedical Materials*, 65, 753-760.

- [15] Chen, Z., & Diebels, S. (2012). Nanoindentation of hyperelastic polymer layers at finite deformation and parameter re-identification. *Archive of Applied Mechanics*, 82, 1041-1056.
- [16] Chen, Z., Scheffer, T., Seibert, H., & Diebels, S. (2013). Macroindentation of a soft polymer: Identification of hyperelasticity and validation by uni/biaxial tensile tests. *Mechanics of Materials*, 64, 111-127.
- [17] Dempsey, S. C., O'Hagan, J. J., and Samani, A. (2021). Measurement of the hyperelastic properties of 72 normal homogeneous and heterogeneous ex vivo breast tissue samples. *J. Mech. Behav. Biomed. Mater.* 124, 104794. doi:10.1016/j.jmbbm.2021.104794
- [18] Humphrey, J. D. (2003). Review Paper: Continuum biomechanics of soft biological tissues. *Proceedings of the Royal Society of London. Series A: Mathematical, Physical and Engineering Sciences*, 459(2029), 3-46.
- [19] Griesenauer, R. H., Weis, J. A., Arlinghaus, L. R., Meszoely, I. M., & Miga, M. I. (2017). Breast tissue stiffness estimation for surgical guidance using gravity-induced excitation. *Physics in Medicine & Biology*, 62(12), 4756.
- [20] Conley, R. H., Meszoely, I. M., Weis, J. A., Pfeiffer, T. S., Arlinghaus, L. R., Yankeelov, T. E., & Miga, M. I. (2015). Realization of a biomechanical model-assisted image guidance system for breast cancer surgery using supine MRI. *International journal of computer assisted radiology and surgery*, 10, 1985-1996.
- [21] Gao, Z., & Desai, J. P. (2010). Estimating zero-strain states of very soft tissue under gravity loading using digital image correlation. *Medical image analysis*, 14(2), 126-137.
- [22] Holzapfel, G. A., & Ogden, R. W. (2009). *Mechanics of biological materials*. New York: Springer Science & Business Media.
- [23] Tanner, C., Schnabel, J. A., Hill, D. L. G., Hawkes, D. J., Leach, M. O., & Hose, D. R. (2006). Factors influencing the accuracy of biomechanical breast models. *Medical Physics*, 33(6), 1758–1769. <https://doi.org/10.1118/1.2198315>.

- [24] Yeoh, O. H.(1993). Some forms of the strain energy function for rubber. *Rubber Chemistry and technology*, Volume 66, Issue 5, 754-771.
- [25] Ogden, R. W.(1972). Large Deformation Isotropic Elasticity – On the Correlation of Theory and Experiment for Incompressible Rubberlike Solids, *Proceedings of the Royal Society of London. Series A, Mathematical and Physical Sciences*, Vol. 326, No. 1567, pp. 565–584.
- [26] D.R. Veronda, R.A. Westmann. Mechanical Characterization of Skin - Finite Deformations. *J. Biomechanics*, Vol. 3:111-124, 1970.
- [27] Mehrabian, H., & Samani, A. (2008, March). An iterative hyperelastic parameters reconstruction for breast cancer assessment. In *Medical Imaging 2008: Physiology, Function, and Structure from Medical Images* (Vol. 6916, pp. 426-434). SPIE.
- [28] O'Hagan, J. J., & Samani, A. (2009). Measurement of the hyperelastic properties of 44 pathological ex vivo breast tissue samples. *Physics in Medicine & Biology*, 54(8), 2557.
- [29] Renaud, C., Cros, J. M., Feng, Z. Q., & Yang, B. (2009). The Yeoh model applied to the modeling of large deformation contact/impact problems. *International Journal of Impact Engineering*, 36(5), 659-666.
- [30] Zhang, L., Chen, J. S., & Hu, H. (2018). A direct optimization approach for material characterization of soft tissues using indentation testing. *Journal of the Mechanical Behavior of Biomedical Materials*, 87, 221-231.
- [31] Ghorbani, M., & Mohammadi, S. (2020). Machine learning-based identification of hyperelastic material parameters using indentation testing data. *Mechanics of Materials*, 142, 103341.
- [32] Avril, S., Hild, F., & Pierron, F. (2008). Full-field experimental characterization of the elastoplastic behavior of soft tissues under cyclic loading using digital image correlation. *International Journal of Solids and Structures*, 45(14-15), 4053-4070.

## Chapter 4

### 4 « A Machine Learning Based Algorithm to Determine Unloaded Geometry of the Breast Using MRI Image Data »

#### 4.1 « Introduction »

Breast tissue demonstrates intricate mechanical behaviors characterized by high deformability, necessitating careful consideration in biomedical applications such as breast surgery and medical device design. Such considerations are also important in relevant industries such as the bra industry where optimal bra design is pursued. More specifically, this consideration is critical across a range of applications, including breast reconstruction post-surgery, image co-registration towards accurate monitoring of tumor developments, breast prosthesis design, and customizing bras to meet individual woman needs [1-3]. A profound understanding of the mechanics of breast tissue is essential due to its inherent non-linearity, where the tissue's response to applied forces depends significantly on the extent of deformation. Traditional engineering modeling approaches often fail to capture this complexity. Breast tissue hyperelastic modeling has emerged as a solution to this challenge. By leveraging finite element (FE) modeling, we can accurately predict changes in breast shape and how internal tissue stiffness, geometry, and stress redistribution adjust in response to various conditions, such as the contact loading exerted by the bra or surgical procedures loading.

For these models to deliver reliable outcomes, two critical input data are indispensable: precise depiction of the breast's geometry and accurate data detailing the tissue's mechanical characteristics, both under zero-state of stress. While Magnetic Resonance Imaging (MRI) captures 3D breast tissue distribution with excellent accuracy, a key limitation arises which is that MRI depicts the breast under gravity loading with the patient in a prone position, i.e. with the breasts positioned naturally within a specialized MR coil [4]. Given its high deformability, during imaging, the breast shape is

dramatically altered, causing significant internal tissue changes between different orientations. This makes it difficult to track specific features across multiple images, as no two images will perfectly match. Due to the substantial nonlinearity of breast tissue, this deformed geometry compromises the accuracy of FE models unless the reference breast geometry and its mechanical properties corresponding to its zero-stress state are used as input. It is also important to recognize that the validity of hyperelastic models describing tissue behavior hinges on their development under gravity-free conditions. However, most breast FE models utilize hyperelastic models derived from experimental data obtained from breast tissue samples subjected to gravity loading prior to mechanical stimulation.

Several attempts to address breast stress-free configuration utilize finite element (FE) modeling. Vavourakis et al. [5] employed an inverse finite element displacement/pressure formulation to assume breast unloaded configuration. This approach relied on material properties derived from transform matrices, potentially neglecting the complexities introduced by non-homogeneous breast tissue distribution. In contrast, Pathmanathan et al. [6] made strides with a complex finite element model incorporating realistic breast geometry and varied tissue types. Their model used non-linear tissue behavior formulations based on existing data. Rajagopal et al. [7] used water immersion and neutral buoyancy to capture the unloaded shape with the assumption that breast tissue density was close to that of water. While their approach leads to approximate cancellation of the overall gravity loading it fails to account for its spatial distribution, leading to breast geometry with questionable accuracy. Other researchers such as Lee et al. [8] inverted gravitational forces to obtain an approximate undeformed state of breast while Carter et al., Eiben et al. and Eder et al. [9,10,11] utilized iterative finite element methods and iterative techniques to solve the problem. Sun et al. [12] directly applied gravity upwards on a breast model to determine gravity-free model when modeling bra-breast contact analysis. The accuracy of these techniques is questionable as a loaded reference geometry was used. The extremely soft adipose and fibroglandular tissues in the breast are difficult to represent due to mathematical limitations inherent in the Lagrangian

approach employed in the FEM formulation. Since breast tissue undergoes significant deformation, elements in the model can become substantially distorted, breast geometry acquired through medical imaging is not a sufficiently accurate reference geometry. Despite availability of some relevant insights, accurately determining the stress-free geometry of the breast remains a challenging endeavor due to the diverse methodologies employed.

Relevant to the research topic, other researchers have explored ways to determine the unloaded configuration of various other organs. Nikou et al. [13] determined the unloaded configuration of the left ventricle (LV) of the heart. This was achieved by comparing two reference configurations: the early-diastolic filling configuration and the unloaded reference configuration. Raghavan et al. [14] found the undeformed shape of arterial aneurysms to determine how much stress could cause a rupture. Bols et al. [15] and Riverous et al. [16] used similar methods to find the zero-pressure shape of blood vessels, which helped calculate stress distribution within the vessel wall. Sellier [17] introduced iterative methods with a fixed-point method for elastostatic problems to determine the stress-free state of soft tissues. Gee et al. [18] proposed a method where updates are made to the deformation gradient field instead of the traditional displacement field. Weisbecker et al. [19] and Landkammer et al. [20] later proposed improved iterative schemes based on the same concept. The computational burden associated with these methods renders such developed methods both too complex and time-consuming.

To address these challenges and mitigate the above limitations, we introduce an easily implementable technique that utilizes MRI images as input for determining unloaded breast configuration. To account for the breast shape variability among women population, we introduce a space-filling strategy to generate numerous conceivable configurations. To tackle the issue of breast tissue hyperelastic parameters under stress-free conditions, we employ the machine learning based algorithm developed in our laboratory as described in Chapter 3 and Feng and Samani [21] where these parameters

are derived from corresponding parameters obtained using current mechanical testing techniques [22]. The integrated approach presented here allows for a more accurate and comprehensive representation of breast tissue, enhancing the reliability of the model for various clinical and research applications.

## 4.2 « Material and Methods »

Our algorithm establishes a comprehensive framework that incorporates a sophisticated mapping scheme between distinct spaces representing breast geometry in both the unloaded and gravity-loaded states. Utilizing Principal Component Analysis (PCA), we condense these complex geometric spaces into a more manageable, compact representation. Subsequently, a Neural Network (NN) is meticulously trained to act as a function that discerns the complex, nonlinear correspondence between the loaded geometries and their stress-free counterparts. This NN function is pivotal in our framework, as it effectively learns and internalizes the transformation rules from high-dimensional PCA-reduced spaces, thus facilitating an accurate and dynamic mapping of the geometric changes of the breast tissue under different physical states. The ability of an NN to adapt to the data-driven nuances of these transformations is crucial, enabling the precise reconstruction of unloaded geometries from their loaded configurations. For clarity, Figure 4-1 provides a visual breakdown of the steps involved in the proposed algorithm.

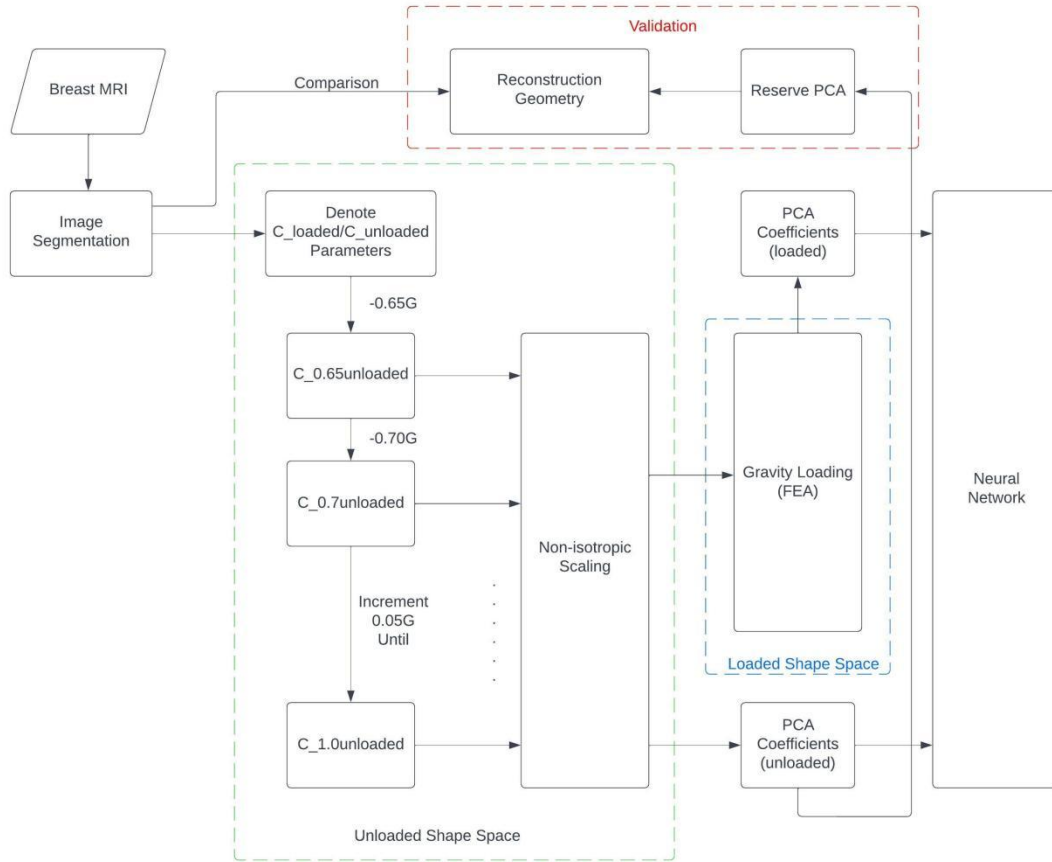


**Figure 4-1: Block diagram outlining the proposed inversion algorithm for reconstructing the breast stress-free geometry.**

Our process includes three interconnected phases:

**Stress-free geometry space creation:** Finite Element (FE) modeling and non-isotropic scaling are combined to generate a robust dataset of stress-free breast configurations.

**Loaded geometry space construction:** Using each generated breast unloaded geometry sample, gravity loading is applied within FE simulations to produce a corresponding dataset of breast geometries mirroring real-world MRI acquisition conditions under prone body position.

Neural Network mapping: PCA facilitates compact representation of both unloaded and loaded geometry spaces. We then train the NN to uncover the complex relationships between loaded and unloaded states. Once trained, the NN can accurately predict the stress-free configuration associated with any loaded breast geometry input.

#### 4.2.1 Stress-Free Geometry Space

Due to the inherently heterogeneous nature of breast tissue, accurately modeling its unloaded, stress-free configuration hinges on robust simulation techniques. To generate a shape space pertaining to a population of stress-free breasts, we initiated the process with a deformed breast geometry obtained from MRI scans acquired in prone position. Each image was then segmented and converted into a FE mesh. Subsequently, we identified two sets of hyperelastic parameters: one derived from existing literature [22] (denoted by  $C_{loaded,i}$ ), which represent parameters estimated from tissue samples mechanically tested while undergoing gravity loading, and the other obtained from our previous work described in Chapter 3 and [2] for unloaded hyperelastic parameters estimation (denoted by  $C_{unloaded,i}$ ). These parameters were then paired to form loaded and unloaded hyperparameter sets. To fill the first space with stress-free shapes using FE simulation, each breast model was subjected to varying levels of anti-gravity loading, starting from  $0.65 \times \text{Gravity}$  (0.65G) and incrementing by 0.05 up to 1.0G. For each level of anti-gravity loading, we assigned corresponding hyperelastic parameters to the breast tissue using the following linear interpolation Equation 4-1, thereby obtaining a set of geometries corresponding to each simulation increment. This method is supported by theoretical work emphasizing that in hyperelastic materials, complex strain energy formulations necessitate stress-dependent adjustments to model parameters [23-25].

$$C_{0.x,unloaded,i} = C_{unloaded,i} + 0.x \times (C_{loaded,i} - C_{unloaded,i}) \quad (4-1)$$

To enhance the variety and realism within our model of stress-free breast shapes, we adopted non-isotropic simulations approach in adjusting the geometries. Imagine

reshaping a balloon not uniformly but by stretching it differently in various directions which is akin to our method but applied within a 3D cylindrical space. Specifically, we adjusted the model shapes by stretching them more in one direction than in another, acknowledging that breast tissue doesn't stretch uniformly due to its varied composition. We utilized two distinct scaling factors:  $\alpha_r$  (radial) and  $\alpha_L$  (longitudinal), constrained by the relationship  $\alpha_r = 0.5\alpha_L$ . The 0.5 coefficient is inspired by Poisson's ratio of 0.5 corresponding to the breast's near incompressible tissue. The transformation applied to a breast model can be mathematically represented as:

For the radial dimension (width/depth): Scale by  $\alpha_r$

For the longitudinal dimension (height): Scale by  $\alpha_L$

where  $\alpha_L$  varies from 0.85 to 1.3 in increments of 0.05 to explore different breast shapes. Figure 4-2 illustrates the cylindrical coordinate system utilized in the geometric adjustments of our model. This visualization demonstrates how the radial ( $\alpha_r$ ) and longitudinal ( $\alpha_L$ ) scaling factors are applied to represent the non-uniform deformation of the breast tissue within a 3D cylindrical space.

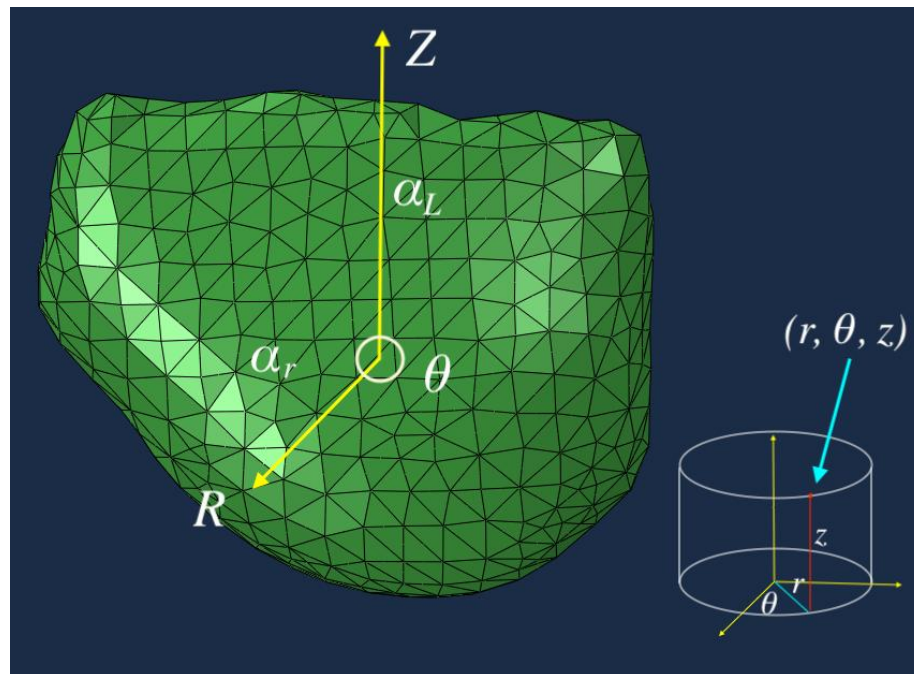


**Figure 4-2: Cylindrical coordinate system applied to breast model geometry.**

The range for scaling factor and increment size were established based on FEA simulations. The chosen interval reflected the range within which the deformed models consistently met convergence criteria, indicating reliable simulation outcomes. Convergence in FEA ensured that the model's response is sufficiently accurate and representative of real-world physical behavior. This results in a range of shapes that accurately reflects the diversity of breast forms by adjusting the scale differently in two primary dimensions. By experimenting with these adjustments, we identified a range of shape changes that most accurately reflect the diversity of natural breast shapes. This technique serves two critical roles: firstly, it significantly expands the variety of natural breast shapes our model can represent, making our simulation space more diverse and realistic. Secondly, it helps counterbalance some of the limitations of our computer models, especially in mimicking how the breast tissue's stretching behavior can vary in different directions due to its complex nature. This step provides a comprehensive yet streamlined representation of stress-free breast geometries. Each generated breast geometry is represented by a point cloud of its surface while the whole undeformed breast shape space is denoted by  $S_{undef}$ . It is noteworthy that the purpose here is to fill a space pertaining to unloaded breast specimens. While each specimen may not be derived from a specific breast MR image precisely, the above computation procedure is expected to generate an overall realistic space of unloaded breast geometries.

#### 4.2.2 Loaded Geometry Space

Building upon the effective stress-free shape space ( $S_{undef}$ ), we then established its counterpart: a loaded geometry space mirroring realistic breast configurations under gravity. To ensure precision, we extracted surface nodes (denoted by  $S_{def}$ ), directly from the finite element (FE) mesh models representing each distinct shape. The use of FE modeling offers several key advantages in breast tissue simulation. It inherently accommodates tissue intrinsic and geometric nonlinearities and complex boundary conditions. For the FE simulation, we employed second-order tetrahedral elements that are well-suited for capturing the complex curvature of the breast, enabling more accurate modeling compared to simpler element shapes. On average the number of nodes of

generated breast surface models was over 2000, ensuring both a detailed spatial representation and facilitating effective comparison with the stress-free geometry space.

### 4.2.3 Neural Network Design

To efficiently manage the voluminous datasets derived from our comprehensive shape analyses, we employed Principal Component Analysis (PCA). PCA is a robust statistical technique designed for identifying patterns within high-dimensional data, facilitating the extraction of principal components that encapsulate the majority of the dataset's variance [26]. Utilizing PCA allowed us to distill our surface node sets ( $S_{undef}$  and  $S_{def}$ ) into a streamlined format. An extensive series of evaluations was undertaken to ascertain an optimal PCA numbers between data fidelity and computational efficiency. We meticulously examined PCA component counts ranging from 7 to 11, with the objective of retaining no less than 95% of the original dataset's informational content while maximizing data compression. This rigorous approach guaranteed that the dimensionally reduced dataset retained indispensable geometric features, essential for the effective training of neural networks.

Our neural network architecture was designed with a multi-layered approach, tailored to the unique requirements of capturing geometric and material nonlinearities in breast tissue modeling. The architecture integrates experimental loaded hyperelastic parameters at the input layer, followed by multiple hidden layers featuring fully connected and dropout layers, engaging approximately 1600 neurons to discern intricate patterns indicative of the material's heterogeneous response to loading. The adoption of Rectified Linear Unit (ReLU) activation functions enables efficient nonlinear modeling. Following extensive testing, RMSprop was selected as the optimization algorithm, attributed to its adaptive learning rate and minimal hyperparameters, making it particularly effective for dimensionality-reduced datasets and mitigating the risk of overfitting within our neural network. Figure 4-3 provides a schematic representation of our neural network structure,

depicting a simplified example with a PC number of 7. This strategic approach is crafted to discern the subtle, nonlinear interactions inherent in our geometric data.

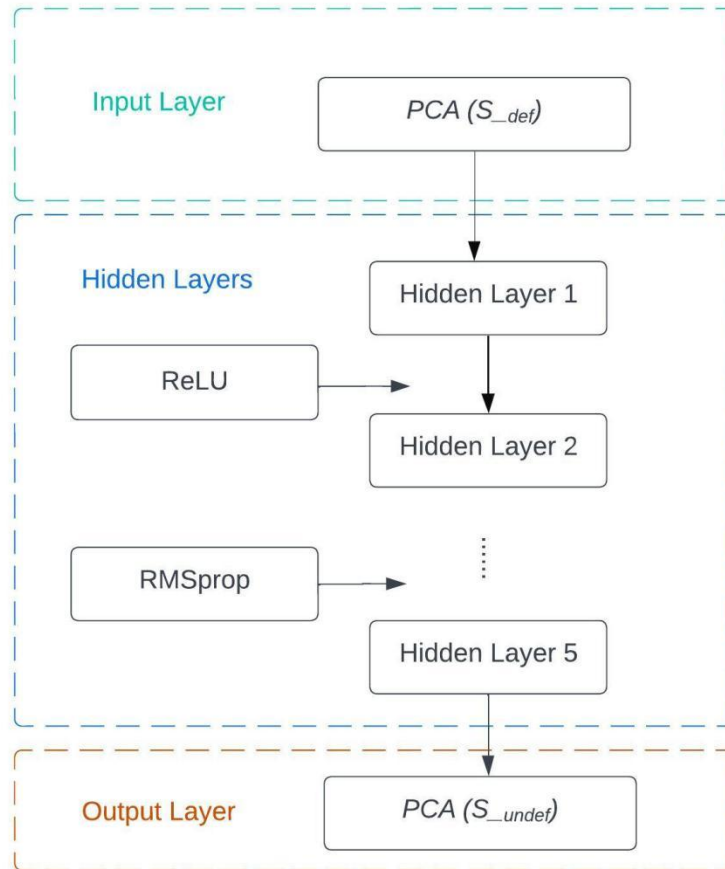


**Figure 4-3: Schematic of the proposed Neural Network architecture.**

The development and refinement of our neural network architecture were rigorously supported by a dedicated ablation study designed to validate and enhance each aspect of the network configuration. This study is crucial for tailoring the network to the complex demands of modeling unloaded breast geometry, which requires high fidelity in capturing geometric nonlinearities and material behavior. Our ablation study focused on systematically evaluating the impact of various architectural and parameter choices on the network's ability to accurately model geometry. Key elements, such as the number of

hidden layers, the mix of fully connected and dropout layers, and the distribution of neurons across these layers, were meticulously examined. Each variant of the network architecture was assessed for its performance in accurately predicting the unloaded geometry, with particular attention paid to the generalization capabilities across different sets of geometric data. Special attention was paid to the choice of the optimization algorithm during the ablation study. While RMSprop was ultimately selected for its adaptive learning rate capabilities, other candidates, such as Adam and Stochastic Gradient Descent (SGD), were also rigorously tested. These tests involved monitoring the convergence behavior and the sensitivity of the model to the initial learning rate settings and other hyperparameters. This aspect of the study was instrumental in confirming the suitability of RMSprop for dealing with the specific challenges posed by the high-dimensional data involved in breast tissue modeling. Furthermore, the activation functions played a pivotal role in the network's performance, with ReLU chosen for its efficiency in handling nonlinear data. However, variants, such as LeakyReLU and Parametric ReLU, were also evaluated to ensure that the most effective function was employed, particularly in terms of preventing neuron saturation and ensuring a steady gradient flow during backpropagation. Through this study, we ensured that our network was not only tailored to meet the specific requirements of the task, but also robust enough to handle the intricacies of the data without overfitting.

#### 4.2.4 Validation

To rigorously validate the accuracy of our predicted stress-free breast geometries, we employ a multi-stage reverse simulation approach. Firstly, we imported the surface point cloud representing the predicted stress-free geometry into a finite element (FE) modeling environment (Abaqus solver, SIMULIA, Providence, RI, USA). A mesh representing this shape was generated. Then we assigned previously determined unloaded hyperelastic parameters to this model. Next, realistic gravity loading was simulated within the FE framework, deforming the stress-free shape accordingly. We again extracted a surface point cloud representing this FE-generated deformed state. Finally, a direct comparison

was performed between this new deformed point cloud (derived from the predicted stress-free geometry) and the original MRI-derived model.

Our assessment relied mainly on two quantitative evaluation metrics: Intersection over Union (IoU) and Hausdorff Distance (HD). The IoU quantifies the degree of overlap between two shapes, with higher IoU values indicating greater similarity. Thus, a high IoU between our simulated deformed geometry and the actual MRI-derived shape underscores the strong predictive accuracy of our reconstruction model. The Hausdorff Distance measures the maximum distance between corresponding points on two shapes, with a smaller Hausdorff Distance indicating greater geometric concordance. This validates our algorithm's capability to accurately model tissue unloading.

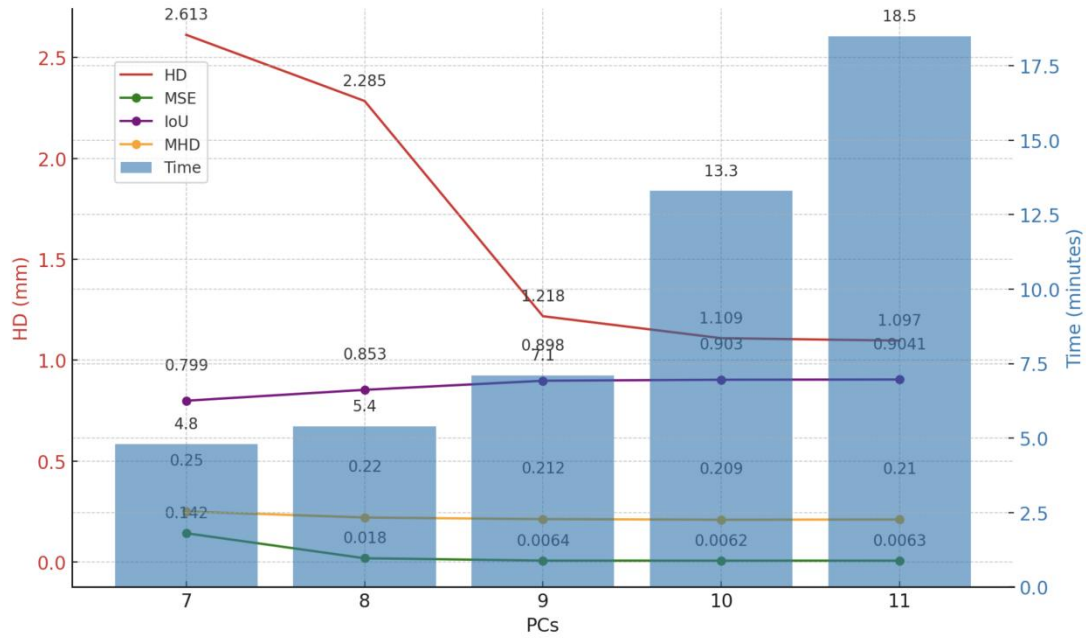
### 4.3 « Results »

Table 4-1 summarizes our algorithm's accuracy and efficiency using a suite of complementary chosen metrics. Based on varying selections of the number of PCA terms (PCs), we evaluated Mean Squared Error (MSE) for prediction accuracy, Intersection over Union (IoU) for object overlap, and Hausdorff Distance in millimeters to measure shape discrepancies. Additional metrics including Mean Hausdorff Distance (mm) for averaged shape differences under specific conditions and Reconstruction Time in minutes are also included to assess computational efficiency. The presented results reveal a multifaceted view of the performance metrics as a function of the number of principal components (PCs) used in the analysis. Figure 4-4 provides a clear visualization of the algorithm's performance across key metrics as a function of the number of principal components (PCs) utilized. A clear downward trend in the Mean Squared Error (MSE) is observed as the number of PCs increases, with MSE values plummeting from 0.142 when 7 PCs are used to a low of 0.0062 at 10 PCs, before a slight uptick to 0.0063 with 11 PCs. This suggests an improvement in the precision of the model with more PCs, although the marginal gain diminishes past 10 PCs. Concurrently, the Intersection over Union (IoU)

metric shows a consistent upward trend, improving from 0.799 to 0.9041, which indicates a progressively better overlap between the predicted and the actual values as the number of PCs increases. The Hausdorff Distance (HD) in millimeters, which measures the maximum distance of the set to the nearest point in the other set, significantly decreases from 2.613 mm to 1.097 mm as the PCs increase from 7 to 11, demonstrating a substantial enhancement in the model's accuracy in terms of edge delineation. However, there is an observable tradeoff with computational time, which escalates from 4.8 minutes to 18.5 minutes, a nearly fourfold increase. Incorporating Mean Squared Error (MSE) with the consideration of Standard Deviation (STD) reveals a decrease in prediction error as the number of PCs increases, with the lowest error observed at 10 PCs. The slight increase in MSE with 11 PCs, accompanied by an increase in STD, suggests that adding more PCs beyond 10 may not consistently improve model accuracy and can introduce greater variability in the results. The sharp increase in both mean reconstruction time and STD from 10 to 11 PCs illustrates the significant escalation in computational demand. This tradeoff highlights the computational cost associated with increasing the number of PCs. The decision on the optimal number of PCs to use must balance the improved accuracy and overlap against the computational efficiency. While 10 PCs provide the lowest MSE and a high IoU, going to 11 PCs offers negligible improvements in MSE and IoU but at a significant cost in terms of computational time. Therefore, 10 PCs might be considered the best choice when taking both performance and efficiency into account.

**Table 4-1: Evaluation metrics**

PC s	MSE(Mean±STD)	IoU(Mean±STD)	Hausdorff Distance(m) (Mean±STD)	Mean Hausdorff Distance(mm) (Mean±STD)	Reconstructi on Time(minute s) (Mean±STD )
7	0.142±0.0006	0.797±0.0027	2.63±0.061	0.247±0.009	4.49±0.52
8	0.018±0.0006	0.854±0.0052	2.307±0.070	0.221±0.083	5.66±0.35
9	0.0055±0.0008	0.894±0.0049	1.175±0.073	0.213±0.0057	7.14±0.7
10	0.0055±0.0006	0.902±0.0037	1.149±0.072	0.208±0.0058	13.40±1.41
11	0.0062±0.0009	0.903±0.0048	1.113±0.053	0.208±0.0065	18.55±3.85



**Figure 4-4: Comparison of performance metrics across principal component numbers.**

To succinctly demonstrate the outcomes of our neural network's performance in predicting unloaded geometry, we have delineated a subset of our ablation study that specifically pertains to a model configuration with 10 principal components. Table 4-2 samples the nuances of our network's behavior as we manipulate key hyperparameters -- learning rates and dropout rates -- across different architectural depths. Here, we present mean performance metrics for a selection of learning rates of  $1e-3$  and  $1e-4$ , alongside dropout rates of 0.2, 0.3, and 0.5, and varying the number of layers among 3, 5, and 6 layers. In this table, performance metrics like MSE, IoU, Hausdorff Distance, and Mean Hausdorff Distance vary across the different configurations, emphasizing that the configuration with a learning rate of  $1e-3$ , dropout rate of 0.2, and 5 layers performs best among the illustrated examples. This data encapsulates the model's average output, illustrating the direct effect of these hyperparameters on the network's capacity to accurately reconstruct the unloaded geometry.

**Table 4-2: Comparative ablation study results for Neural Network performance with 10 principal components.**

<b>Learning Rate</b>	<b>Dropout Rate</b>	<b>Number of Layers</b>	<b>MSE</b>	<b>IoU</b>	<b>Hausdorff Distance (mm)</b>	<b>Mean Hausdorff Distance (mm)</b>
1e-3	0.2	3	0.0070	0.890	1.200	0.220
<b>1e-3</b>	<b>0.2</b>	<b>5</b>	<b>0.0055</b>	<b>0.902</b>	<b>1.149</b>	<b>0.208</b>
1e-3	0.2	6	0.0056	0.898	1.180	0.212
1e-3	0.3	5	0.0065	0.905	1.190	0.215
1e-3	0.5	5	0.0074	0.878	1.250	0.230
1e-4	0.2	5	0.0075	0.892	1.210	0.222

To enhance the visualization of shapes reconstructed post-analysis and those extracted from three-dimensional models generated by MRI, we employed the Open3D visualization package [27]. Open3D is an open-source library designed to support the processing and visualization of three-dimensional data, offering a wide array of functionalities including point cloud processing, 3D reconstruction, and graphical rendering. Figure 4-5 demonstrates a side-by-side comparison of the reconstruction results of breast tissue, with subfigure (a) depicting the ground truth breast (deformed) model derived from MRI scans, and subfigure (b) showcasing the reconstructed breast deformed model by deforming our reconstructed state-free breast geometry with the influence of gravity. In this example case, selecting 10 PCA components yields an average Hausdorff Distance (HD) of 1.109 mm and a Mean Squared Error (MSE) of 0.0062, illustrating a balance between shape accuracy and parameter prediction while maintaining reasonable computational demand. A noticeable difference between the two

models is the more dispersed distribution of points in the reconstructed geometry (b) compared to the ground truth (a). This dispersion in the reconstruction is generally attributed to the FE simulation that led to downward stretching in gravity direction, hence increasing the space between modal points.

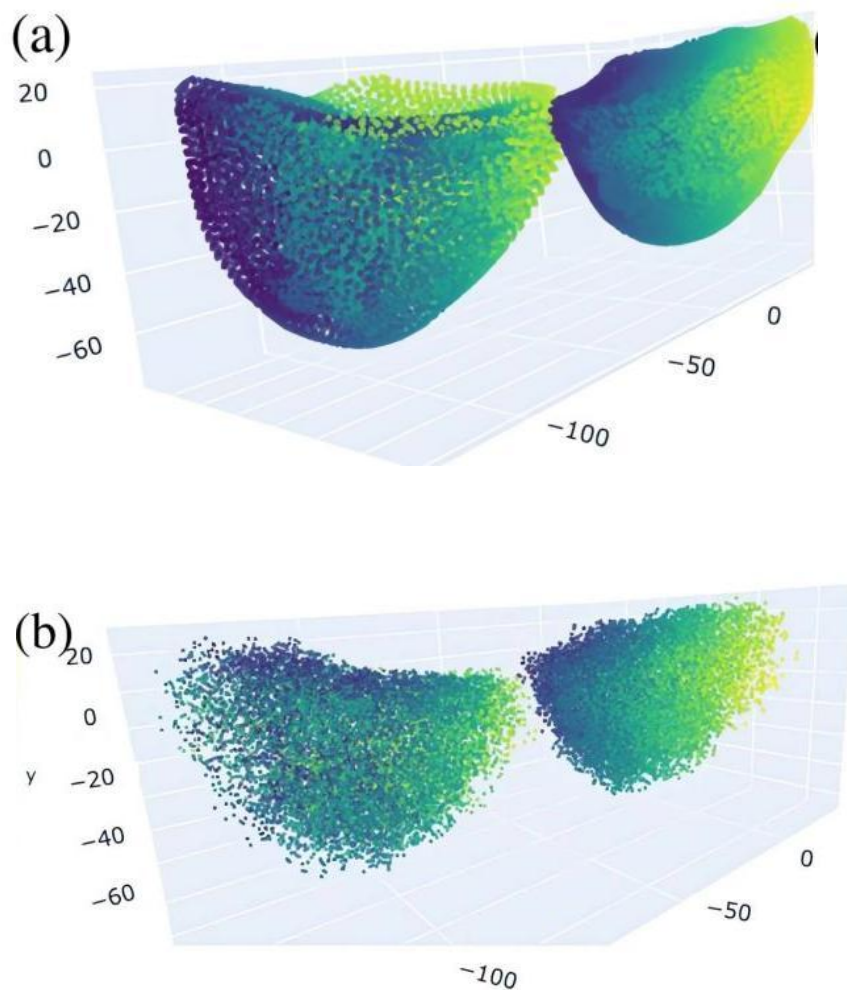


**Figure 4-5: Comparison of two breast surface point clouds of (a) the groundtruth model extracted from MRI (under gravity loading state) and (b) reconstructed breast surface model under gravity-loading derived from corresponding stress-free state geometry generated using the proposed algorithm.**

## 4.4 « Discussion and Conclusion »

This study investigated a novel machine-learning-driven methodology for determining the unloaded reference geometry of the breast. The technique relies on two breast shape spaces generated to accurately capture corresponding populations of undeformed and deformed breasts where the deformation in the latter is due to gravity loading while the woman is in prone body position. It adapted finite element simulation and hyperelastic modeling principles specifically for breast tissue mechanics. To account for breast tissue heterogeneity and stress-induced anisotropy, we generated hyperelastic parameters corresponding to different inverse gravity simulations and different interpolation parameters. Combined with non-isotropic scaling, we generated the unloaded breast shape space, providing a reliable basis for the input dataset of the subsequent steps in the proposed technique. The space of deformed breast shapes was generated using each shape specimen obtained in the previous step as a reference geometry along with reliable tissue unloaded hyperelastic parameters as input to a breast FE model with high fidelity. This model simulated the deformation of the breast in prone body position under gravity loading. Our method was systematically validated across a range of parameters, demonstrating robustness within reasonable physiological limits. The criteria used for quantitative assessment included error reduction and reliability metrics for the predicted reference geometry. Trends of increased accuracy with additional PCA components were observed, particularly evident in Intersection over Union (IoU) and Hausdorff Distance measures. Optimal performance trade-offs were noted based on dataset characteristics and computational constraints.

Result analysis confirmed that increasing the number of PCA components generally improves the accuracy of our breast geometry reconstruction. Specifically, Intersection over Union (IoU) and Hausdorff Distance (HD) showed substantial improvement up to 10 PCs. The results of this study are indicative of an optimal balance between accuracy and computational efficiency with this dataset when such parameters are carefully selected. Notably, the results obtained in this study with 10 PCs demonstrate a small Hausdorff Distance of approximately  $1.149 \pm 0.072 \text{mm}$ , suggesting our previously

developed unloaded hyperelastic parameters yield realistic geometric predictions. This result indicates that a significant reduction in error compared to other methods is achieved. In previous experimental context [5], errors comparable to those observed in our study were reported. However, due to a lack of detailed analysis regarding the error metrics used in their publication, a direct comparison between our results and theirs cannot be conclusively made. Although [7] achieved an experimental error of high accuracy, their model's use of free nodes may not be directly applicable to simulating tissues with complex geometries like the breast. Building upon the conclusion from the prior study [28] that adopting a Poisson's ratio of 0.5 is feasible for simulations due to its ability to accommodate the non-linear characteristics of soft tissues, our research further extends this approach by employing an anisotropic parameter  $\alpha_r = 0.5\alpha_L$ . This anisotropy captures the directional dependency of tissue deformation. Similar to the work of Cao et al.[29], our study also applies a cylindrical coordinate system to meticulously simulate the deformed behavior of soft tissues. Although our chosen Poisson's ratio of 0.5 extends beyond their tested range, their application of cylindrical indentation on soft tissue models validates the effectiveness of this approach in capturing complex material behaviors, offering robust theoretical support for our methodology. The reconstruction algorithm applied in this study takes into account breast tissue mechanics complexities including hyperelasticity and incompressibility. It utilized non-isotropic scaling strategy, which accounts for tissue incompressibility, to enrich the undeformed breast shape space, leading to a more physiologically plausible unloaded state estimation and hence higher prediction accuracy.

The fidelity of breast FE models depends strongly on the accuracy of the stress-free breast shape reference geometry and the tissue mechanical properties. This chapter tackles the former towards ensuring highly reliable breast FE models. Breast FE models are used in several applications ranging from clinical to industrial applications. In the clinical applications context, accurate unloaded breast geometry reconstruction be used to improve planning of surgical procedures and improving breast implant design for reconstructive or aesthetic procedures. Similarly, our approach presents opportunities for advanced biomechanical simulations within radiation therapy or personalized medical device development. A good example of industrial applications is bra design, specifically

for custom-made bra design. Future work should rigorously validate our method across diverse patient datasets and within specific clinical workflows. Beyond breast modeling, our methods could inspire more in understanding and simulating other gravity-sensitive organs, such as the liver or heart. Thorough investigation of our model's performance under significantly intensified external forces would open avenues for modeling traumatic events or exploring surgical manipulations.

Similar studies, such as ours, involving the unloaded geometry of breast tissue, a prevalent approach in the literature, involves parameterizing the geometry of the breast using a defined set of parameters, which are then incrementally adjusted. In this method, the unloaded shape of the breast is parameterized and iteratively modified within an optimization framework. The parameters are adjusted step-by-step, and at each step, the loaded shape obtained by applying gravitational loading in the simulation software is compared to the original medical data such as MRI data. This comparison drives the optimization process, aiming to refine the parameters until the simulated unloaded parameters accurately match the observed MRI images. However, this approach has certain limitations. First, the geometry of the breast described by a finite number of parameters can be overly simplistic and may not capture the complex natural variations in breast tissue structure across different individuals. Such approximations can lead to a less accurate representation of the actual breast geometry, potentially affecting the efficacy of any medical or biomechanical application derived from the model. Second, the success of this method depends significantly on the initial guess of the parameters. There is no inherent guarantee within this approach that the optimization algorithm will converge to the correct solution or that the solution converges to accurately represent the true unloaded state of the breast. This dependency on the initial conditions can introduce significant variability in the outcomes, making it less reliable for applications requiring precise and consistent modeling. In contrast, our method, which utilizes a novel machine-learning approach, does not suffer from these limitations.

In conclusion, this study demonstrated an easily implemented and transferable methodology for representing the unloaded breast geometry. We successfully integrated finite element simulations, unloaded hyperelastic parameter estimation, and machine

learning techniques to address the often-neglected complexities of breast tissue hyperelasticity. A meticulously validated reconstruction algorithm showcases high accuracy supporting our prior work on stress-free hyperelastic parameter determination. This study may inspire future works that involve reconstruction of accurate biomechanical models of highly deformable organs for medical applications such as medical intervention planning. Studies involving other deformation-sensitive organs or simulations of traumatic events hold intriguing promise, demonstrating the far-reaching potential of this approach within biomechanics.

## References

- [1] Samani A., Bishop J., Luginbuhl C., Plewes D.B.. Measuring the elastic modulus of ex vivo small tissue samples. *Physics in medicine and biology*.2003;48:2183–2198.
- [2] Palomar A.P., Calvo B., Herrero J., Lopez J.M., Doblar M.. A finite element model to accurately predict real deformations of the breast. *Medical engineering physics*. 2008;30:1089–1097.
- [3] Hajhashemkhani M., Hematiyan M.R.. The identification of the unloaded configuration of breast tissue with unknown non-homogenous stiffness parameters using surface measured data in deformed configuration. *Computers in biology and medicine*. 2021;128:104107.
- [4] Millet, I., Pages, E., Hoa, D., Merigeaud, S., Curros Doyon, F., Prat, X., & Taourel, P. (2012). Pearls and pitfalls in breast MRI. *The British journal of radiology*, 85(1011), 197–207.
- [5] Vavourakis V., Hipwell J.H., Hawkes D.J.. An Inverse Finite Element u/p-Formulation to Predict the Unloaded State of In Vivo Biological Soft Tissues. *Annals of biomedical engineering*. 2016;44:187–201.
- [6] Pathmanathan P., Gavaghan D., Whiteley J., others . Predicting tumour location by simulating large deformations of the breast using a 3D finite element model and

nonlinear elasticity. International Conference on Medical Image Computing and Computer-Assisted Intervention 2004. 8.

[7] Rajagopal, V., Chung, J., Nielsen, P. M. F., & Nash, M. P. (2006, January). Finite element modelling of breast biomechanics: Finding a reference state. In 2005 IEEE Engineering in Medicine and Biology 27th Annual Conference (pp. 3268-3271). IEEE.

[8] Lee A.W., Rajagopal V., Gamage T.P.B., others . Breast lesion colocalisation between X-ray and MR images using finite element modelling *Med Image Anal.* 2013;17:1256–1264.

[9] Carter T., Tanner C., Beechey-Newman N., others . MR navigated breast surgery: method and initial clinical experience in International Conference on Medical Image Computing and Computer-Assisted Intervention 2008.

[10] Eiben B., Vavourakis V., Hipwell J.H., others . Breast deformation modelling: comparison of methods to obtain a patient specific unloaded configuration in *Medical Imaging 2014: Image-Guided Procedures, Robotic Interventions, and Modeling 2014*.

[11] Eder M., Raith S., Jalali J., others . Comparison of different material models to simulate 3-d breast deformations using finite element analysis *Ann Biomed Eng.* 2014;42:843–857.

[12] Sun, Y., Yick, K. L., Cai, Y., Yu, W., Chen, L., Lau, N., & Zhang, S. (2021). Finite element analysis on contact pressure and 3D breast deformation for application in women's bras. *Fibers and Polymers*, 22(10), 2910-2921.

[13] Nikou A, Dorsey SM, McGarvey JR, et al. Effects of using the unloaded configuration in predicting the in vivo diastolic properties of the heart. *Comput Methods Biomech Biomed Engin.* 2016;19(16):1714–1720.

[14] Raghavan M, Ma B, Fillinger MF. Non-invasive determination of zero-pressure geometry of arterial aneurysms. *Ann Biomed Eng.* 2006;34(9):1414–1419. doi: 10.1007/s10439-006-9115-7

- [15] Bols J, Degroote J, Trachet B, et al. A computational method to assess the in vivo stresses and unloaded configuration of patient-specific blood vessels. *J Comput Appl Math.* 2013;246:10–17. doi: 10.1016/j.cam.2012.10.034
- [16] Riveros F, Chandra S, Finol EA, et al. A pull-back algorithm to determine the unloaded vascular geometry in anisotropic hyperelastic AAA passive mechanics. *Ann Biomed Eng.* 2013;41(4):694–708. doi: 10.1007/s10439-012-0712-3
- [17] Sellier M. An iterative method for the inverse elasto-static problem. *J Fluids Struct.* 2011;27(8):1461–1470. doi: 10.1016/j.jfluidstructs.2011.08.002
- [18] M.W. Gee, C. Förster, W.A. Wall, A computational strategy for prestressing patient-specific biomechanical problems under finite deformation, *Int. J. Numer. Methods Biomed. Eng.* 26 (1) (2010) 52–72.
- [19] H. Weisbecker, D.M. Pierce, G.A. Holzapfel, A generalized prestressing algorithm for finite element simulations of preloaded geometries with application to the aorta, *Int. J. Numer. Methods Biomed. Eng.* 30 (9) (2014) 857–872.
- [20] P. Landkammer, M. Caspari, P. Steinmann, Improvements on a non-invasive, parameter-free approach to inverse form finding, *Comput. Mech.* 61 (4) (2017) 433–447.
- [21] Feng X., Samani A.. Reconstruction of the Stress-free Hyperelastic Parameters of Breast Tissue: Machine-Learning Based Inverse Problem Technique in *CMBES Proc.*;45 2023.
- [22] Dempsey S.C.H., O’Hagan J.J., Samani A.. Measurement of the hyperelastic properties of 72 normal homogeneous and heterogeneous ex vivo breast tissue samples *J Mech Behav Biomed Mater.* 2021;124:104794.
- [23] Ogden, R. W. (1997). *Non-linear elastic deformations.* Dover Publications.
- [24] Holzapfel, G. A. (2000). *Nonlinear solid mechanics: A continuum approach for engineering.* Wiley.

[25] Gurtin, M. E. (2008). *An introduction to continuum mechanics*. Academic Press.

[26] Pearson, K. (1901). "On Lines and Planes of Closest Fit to Systems of Points in Space". *Philosophical Magazine*. 2 (11): 559–572.

[27] <https://www.open3d.org/>

[28] Zhang, M., Zheng, Y. P., & Mak, A. F. T. (1997). Estimating the effective Young's modulus of soft tissues from indentation tests—nonlinear finite element analysis of effects of friction and large deformation. *Medical Engineering & Physics*, 19(6), 512–517.  
[https://doi.org/10.1016/S1350-4533\(97\)00017-9](https://doi.org/10.1016/S1350-4533(97)00017-9)

[29] Cao, Y., Ma, D., & Raabe, D. (2009). The use of flat punch indentation to determine the viscoelastic properties in the time and frequency domains of a soft layer bonded to a rigid substrate. *Acta Biomaterialia*, 5(1), 240–248.  
<https://doi.org/10.1016/j.actbio.2008.07.020>

## Chapter 5

### 5 « Biomechanics-driven Optimization of Bra Shape Design for Women with Bilateral Asymmetry: Leveraging Individual MRI Data and Hyperelastic Parameters for Breast-Bra Contact Mechanics– Preliminary Study »

#### 5.1 «Introduction »

A significant portion of the female population experiences breast bilateral asymmetry, with estimates suggesting as high as 87% of women are affected [1]. This asymmetry goes beyond aesthetic differences. Research indicates a concerning correlation between breast asymmetry and an increased risk of breast cancer development [2-3]. This was confirmed through the study presented in Chapter 2. Within asymmetric breast tissue, areas of concentrated stress within breast tissue have been linked to tumor formation and the potential transformation of healthy tissue into cancerous growths [4]. Unfortunately, traditional off-the-shelf bras typically adopt symmetrical designs which may lead to discomfort and tissue stress concentration in the larger and/or stiffer breast. To avoid this discomfort, affected women may choose to select the bra based on their larger breast's size. However, this may lead to inadequate support for the smaller breast. Improper design parameters in bra shape can lead to serious consequences, such as stress concentration or insufficient support which may lead to breast movement and friction on the nipples. Other than increasing the risk of breast cancer, overly tight bra pressure may generate excessive pressure on the shoulders, chest, and underbust area, affecting normal breathing and blood circulation and potentially creating localized stress concentration and hindering efforts to promote healthy breast tissue distribution.

A well-designed bra must fulfill two key functions: provide comfortable support by closely matching breast contours and avoid applying excessive contact pressure [5]. Finite Element (FE) modeling has emerged as a powerful tool within bra design, allowing for detailed analysis of bra-breast interaction. Bra design FE modeling involves the use of complex anatomical structures and biomechanical models to simulate breast deformation

and pressure and stress distribution. Analyzing the mechanical interaction between the breasts and bra provides valuable insights for selecting the optimal bra shape and fabric. The modeling process considers several factors such as material nonlinearity, geometric nonlinearity, and the interaction between the bra and the breast. Some studies have successfully developed FE models to analyze bra shape effects and pressure exerted by different bra material [6-8]. These models construct three-dimensional FE models based on 3D-scan data while they consider hyperelastic material models such as Mooney-Rivlin model for breast deformation. One common limitation of these models pertains to using inaccurate tissue mechanical properties. Current hyperelastic parameters, assigned to breast tissue in these models, fail to account for individual variations and preloading bias. Individual factors such as age, ethnicity, and breast size can all influence the tissue's biomechanical properties [9]. This lack of personalization potentially limits a model's accuracy and predictive capability. Moreover, ignoring the influence of gravity force on the measured hyperelastic properties and the stress-free reference geometry of the breast inevitably impacts the model accuracy as discussed in Chapters 3 and 4.

Although FE models are becoming increasingly prevalent in product design, limited published literature explores their application in bra design analysis. Firstly, the focus has largely been on simulating and understanding the effects of the conventional design approach where the bra cup is typically segmented into two main parts: the lower half forms a complete hemisphere to provide a foundational support, and the upper half comprises two triangular sections derived from slicing the top of a sphere, designed to encase and mold the upper portion of the breast. Due to the complexity of modeling breast-bra contact mechanics and internal breast tissue variations, most studies concentrate on sports bras that compress the breast significantly rather than everyday bras [10-12]. Li et al. [13] proposed a biomechanical model of women's bodies and bra, studying the impact of uniform walking on breast dynamic deformation. However, the researchers did not develop their models based on actual human images and did not consider gravity and the initial pressure of the underwear. The FE model of the breast and bra established by Brunon et al.[14], which does not consider gravity, demonstrates that due to the complex compound structure of women, the high degree of material nonlinearity, and the large deformations involved in motion, it is challenging to address the

contact dynamics between women's breasts and their bra using FE analysis. Given the above challenges, research on the biomechanical analysis of everyday bras is scarce. Furthermore, existing FE models rarely address the issue of breast asymmetry while overlooking this asymmetry in such models fail to capture potentially harmful stress concentration. This leaves unanswered questions about whether everyday bra design could be actively tailored to promote a more uniform and healthier stress distribution for women with breast bilateral asymmetry.

To address these issues, we proposed an everyday bra design method that considers comfort while reducing the risk of breast cancer development. It is focused on effectively solving the stress concentration problem for women with breast bilateral asymmetry. Specifically, essence of the proposed design approach is reflected in the following four aspects:

1. We introduce the unloaded state of the breast obtained using the methods described in Chapter 4 into the FE modeling. This leads to accurate estimation of the breast tissue stress distribution while the bra is worn, thus providing a more reliable basis for optimizing the bra design, including its shape and fabric.
2. We use the accurate tool developed for stress distribution estimation in conjunction with machine learning algorithms to optimize bra design where the major optimization criteria is stress concentration minimization. This makes possible designing personalized bras according to the shape, size, bilateral asymmetry and tissue hyperelastic parameters of the woman if available.
3. We propose an alternative method for the breast-bra contact mechanics analysis, which effectively addresses common convergence and low speed challenges of traditional contact mechanics models. In addition to guaranteeing solution convergence, using the proposed contact mechanics technique leads to acceleration of the optimization process which is the primary part of the proposed bra design technique.

4. We develop a bra shape design framework that takes breast contour as the starting point and tailors the shape to the individual. This is in contrast to other design methods that make limited modifications to existing bra shapes based on FE modeling.

It is anticipated that the proposed design technique leads to more comfortable, safe and effective bra design options.

## 5.2 « Material and Methods »

This proposed bra design method is founded on an optimization algorithm which starts with an initial guess for the bra (parameterized) geometry and its fabric mechanical properties. Next the novel breast-bra contact mechanics technique briefly described in Figure 5-1 is conducted. This technique outputs the breast tissue stress distribution which is checked for its level of spatial uniformity. If this stress uniformity is not maximized, the bra shape parameters and its fabric properties are changed within the optimization process before the stress analysis process is carried out again. This process is repeated until the stress uniformity is maximum. The contact mechanics technique developed for the bra optimization method employs a two-step framework to compute the tissue breast distribution. First, it aligns the breast and bra surfaces before the bra is moved towards the breast to initiate contact. Essentially, this simulates how the bra is practically worn. This step utilizes the unloaded breast geometry obtained from the technique described in Chapter 4 as a starting int. Gravity force is applied while the woman is standing in upright position before the contact is initiated. The second major block of the contact mechanics algorithm formulates the contact loading in the FE model as a prescribed boundary condition. This formulation drastically reduces the problems level of nonlinearity involved in typical contact mechanics problems, hence address convergence issues commonly encountered in contact mechanics problems.

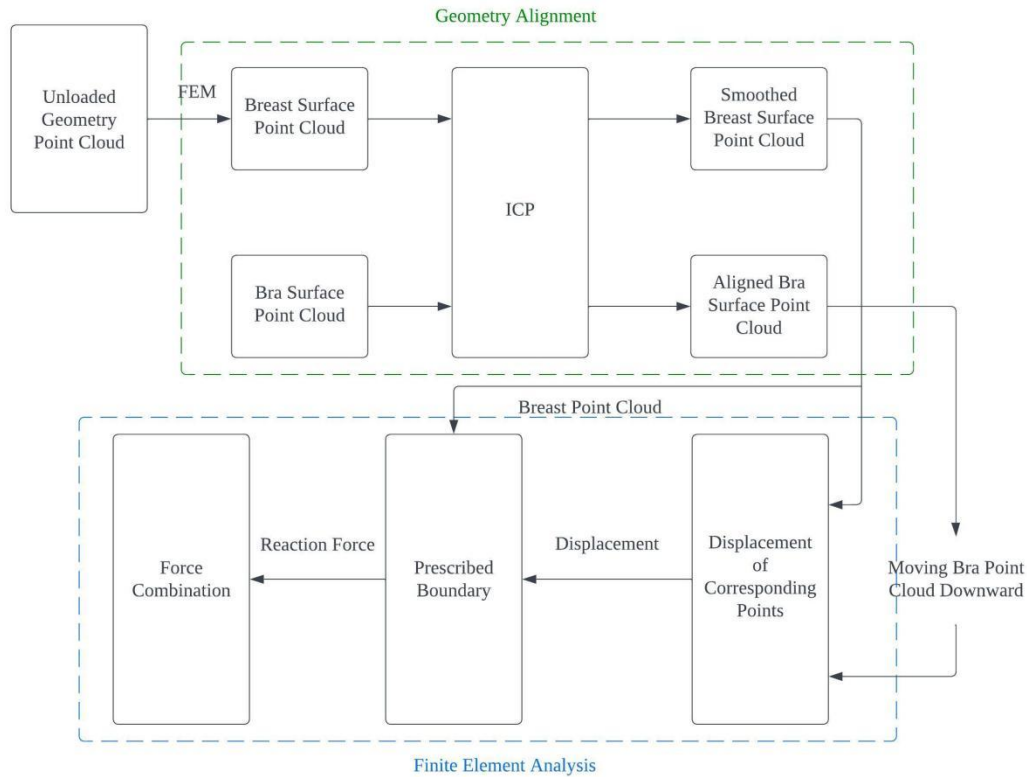


**Figure 5-1: Flowchart of proposed breast-bra contact mechanics technique.**

### 5.2.1 Geometry Alignment

#### **Breast Sub-model:**

Unlike other bra design approaches, our study focuses on personalized bras for those with significant breast bilateral asymmetry. To achieve this goal, we started with the unloaded geometry obtained from a previous project, which was reconstructed from MRI data. Since the MRI-reconstructed geometry was acquired for prone body position, we first rotated the breast geometry model 90 degrees to change it from a prone position to a standing upright position. To simulate this rotation, we imported the rotated surface point cloud into Abaqus FE solver (SIMULIA, Providence, RI, USA) and created a 3D solid meshed part. After assigning the unloaded hyperelastic parameters to the part, a gravity

loading in the  $-Z$  direction was applied to it where the  $Z$ -axis points downward when the woman stands upright. This step aims to simulate the natural shape of the breast when a woman stands upright. We extracted the surface point cloud of this deformed breast shape and used it for subsequent breast-bra contact model.

### **Bra Parameterization Model:**

For the bra shape optimization, it is necessary to mathematically represent the shape using a reasonably small number of parameters. In the unloaded breast geometry reconstruction study, which was presented on Chapter 4, we explored the unloaded shape space and enriched the data through non-isotropic scaling. Observations from this process showed that the deformation of the breast after loading exhibits a difference between the upper and lower hemispheres (divided by the nipple), which is mainly influenced by Cooper's ligaments [15]. Based on these observations, our design adopted bra shape characterization based on the two different hemispheres where each is mathematically presented by a paraboloid with distinct curvatures. This approach leverages the geometric properties of paraboloids to achieve a tailored fit, by precisely merging two sections with varying degrees of curvature to accommodate the natural shape and size variations of the breast. It is crucial to emphasize that this approach merely sets the stage for the initial shapes, which are then refined and optimized through an iterative process to achieve the best possible fit and support. As such, the bra shell can be mathematically modeled using two parabolic equations, each representing half of the shell. The general form of a parabolic equation in three dimensions can be expressed as:

$$z = \mathbf{c}(R^2 - x^2 - y^2) + H \quad (5-1)$$

where  $z$  is the height of the paraboloid at any point  $(x,y)$ ;  $R$  represents the radius of the breast at its base, which is the maximum cross-sectional radius of the breast on the chest plane;  $H$  denotes the height from the base of the breast to its apex, indicating the vertical distance from the lowest to the highest point of the breast; and  $\mathbf{c}$  is the curvature of the paraboloid. The curvature of the bra's upper half ( $\mathbf{c}_{upper}$ ) was derived from the unloaded

breast shape, representing the natural, unsupported form of the breast. This curvature aims to mimic the breast's shape without the influence of gravity, providing a baseline for the upper section of the bra shell. Lower half curvature ( $c_{lower}$ ) was based on the breast shape when deformed by gravity, indicating how the breast sags or changes shape under its weight. This curvature was crucial for designing the lower section of the bra shell to offer support and maintain the desired breast shape against gravitational pull. The transition between the upper and lower halves required ensuring continuity and smoothness at the boundary.  $Z_{transition}$  represents the height at which the transition occurs, we ensured  $Z_{upper}(Z_{transition})=Z_{lower}(Z_{transition})$  and their derivatives were also equal at this point to maintain a smooth surface. The initial shape design of the bra provides an excellent foundation for subsequent Finite Element Method (FEM) experiments. By incorporating specific curvatures derived from both the natural state of the breast and its shape under the influence of gravity, the model facilitates a nuanced analysis of the bra's performance in terms of support, fit, and comfort.

### **Alignment of bra and breast surfaces:**

Before initiating the contact between the two surfaces of the bra and breast, the two surfaces must be aligned. In the proposed technique, this alignment is achieved using the Iterative Closest Point (ICP) method [16] which is employed to achieve geometric alignment of surface point clouds representing the shapes of the breast and bra. Essentially, this step simulates the process of a person trying on a bra and adjusting it from an initial misaligned state to a near-perfect fit.

The Iterative Closest Point (ICP) algorithm is a widely used method for aligning two surfaces, typically 3D models or point clouds, by minimizing the distance between them. After starting with an initial transformation, the ICP algorithm iteratively revises the transformation needed to align a source shape to a target shape. It can be broken down into several key steps: selecting corresponding points, determining the optimal transformation, and applying this transformation to achieve alignment. Mathematically, the ICP process seeks to find the rigid body transformation (rotation  $\mathbf{R}$  and translation  $\mathbf{t}$ )

that minimizes the sum of squared distances between corresponding points across the two datasets. Given a set of source points  $\mathcal{S}=\{s_1, s_2, \dots, s_n\}$  and the corresponding set of target points  $\mathcal{T}=\{t_1, t_2, \dots, t_n\}$ , the ICP algorithm minimizes the following objective function:

$$E(R, t) = \sum_{i=1}^n \|(R s_i + t) - t_i\|^2 \quad (5-2)$$

$E$  is the error metric, a sum of squared distances,  $R$  is the rotation matrix,  $t$  is the translation vector,  $s_i$  are the points of the source shape,  $t_i$  are the corresponding points on the target shape.

We applied ICP experiment with the initial separate point clouds gathered for both the breast, which serves as the target shape, and the bra, designated as the source shape. The bra's initial point cloud was approximately scaled to the size of the breast, which reflects a realistic scenario of an individual selecting a bra with an almost suitable fit. Following this, the ICP iterations commence, each embodying a sequence of steps to achieve precision in alignment. The process initiated with a closest point search, where for each point on the bra, a corresponding nearest point on the breast surface was identified, laying the groundwork for point matching. Subsequently, transformation estimation was conducted to compute the optimal rigid transformation, which involved calculating rotation and scaling factors that minimize the distances between these newly established point pairs.

With the transformation parameters at hand, we proceed to adjust the bra shape by applying the calculated rotation and scaling, thus moving it into a closer alignment with the breast shape. In parallel, the breast shape underwent a surface smoothing process, utilizing a  $k$ -nearest neighbors algorithm ( $k$ -NN) [17]. The advantage of employing  $k$ -NN in this context is its ability to smooth while conservatively preserving the geometrical features of the breast shape. Specifically, the  $k$ -NN was applied to the top 1% of points with the greatest distance discrepancy post-transformation, restricted to a neighborhood of no more than 20 points. This constraint was critical as it ensured that the breast shape does not lose its intrinsic curvatures due to excessive smoothing. The  $k$ -NN algorithm is mathematically represented by:

$$S(p_i) = 1/k \sum_{j=1}^k w_j \cdot p_{n_j} \quad (5-3)$$

where  $S(p_i)$  is the smoothed position of point  $p_i$ ,  $k$  is the number of nearest neighbors,  $w_j$  are the weighting factors (based on distance), and  $p_{n_j}$  are the positions of the nearest neighbor points. This iterative process of alignment and smoothing edges the bra shape incrementally closer to the breast, iterating towards an objective where at least 70% of the points are in complete alignment, reducing friction between the breasts and the fabric. This alignment well simulated the act of a bra conforming to the contours of the body when worn.

### 5.2.2 Finite Element Analysis

In the finite element analysis (FEA) phase of the simulation, we simulated the final adjustments typical of wearing a bra, which includes fastening the back strap and adjusting the shoulder straps. Normally, such adjustments would redistribute breast tissue to achieve a snug fit. As simulating this detailed process within FEA is complex to the high nonlinearity of the associated breast-bra contact mechanics problem, we modeled the state of bra post-adjustment for simplicity. This modeling approach is founded on the assumption that the bra deformation insignificant compared to the breast deformation. The fastening and adjustment of the bra typically introduces two principal forces: F1 and F2 shown on Figure 5-2. F1 is directed normal towards the torso, emulating the force exerted by the lower edge of the back strap. F2, inclined at a 5° - angle along the z-axis, simulates the force exerted by the shoulder straps. To circumvent the challenges of convergence in contact analysis within FEA, we adopted a method involving prescribed boundary conditions as described below.

1. The bra surface was further displaced towards the chest by an initial trial value of 3mm. This displacement value is refined through subsequent iterations. This surface motion generates local compression (contact) at each point of the breast's surface which is consistent with the location of the point on the breast surface contour.

2. Displacements of the breast surface in contact with the moving bra are calculated before they are assigned as prescribed boundary conditions to the corresponding points on the breast point cloud. Prescribed boundary conditions in finite element analysis (FEA) are specific loading constraints applied to the model to simulate real-world physical restrictions and forces. These conditions dictate how certain parts of the model can move or react under simulated physical forces, ensuring the simulation accurately reflects the expected behavior of the system under study. The reason for employing prescribed boundary conditions in this scenario is twofold. Firstly, it allows for a reasonably realistic simulation of how the bra applies forces to and interacts with the breast, capturing the nuances of the bra wearing action where the garment exerts contact pressure and displacement upon the body. Secondly, by assigning specific displacements to the bra model based on expected behavior, the simulation can effectively decouple complex interactions into manageable stages. This approach facilitates a more detailed and accurate analysis of the impact of wearing a bra on breast tissue, where the bra continually applies forces to the breast.

3. The FEA simulation yielded the reaction force at each point on the breast surface subjected to the prescribed displacement boundary condition. We then aggregated the reaction forces across all points on the breast based on static equilibrium to calculate the counteracting forces, resulting in the determination of forces F1 and F2. Figure 5-2 sketches the Poisson's of two forces apply.

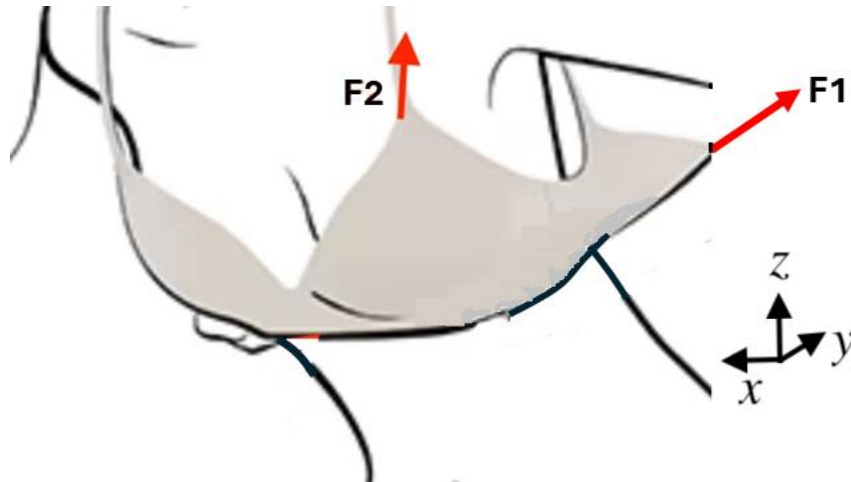


**Figure 5-2: A sketch of two forces F1 and F2 which bra applies.**

Following the generation of forces F1 and F2, we conducted an evaluation to determine if the magnitude of these forces fall within a reasonable range. This assessment aimed at ascertaining whether the initial 3mm displacement was excessive. Through an iterative process, we optimize the displacement distance, ultimately identifying the most appropriate values for F1, F2, and the bra displacement towards the chest that most closely align with realistic garment fit. The optimization process ensured that the positioning of the bra and breast was conducive to comfort. This was achieved by adjusting the forces F1 and F2 to ideal levels [18], thereby ensuring that neither the lower edge of the bra nor the shoulder straps exert undue pressure on the wearer. Subsequently, we analyzed the stress distribution on the breast volume using Abaqus to ensure that it was reasonably uniform and within acceptable limits. This step was for ensuring minimal risk of future development of breast cancer and comfort of the bra's fit.

## 5.3 « Preliminary Results »

### 5.3.1 Geometry Alignment and Displacement Mapping

Figure 5-3 presents the breast surface point cloud after aligning the geometry, where each point is assigned a displacement vector. This vector represents the adjustment needed to move each corresponding point on the bra closer to the chest, aiming for a more accurate fit. The displacement vectors are illustrated as gray arrows, each pointing in the direction where the point should move to align with the chest surface more closely. Due to the three-dimensional nature of these displacement vectors, which consider the complex topography of the breast surface, the arrows may appear somewhat scattered when viewed collectively, as visualized using the Open3D toolkit.

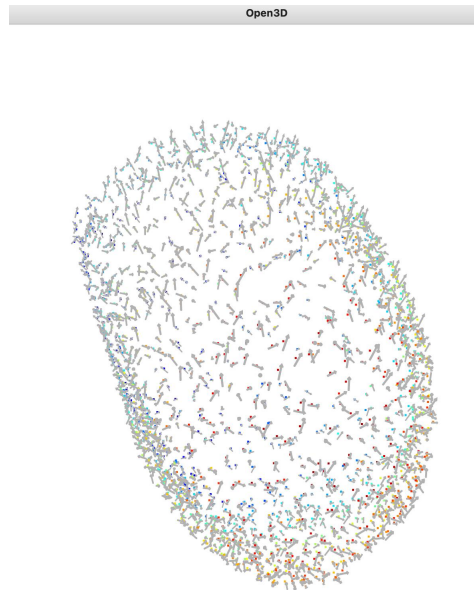


**Figure 5-3: Displacement mapping of breast surface points assigned with the displacements of corresponding bra surface points.**

### 5.3.2 Resultant Forces from Repeated Experiments

We repeated experiments and continuously adjusted the specific motion of the bra towards the chest, along with assessing the F1 and F2 forces with their components reported in Table 5-1. This table indicates that when the bra is moved towards the chest by 3mm, the resultant forces  $F_y$  are relatively large. As the bra movement decreases to 2.3mm, the two resultant forces reach more balanced levels. Further loosening of the bra's displacement towards the chest leads one of the resultant forces to become negative, indicating that the bra at this position is no longer providing adequate support to the breast.

In repeated experiments of bra displacement and its impact on breast support, the occurrence of negative forces is a critical aspect to consider. Forces F1 and F2 are the resultant forces derived from computing the reaction forces at each point on the breast surface. These forces are decomposed into components along specific axes. In this context, a negative value indicates that the force component in the negative direction of the axis is greater than that in the positive direction. This results from the vector sum of all the three-dimensional forces acting across the surface points of the breast. For instance, when the bra is adjusted to a position where it is moved 2.0 mm towards the chest, F2 exhibits greater force in the negative y-direction, which corresponds to a movement away from the body (the positive y-direction signifies a movement towards the trunk of the body). Similarly, a negative force in the z-direction, where the negative indicates a loosening effect (the positive z-direction represents an upward pulling force by the shoulder straps), suggests that the straps do not provide adequate tension to support and lift the breast effectively. The magnitude of F2 is a relatively small negative force, which implies that under a bra motion of 2.0 mm, the corresponding strap does not generate appreciable amount of resistance to the motion due to its inability to resist compression. This analysis shows that a displacement of 2.3 mm towards the chest leads to a more balanced level of force, indicating that this is a more optimal relative positioning between the bra and breast for providing effective support. This highlights the importance of precise adjustments in the bra fit to ensure that the forces exerted by the bra are neither excessive nor insufficient. In practical terms, this ensures that the greatest pressure is

applied where it is most needed at the base of the chest, especially for larger breasts where the bra cup must counterbalance the gravitational pull and provide a substantial level of support, thereby generating significant reactionary forces at these critical points. Hence, we determine the optimal relative position of the breast and bra to correspond to 2.3mm motion towards the chest after alignment with the breast. It is evident that when wearing an everyday bra, the greatest pressure is exerted on the base of the chest, followed by the shoulder straps. This is particularly true for larger breasts as the bra cup provides a certain level of support, resulting in a significant reactionary force at the base of the chest.

**Table 5-1: Optimal bra displacement and resultant forces analysis.**

	$F_1$ Backbend (N)			$F_2$ Shoulder Strap (N)		
	$F_x$	$F_y$	$F_z$	$F_x$	$F_y$	$F_z$
-3mm	0	26	0	0.56	20	4.16
-2.8mm	0	20	0	0.32	15	5.12
-2.3mm	0	6.16	0	0.43	0.91	4.96
-2.0mm	0	5	0	0.069	-0.93	-1.44

### 5.3.3 Stress Analysis at Optimal Position

A stress analysis of the breast at this optimal position reveals a more reasonable and uniform stress distribution on the breast surface. Figure 5-4 demonstrates the stress distribution over the breast surface, revealing that most regions experience low and uniform stress levels. A closer inspection from the side reveals minor areas with slightly elevated stress, which we attribute to the reactive forces from the torso. We plan to further employ gradient descent optimization to refine the bra design with the aim of minimizing stress nonuniformity within the breast volume.

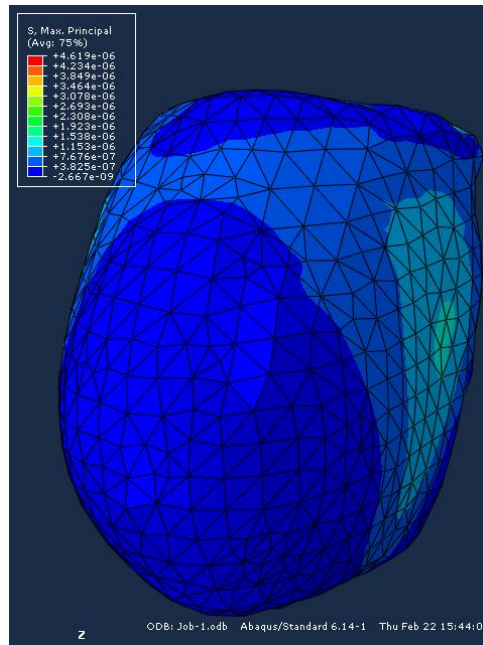


**Figure 5-4: Stress Distribution Analysis on Breast Surface.**

## 5.4 « Discussion and Conclusions »

This study was performed in pursuit of the long-term objective of the research presented in this thesis, which is addressing elevated breast cancer risk among women with breast bilateral asymmetry. One concept we pursued to mitigate this risk is founded on the evidence of correlation between this bilateral asymmetry and breast cancer development [19]. Evidence also exists that indicate that the underlying cause of this risk elevation pertains to the biomechanical environment breast cells experience while women wear their everyday bra [20]. The evidence points to stress concentration arising from contact between the bra and breast surface. According to the principles of solid mechanics, the stress distribution is dependent on the configuration of the breast and the bra's fabric and straps. The distribution also depends on the breast tissue distribution, its heterogeneity and mechanical properties. The preliminary research presented in this chapter tackles the shape and mechanical properties of the bra's fabric and its straps by developing an

everyday bra design method with the primary aim of minimizing the risk of future breast cancer development. Ensuring exertion of minimum pressure of bra on the breast surface while minimizing breast tissue stress concentration towards comfort and future breast cancer risk minimization, this study proposes a methodology that guides the shape design of everyday bra. In this preliminary study, we developed a biomechanics-driven methodological approach based on fine-tuning of the bra's fit by adjusting the initial bra displacement towards the chest to ensure comfort and structural compatibility of the garment with the woman's anatomy. Through iterative adjustments and detailed biomechanical analysis, we were able to achieve an optimized fit that balances comfort with support, highlighting the effectiveness of integrating ICP alignment and FEA in garment fitting simulations.

Due to individual environmental differences, material selection limitations, and human interference, most other relevant research [13-14,21-22] which utilized try-on testing methods are time-consuming and prone to biased results. This study employs a finite element numerical simulation method to provide a quantifiable assessment of clothing pressure and to evaluate the performance of different design parameters. Further research is necessary to complete the optimization algorithm necessary to determine optimal parameters of bra shape and bra fabric and its straps mechanical properties.

## Reference

- [1] Scutt, D., Lancaster, G. A., & Manning, J. T. (2006). Breast asymmetry and predisposition to breast cancer. *Breast cancer research*, 8(2), 1-7.
- [2] Alterson, R., & Plewes, D. B. (2003). Bilateral symmetry analysis of breast MRI. *Physics in Medicine & Biology*, 48(20), 3431.
- [3] Scutt, D., Manning, J. T., Whitehouse, G. H., Leinster, S. J., & Massey, C. P. (1997). The relationship between breast asymmetry, breast size and the occurrence of breast cancer. *The British Journal of Radiology*, 70(838), 1017-1021.

- [4] Andersen, B. L., Farrar, W. B., Golden-Kreutz, D., Kutz, L. A., MacCallum, R., Courtney, M. E., & Glaser, R. (1998). Stress and immune responses after surgical treatment for regional breast cancer. *JNCI: Journal of the National Cancer Institute*, 90(1), 30-36.
- [5] Hardaker, C., & Fozzard, G. J. (1997). *International Journal of Clothing Science and Technology*, 9, 311.
- [6] Cai, Y., Yu, W., & Chen, L. (2016). Finite element modeling of bra fitting. In W. Yu (Ed.), *Advances in Women's Intimate Apparel Technology* (pp. 147-168). Woodhead Publishing. <https://doi.org/10.1016/B978-1-78242-369-0.00009-8>
- [7] Zhang, S., Yick, K. L., Chen, L., Yu, W., Lau, N., & Sun, Y. (2020). Finite-element modelling of elastic woven tapes for bra design applications. *The Journal of The Textile Institute*, 111(10), 1470-1480.
- [8] Liang, R., Yip, J., Yu, W., Chen, L., & Lau, N. M. L. (2019). Numerical simulation of nonlinear material behaviour: Application to sports bra design. *Materials & Design*, 183, Article 108177. <https://doi.org/10.1016/j.matdes.2019.108177>
- [9] Boyd, N. F., Martin, L. J., Bronskill, M., Yaffe, M. J., Duric, N., & Minkin, S. (2010). Breast tissue composition and susceptibility to breast cancer. *Journal of the National Cancer Institute*, 102(16), 1224-1237.
- [10] Zhang, J., Lau, N. M., Sun, Y., Yip, J., Yick, K. L., Yu, W., & Chen, J. (2022). Non-linear finite element model established on pectoralis major muscle to investigate large breast motions of senior women for bra design. *Textile Research Journal*, 92(19-20), 3511-3521.
- [11] Zhu, C. L., Long, W., Ying, B. A., & Qi, J. (2020). Finite element simulation of the dynamic pressure distribution of a typical compression sports bra during wearing. *Journal of Fiber Bioengineering and Informatics*, 13(4), 211-219.

- [12] Li, Y., Zhang, X., & KW, Y. (2003). A 3D biomechanical model for numerical simulation of dynamic mechanical interactions of bra and breast during wear. *Sen'i Gakkaishi*, 59(1), 12-21.
- [13] Li, Y., Zhang, X., & KW, Y. (2003). A 3D biomechanical model for numerical simulation of dynamic mechanical interactions of bra and breast during wear. *Sen'i Gakkaishi*, 59(1), 12-21.
- [14] Bel-Brunon, A., Bouten, L., Cornolo, J., & Morestin, F. (2014, July). Numerical modeling of bra wear during running. In 11th World Congress on Computational Mechanics.
- [15] Holzapfel, G. A., & Ogden, R. W. (2009). *Mechanics of biological materials*. New York: Springer Science & Business Media.
- [16] Besl, P. J., & McKay, N. D. (1992, April). Method for registration of 3-D shapes. In *Sensor fusion IV: control paradigms and data structures* (Vol. 1611, pp. 586-606). Spie.
- [17] Fix, E., & Hodges, J. L., Jr. (1951). *Discriminatory Analysis. Nonparametric Discrimination: Consistency Properties*. USAF School of Aviation Medicine, Randolph Field, Texas.
- [18] Song, X., & Feng, X. (2006). Relationship between garment pressure and human body comfortableness. *Journal of Textile Research*, 27(3), 103.
- [19] Scutt, D., Manning, J. T., Whitehouse, G. H., Leinster, S. J., & Massey, C. P. (1997). The relationship between breast asymmetry, breast size and the occurrence of breast cancer. *The British journal of radiology*, 70(838), 1017-1021.
- [20] Butcher, D. T., Alliston, T., & Weaver, V. M. (2019). A tense situation: Mechanical forces in cancer development. *Nature Reviews Cancer*, 19(2), 88-102.  
<https://doi.org/10.1038/s41568-018-0087-4>.

[21] Sun, Y., Yick, K. L., Yu, W., Chen, L., Lau, N., Jiao, W., & Zhang, S. (2019). 3D bra and human interactive modeling using finite element method for bra design. *Computer-Aided Design*, 114, 13-27.

[22] Sun, Y., Yick, K. L., Cai, Y., Yu, W., Chen, L., Lau, N., & Zhang, S. (2021). Finite element analysis on contact pressure and 3D breast deformation for application in women's bras. *Fibers and Polymers*, 22(10), 2910-2921.

## Chapter 6

### 6 « Conclusions and Future Work »

#### 6.1 « Conclusions »

This study advances the field of personalized bra design for women with bilateral breast asymmetry and those at elevated breast cancer risk, a population significantly underserved by current approaches. With biomechanics-driven modeling at its core, we broke this ambitious goal into key interconnected but independent projects. A novel unsupervised machine learning framework was successfully developed for enhanced breast cancer risk assessment based on longitudinal MRI data. This work surpassed prior label-based supervised methods, providing a data-driven tool for long-term cancer-risk prediction framework. To overcome inaccuracies introduced by gravity induced breast tissue stresses, we developed a computational inversion technique for breast biomechanics modeling. This innovation enabled us to estimate stress-free breast tissue hyperelastic parameters from their loaded counterpart. Subsequently, a correlated framework was established to reconstruct stress-free breast geometries from MRI, leveraging our stress-free hyperelastic parameter work alongside Finite Element modeling and Neural Network mapping. Lastly, utilizing these earlier results, an intricate customization framework for bra design was devised. Our approach uses breast stress uniformity as an objective function through patient-specific unloaded parameter and geometry, offering customized fit and support. This dissertation comprises four chapters detailing these research investigations. Each chapter's central contributions and resulting insights are outlined below.

##### 6.1.1 Chapter 2

This chapter delves into the pressing necessity for developing advanced, unsupervised classifier for breast cancer risk prediction using a longitudinal MRI dataset, with a particular emphasis on the analysis of asymmetry features. In addressing this critical need, our machine learning pipeline has adeptly navigated the complexities of this challenge.

By analyzing MRI data both volume-by-volume and slice-by-slice, our approach facilitated an exhaustive exploration of MRI feature spaces and improved precision in asymmetry analysis. The results demonstrated significant advancements in clustering accuracy and effectiveness, as evidenced by rigorous cross-validation processes utilizing sequentially labeled data (categorized as positive or negative). This validation not only underscores the robustness of our machine learning model but also highlights its superior capability in identifying nuanced patterns of asymmetry that are crucial for detecting the tendency of a tumor to be cancerous. As a potential early warning system, our machine learning technique outlined in this chapter not only addresses an urgent need in breast cancer risk assessment but also paves the way for advances in the field of preventative care.

### 6.1.2 Chapter 3

In this chapter, a novel computational inversion technique for determining patient-specific stress-free breast tissue hyperelastic parameters was developed. The novelty of this technique primarily stems from its ability to address parameter preloading-induced inaccuracies often present in traditional biomechanical modeling. Through a rigorous experimental protocol, a comprehensive dataset of unloaded hyperelastic parameter values was generated. These parameters were then translated into their loaded counterpart using accurate simulation technique. The accuracy of this parameter mapping was rigorously assessed based on subsequent geometry reconstruction results, which is shown in Chapter 4. Specifically, this computationally driven approach avoids the need for direct, patient-specific measurement of stress-free hyperelastic parameters, which is impractical. In conclusion, this study demonstrated a very good feasibility for predicting stress-free breast hyperelastic parameters from more readily obtainable loaded counterparts. The proposed technique is anticipated to be adapted into the modeling processes of other soft tissues to enhance the precision of relevant biomedical applications.

### 6.1.3 Chapter 4

In this chapter, we developed an innovative methodology for reconstructing an individual's stress-free breast geometry, addressing a key limitation in biomechanical modeling. The core novelty of this work lies in overcoming the inaccuracies introduced when using MRI-derived geometries that inherently reflect gravity-loaded breast shapes. Combining Finite Element modeling with unloaded hyperelastic parameters (obtained through the technique presented in Chapter 3), we generated a detailed 'shape space' representing a realistic range of stress-free breast configurations. A neural network was subsequently trained to establish a robust mapping from an individual's loaded breast geometry to its unloaded counterpart within this space. Validation was performed using a 'reverse simulation' approach demonstrating high accuracy. Crucially, our method successfully determines a realistic stress-free geometry without involving any experimental work. In conclusion, the two interwoven projects presented in Chapters 3 and 4 related to the stress-free state of tissue and breast shape provide a foundation for improving the precision in personalized breast modeling.

### 6.1.4 Chapter 5

This chapter presented a preliminary investigation pertaining to the development of a computational framework for bra design, where breast tissue stress uniformity was utilized as a fundamental design principle. To our knowledge, this has not been done before. The iterative framework incorporated initial surface alignment (iterative closest point algorithm), Finite Element breast stress modeling with prescribed boundary conditions, and a tailored optimization strategy maximizing breast tissue stress uniformity. The innovation of this study builds on our prior work by incorporating the stress-free insights gained (through stress-free hyperelastic parameters and geometry estimation). Crucially, this work directly addresses the unique needs of individuals with significant breast bilateral asymmetry, a population currently underserved by the traditional bra industry. The integration of insights from our early-stage breast bilateral asymmetry classification and risk assessment work paves the way for bra designs that not

only enhance support and comfort but could also play a vital role in long-term breast health monitoring within this higher-risk population.

## 6.2 « Future Directions »

While the proposed investigations offer significant advances in personalized bra design for asymmetric breasts and breast cancer risk prediction, further refinement and expansion are necessary to maximize their translational potential. Firstly, expanding our analysis to a larger, more diverse patient cohort and integrating a wider array of breast features (including tissue density and hormonal variations) would solidify the robustness of our model, ensuring inclusivity and broader applicability. Furthermore, developing user-friendly interfaces for both medical professionals and patients would significantly enhance the clinical use and accessibility of these powerful tools.

In Chapter 2, while successful in predicting cancer risk based on bilateral asymmetry, our model would benefit significantly from validation across larger, more diverse datasets, ideally representing various age groups and breast compositions. Refining prediction based on specific patterns within asymmetry (e.g., volume vs. density differences) offers significant potential to further individualized risk assessment. Finally, establishing potential correlations between changes in asymmetry and genetic predisposition markers through carefully designed collaborative studies could revolutionize our understanding of how bilateral asymmetry relates to underlying breast cancer biology.

In Chapters 3&4, we anticipate further validation of our derived unloaded parameters and geometry in a broader scope of biomechanical modeling. This includes assessing their applicability to scenarios involving large deformations and dynamic monitoring. Additionally, we consider the incorporation of dynamic penalty terms to continually refine our Neural Network model.

Chapter 5 aims to deploy this design framework within an industrial context, further enhancing and optimizing the system through sensor-based monitoring and material mechanical testing of bras. The objective is to make this system more compatible with industrial operations and standards, ultimately fulfilling the goal of this research: to provide comfortable and functional bras for women with breast bilateral asymmetry. We also intend to extend the application of this design to support those who have recently undergone breast surgery, whether it be resection or augmentation, as a form of postoperative protection.

### 6.3 « Closing Remarks »

Customized bra design has the potential to be a powerful preventative tool for breast health, especially in individuals with significant breast bilateral asymmetry. Our work establishes a novel computational framework laying the groundwork for such integrated strategies. While this personalized approach is still in its early stages, it carries great promise. Even so, there are key technical challenges that remain to be addressed before its broad clinical translation. Acquiring longitudinal medical imaging data, vital for personalized modeling, poses limitations. In this thesis, this challenge was partially mitigated by leveraging finite element-based data augmentation alongside rigorous validation protocols. However, developing novel, streamlined imaging modalities tailored to breast assessments could facilitate widespread adaptation of our methods. Through a multi-faceted, interdisciplinary approach, further refinement is needed to ensure these techniques achieve optimal levels of robustness and efficiency, ultimately impacting early cancer detection and improving long-term breast health.